Dissertation

Submitted in partial fulfillment of the requirements for the degree of Doctor of Philosophy in Physics in the Graduate School of Science

大阪大学
OSAKA UNIVERSITY

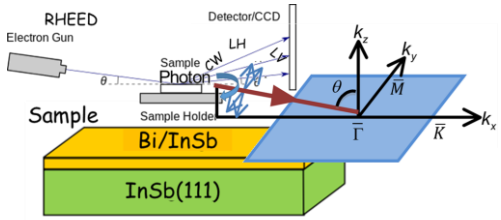

Experimental and theoretical studies on bismuth thin films on semiconductor substrates

Jibon Krishna Modak
Ph.D. Candidate under Bangabandhu Science and Technology Fellowship, Dept. of Physics, RA(FBS), TA(CIS), Osaka University, Japan.

Supervisor

Dr. Shin-ichi Kimura
Professor,
Graduate School of Frontier Biosciences and Department of Physics,
Osaka University, 1-3 Yamadaoka, Suita, Osaka 565-0871, JAPAN.

INDEX

List of Research Contributions & Achievements

Conference Paper

1.	NSICT Conference (2010), Bangladesh, "Electronic Structure calculation of Co2MnSi."
2.	UVSOR symposium (2019), Japan, "Observed the electronic structure of ultrathin Bi(111)/InSb(111)-3x3."
3.	JSR-2020, Japan, "Electronic Structure of ultrathin Bi (111) films of InSb(111)B-3x3."

Poster

1.	NSICT Conference (2010), Bangladesh, "Electronic Structure calculation of Co2MnSi."
2.	UVSOR symposium (2019), Japan, "Observed the electronic structure of ultrathin Bi(111)/InSb(111)-3x3."
3.	JSR-2020, Japan, "Electronic Structure of ultrathin Bi (111) films of InSb(111)B-3x3."

Published Paper

1.	Jamila, N., Jahan, I., **Modak, J. K.**, Hasan, W., Rahman, A., Hossain, M., Choudhury, M., Chowdhury, S., Rahaman, R., & Hasan, Z "DFT-based computational investigations of the Physical Properties of Perovskites-Structure SrXO3 (X = Si, Tb, Th) for Optoelectronic and Thermo-Mechanical Applications" Materials Today Communications, 107650 (2023). https://doi.org/10.1016/j.mtcomm.2023.107650
2.	Barman, P., Rahman, M. F., Islam, M. R., Hasan, M., Chowdhury, M., Hossain, M. K., **Modak, J. K.**, Ezzine, S., & Amami, M, "Lead-free novel perovskite Ba3AsI3: First-principles insights into its electrical, optical, and mechanical properties", *Heliyon*, *9*(11), e21675 (2023). https://doi.org/10.1016/j.heliyon.2023.e21675
3.	M. Z. Hasan, M. A. Rayhan, M. A. Rahman, M. Rasheduzzaman, **J. K. Modak**, and K. M. Hossain, "Insights into the physical properties of inverse Heusler alloy Cr2 CoGa via density functional theory", Phys. Scri., 96, 055704(2021). http://dx.doi.org/10.1088/1402-4896/abe90e
4.	Md. K. Miah, K. M. Hossain, Md. A. Rahman, Md. Rasheduzzaman, S. K. Mitro, **J. K. Modak**, Md. Z. Hasan, "Comprehensive study on the physical properties of tetragonal LaTGe3 (T =Rh, Ir, or Pd) compounds: An ab initio investigation", AIP Advances 11, 025046 (2021). http://dx.doi.org/10.1063/5.0042924
5.	Md. Z. Hasan, K. M. Hossain, S. K. Mitro, Md. Rasheduzzaman, **J. K. Modak** & M. A. Rayhan, "Structural, mechanical, electronic, and anisotropic properties of niobium-doped strontium ferrite: First-principal calculations", Appl.Phys. A**127**, 36(2021). https://link.springer.com/article/10.1007/s00339-020-04219-5
6.	K. M. Hossain, S.K. Mitro, Md. A. Hossain, **J. K. Modak**, Md. Rasheduzzaman, Md. Z. Hasan, "Influence of antimony on the structural, electronic, mechanical, and anisotropic properties of cubic barium stannate", Materials Today 26, 101868(2021). http://dx.doi.org/10.1016/j.mtcomm.2020.101868
7.	Md. Rasheduzzaman, K. M. Hossain, S.K. Mitro, M.A. Hadi, **J. K. Modak**, Md. Z. Hasan, "Structural, mechanical, thermal, and optical properties of inverse-Heusler alloys Cr2CoZ (Z = Al, In): A first-principles investigation", Phys, Letts. A **385**, 126967(2021). http://dx.doi.org/10.1016/j.physleta.2020.126967
8.	K. Rani, S.K Enayat, **J. K Modak**, R. Yasmin, "Adaptive Filtering with Variable Step Size using GLMS Algorithm", Global. J. **13**, 11(2016). https://globaljournals.org/GJCST_Volume15/1-Adaptive-Filtering-with-Variable.pdf

9.	**J. K Modak**, A. I. Nahid, and K. Rani, "Spin Polarization and Electronic Structure calculation of Nickel and Co2MnSi thin film interface", Int. J. Sci. Engi. Res. **6**, 8 (2015). https://www.ijser.org/researchpaper/Spin-Polarization-and-Electronic-Structure-calculation-of-Nickel-and-Co2MnSi-thin-film-interface.pdf
10.	Write a research report about groundwater level for B.Sc. (Engi. project). (Not published)

Achievement

Government Scholarship	2002-2004(For **outstanding performance** in High school and college)
Government Scholarship	2004-2008(For secure **1st position** in undergraduate in Engineering)
National Science and Technology Scholarship	2009-2011(For M.Sc. thesis, **outstanding research performance**)
Lecturer	2011-2014, Bangabandhu Science & Technology University, Bangladesh.
MEXT Scholarship	2012-2015(Ph.D. under Takanashi Lab, Tohoku University, Japan), due to 2 years probationary period the university did not accept study leave, so I **withdrew my name**.
Visiting Teacher	2013-2018, N. Haq College, Gopalganj & North Waster University, Khulna.
Assistant Professor	2015-2022, Bangabandhu Science & Technology University, Bangladesh.
University Grant Project	2016-2017, Making the **digital display** (i.e., Cricket scoreboard)
Associate Editor	2017 to **Present**, Australian Journal of Engineering and Innovation Technology (https://universepg.com/editors/ajeit)
Research Associate	2018-2019 (Osaka University does **not fulfill commitment**)
Bangabandhu Science & Technology Fellowship	2018-2022 (Osaka University, as a Ph.D. Student)
MEXT Scholarship	**I withdrew my name** in 2018-2021 under Masashi Akaburi (JAIST, Japan), due to engaging in a Bangladeshi government project under Osaka University.
Research Assistant	2018 to present, (FBS, Osaka University, Japan)
English Visiting Teacher	2018 to present, IRIS & SEEDS prog., Osaka University, Japan
Associate Professor	2022-2051, Bangabandhu Science & Technology University, Bangladesh.
Experimental Teacher Assistant (eTA)	2023 to present, (CIS, Osaka University, Osaka, Japan)

Acknowledgments

First, I thank my supervisor, Prof. Shin-ichi Kimura, for his kind guidance and experimental support throughout the correction and checking of the writing of this thesis research. The solid training, rigorous attitude, critical thinking spirit, and years of research experience I received from him have benefited me greatly and helped me grow up in academia.

I would like to express my sincere gratitude to my wife, son, and daughter for their unwavering support throughout my research journey. The Bangladeshi government played a crucial role in funding this thesis through the father of the nation, Bangabandhu Sheikh Mujibur Rahman Science & Technology Fellowship Trust. I am also thankful for the financial support provided by Osaka University in the form of a research assistantship (RA), as well as the Japanese government for providing me with a residence during my studies.

The research conducted at IMS, UVSOR, where a portion of the experimental work was carried out, was supported. Additionally, I am grateful to CMC, Osaka University for providing a high-speed system. I would also like to express my appreciation to Konika Rani and her lab for granting me access to their supercomputer facility at the Kadoma lab at Osaka University, Japan.

I also want to give a big thanks to IPC, for giving me the opportunity as well as Prof. Hosaka and Prof. Koshino for their continued mental support in arranging an IPC meeting every semester. I would like to express my gratitude to Prof. Kodama, Director of the Institute of Laser Engineering (ILE) for his care and mental support. Furthermore, I had the privilege of discussing certain aspects of my research with Osaka University President Prof. Nishio and my university Vice-Chancellor Prof. Dr. Mahbub. Both were supportive and provided mental support and considered my study leave extension as an extraordinary leave during the OU and BSMRSTU collaboration purpose.

I would like to express my gratitude to the Osaka University Medical Centre and the Harassment Cell for their unwavering support and understanding during my prolonged period of depression recovery.

Abstract

This study explores the influence of lattice matching on the behavior and electronic structure of bismuth (Bi) thin films on semiconductor substrates such as indium antimonide (InSb). My research combines experimental and theoretical calculations to investigate the impact of the electronic structure of the Bi/InSb system, and results demonstrate that Bi ultrathin films exhibit significant deviations from their expected behavior when not in contact with substrates due to interactions with the substrate itself. Angle-resolved photoemission spectroscopy (ARPES) measurements reveal noteworthy modifications in the film's electronic band structure compared to isolated Bi films, resulting in the formation of a quantum well state (QWS). By analyzing the QWS using the theoretical phase accumulation model (PAM) and comparing it with corresponding fitted parameters from density functional theory (DFT) calculations, my experimental observations are further supported, providing deeper insights into the structural and electronic changes induced by lattice matching. This study offers solutions to longstanding debates in the field by emphasizing the critical role of lattice matching in the epitaxial growth of materials. Furthermore, my experimental evidence reveals a semi-metal-to-metal (SMM) transition during monolayer formation, as well as the presence of QWS starting from the bilayer stage, challenging the prevailing notion of a semi-metal-to-semiconductor (SMSC) transition with decreasing film thickness. These findings provide a fresh perspective on the thickness-dependent properties of Bi thin films.

Motivations

The primary motivation behind this work is to make a valuable contribution to the ever-expanding knowledge of topological materials in nanotechnology. Additionally, I aim to establish a foundation for future investigations into the control and manipulation of electronic states within two-dimensional systems. The discovery of a metallic point-like Fermi surface in Bi (111) on InSb (111) B presents exciting opportunities for the development of innovative electronic devices that harness the unique properties of these materials.

This study aimed to address several debated issues in the field of topological materials bismuth. Firstly, I investigated the impact of lattice matching on the growth of free-standing monocrystals. Contrary to expectations, my experimental results demonstrated that this phenomenon did not occur in practical applications. Secondly, while Bi (111) is typically categorized as a two-dimensional topological insulator (2DTI), my findings showed the absence of potential edge states. However, I did observe the formation of quantum well states (QWS) starting at a thickness of one bilayer (1BL), for considering the crucial tools to calculate bismuth thickness, and based on this calculation observed points like fermi surface down to 1BL. This discovery is a significant achievement in my research, as the metallic characteristics of these states persist down to a thickness of 1BL.

Chapter 1

Chapter 1

1.1 Introduction

In recent years, there has been a significant surge of interest in the study of 2D topological materials, primarily due to their remarkable electronic and topological properties. One particular focus of researchers is the electronic band structure of semimetal Bi, which exhibits a captivating spin-orbit interaction (SOI). This interaction results in a substantial Rashba splitting and serves as a foundation for the development of various topological materials **[1, 2, 3]**. Among these properties, the theoretical prediction of a two-dimensional (2D) topological insulator (TI) in a single free-standing Bi (111) bilayer (BL) has garnered considerable attention **[4, 5]**.

Ultrathin bismuth (Bi) films have also captured the attention of researchers due to their unique surface state, which is protected by time-reversal symmetry. This feature makes them an intriguing candidate for exploring new phenomena **[5]**. Several growth methods and substrates have been utilized to grow Bi films **[6-12]**, with molecular beam epitaxy (MBE) being a particularly popular approach. MBE provides precise control over film thickness and growth rate **[6]**.

In this study, I conducted an experiment where ultrathin Bi films were grown on InSb(111)B substrates using MBE. The characterization of their electronic properties was done through angle-resolved photoemission spectroscopy (ARPES). My experiment revealed the formation of Quantum well states (QWS) starting down to 2BL. I also observed that the quantum well state exhibited a dependence on the film thickness, which I was able to explain using a theoretical model. Moreover, I observed an electron pocket close to the $\bar{\mathbf{M}}$ point and other interesting phenomena on the Bi (111) surface. As a result, I aimed to address some longstanding issues regarding Bi (111), such as its peculiar physical properties. In thicker cases, it behaves as a semimetal, while in thinner cases, it theoretically transitions to a semiconductor. This transition, commonly referred to as the semi-metal to semiconductor transition, has been a subject of debate. My experimental approach aimed to shed light on this question and investigate whether the higher bilayer semi-metal character is trivial or non-trivial. Recent contradictory results have emerged in this regard. However, my findings of electron pockets at higher bilayer thickness and the presence of surface states at the same energy position suggest

that new phenomena remain in higher bilayer thickness, but in the ultrathin case no distinguished features were observed, and little energy shift was observed comparing with pristine InSb band dispersion suggested metallic-like behavior. These findings highlight the unique behavior of ultrathin Bi films and provide a solid foundation for exploring potential applications in quantum computing and spintronics.

1.2 Thesis Overview

The dissertation is organized in the following manner: **Chapter 2** introduces the background and the relevant subject matter. **Chapter 3** provides essential information about the experimental tools used, including reflection-high energy electron diffraction (**RHEED**), core-level photoemission spectroscopy (**CLPES**), and angle-resolve photoemission spectroscopy (**ARPES**). **Chapter 4** delves into the theoretical framework, elucidating the experimental phenomena and demonstrating how theoretical findings effectively elucidate 2D growth and interactions. **Chapter 5** shows the result and engages in a discussion about thin-film growth and characterization. Lastly, **Chapter 6** offers a summary of my work in this thesis and highlights potential avenues for future research.

1.3 Reference

1. C. R. Ast, J. Henk, A. Ernst, L. Moreschini, M. C. Falub, D. Pacilé, P. Bruno, K. Kern, and M. Grioni, "Giant Spin Splitting through Surface Alloying," Phys. Rev. Lett. **98**, 186807 (2007). https://doi.org/10.1103/PhysRevLett.98.186807
2. D. Hsieh, D. Qian, L. Wray, Y. Xia, Y.S Hor, R.J. Cava, and M.Z. Hasan, "A topological Dirac insulator in a quantum spin Hall phase," Nature **452**, 970(2008). https://doi.org/10.1038/nature06843
3. H. Zhang, C.X Liu, X. L Qi, X.Dai, Z. Fang & S.C Zhang, "Topological insulators in Bi_2Se_3, Bi_2Te_3, and Sb_2Te_3 with a single Dirac cone on the surface", Nature Physics **5**, 438-442(2009). https://doi.org/10.1038/nphys1270
4. S. Murakami, "Quantum Spin Hall Effect and Enhanced Magnetic Response by Spin-Orbit Coupling," Physical Review Letters **97**,236805 (2006). https://doi.org/10.1103/PhysRevLett.97.236805

5. M. Wada, S. Murakami, F. Freimuth, and G. Bihlmayer, “Localized edge states n two-dimensional topological insulators: Ultrathin Bi films” Physical Review B **83**, 121310(R) (2011). https://doi.org/10.1103/PhysRevB.83.121310
6. T.Hirahara, T.Nagao, I.Matsuda, G.Bihlmayer, E.V.Chulkov, Yu.M.Koroteev, P.M. Echenique. M.Saito, and S.Hasegawa, “Role of Spin-orbit coupling and Hybridization effects in the electronic structure of ultrathin Bi films,” Physical Review Letters **97**, 146803(2006). https://doi.org/10.1103/PhysRevLett.97.146803
7. F.Reis, G.Li, L.Dudy, M.Bauernfeind, S.Glass, W.Hanke, R.Thomale, J.Schafer, R.Claessen, “Bimuthene on a SiC substrate: A candidate for a high-temperature quantum spin Hall material”, Science **357**, 287(2017). https://doi.org/aai8142
8. L. Miao, M. Y. Yao, W. Ming, F. Zhu, C. Q. Han, Z. F. Wang, D. D. Guan, C. L. Gao, C. Liu, F. Liu, D. Qian, and J. F. Jia, “Evolution of the electronic structure in ultrathin Bi (111) films”, Physical Review B **91**, 205414(2015). http://dx.doi.org/10.1103/PhysRevB.91.205414
9. L. Nicolaï, J.M. Mariot, U. Djukic, W. Wang, O. Heckmann, M. C. Richter, J. Kanski, M. Leandersson, T. Balasubramanian, J. Sadowski, J. Braun, H. Ebert, I. Vobornik, J. Fujii, J. Minár and K. Hricovini, “Bi ultra-thin crystalline films on InAs(1 1 1)A and B substrates: a combined core-level and valence-band angle-resolved and dichroic photoemission study”, New Journal of Physics **21**, 123012(2019). https://iopscience.iop.org/article/10.1088/1367-2630/ab5c14
10. T. Nagao, J.T.Sadowki, M.Saito, S.Yaginuma, Y.Fujikawa, T.Kogure, T.Ohno, Y.Hasegawa, and T.Sakurai, “Nanofilm allotrope and phase transformation of ultrathin Bi film on Si (111)-7x7” Physical Review Letters **93**, 105501 (2004). https://doi.org/10.1103/PhysRevLett.93.105501
11. C. McGinley, A. A Cafolla, B. Murphy, D. Teehan, P. Moriarty, “The interaction of bismuth with the GaAs (111) B surface”, Applied Surface Science **152**, 169(1999). https://doi.org/10.1016/S0169-4332(99)00311-6
12. S. Cho, Y. Um, Y. kim, G. K. L. Wong, J. B. Ketterson, J. Hong, “Bi epitaxy on polar InSb(111) A/B faces”, Journal of Vacuum Science & Technology A **20**, 1191 (2002). https://doi.org/10.1116/1.1479735

Chapter 2

Chapter 2

Material of interests

2.1 Introduction

In experimental research**,** material selection is a critical step due to the difficulty in changing materials and the necessary preparation required to enter a beamline (BL). Bulk bismuth (Bi) has been extensively used for its unique physical properties, including the highest magnetic susceptibility, highest resistivity, one of the lowest heat conductivities, and the highest hall coefficients. Bi is also the heaviest non-radioactive element and exhibits strong spin-orbit coupling (SOC) [**1, 2],** making it a promising candidate for the quantum hall effect (QHE) and quantum spin hall effect (QSHE), essential physical phenomena for developing next-generation spintronic devices that enable the manipulation of polarized electrons without using a magnetic field. Moreover, Bi is a parent of several topological insulators (TIs). Consequently, most researchers studying Bi have used substrates such as SiC, Bi_2Te_3, Bi_2Se_3, etc. [**3-9**].

However, some researchers choose III-V semiconductors, such as GaAs and InAs, used in the previous thesis [**10-12**]. But my target was the check the ultrathin such as the monolayer to bilayer formation stage, for this purpose the lattice matching is a crucial factor. In such a case, I found that indium antimonide (InSb) is very close almost 0.8%, whereas Chu et al. used InSb to deposit Bi and checked the crystal quality and growth technique [**13**]. Very recently, last year, that is 2021, one result found that they checked the STM structure [**14**] and reported monolayer formation possible, and another result found they checked transport measurement [**15**], and ARPES results in the thicker case by Inbar et al. (2023). Therefore, the unexplored part is the combination of RHEED and ARPES for Bi on InSb growth and electronic structure. This substrate is also attractive due to narrow bandgap semiconductors because of their potential uses for infrared detectors and, as a direct result of their high mobility, in high-speed electronic devices operating at low voltages [**16-21**], and other ultrathin device applications [**22, 23**], and very recently, e.g., as building blocks of quantum computers [**24**], and THz transport waveguides [**25**]. Their small effective mass of 0.014 m_e [**26-28**] also makes them ideal for studying 2D electron gas systems and suitable candidates for Bi growth, and an important point is lattice match [**13**]. Another crucial point is the different rich conditions. However, it is Sb

face; other reconstructions provided different atomic concentrations, in 3x3 reconstruction in In-rich or high-temperature conditions and 2x2 reconstructions in Sb-rich or lower temperatures [**29-31**]. Also, some results show that high-temperature (3x1) phases have been reported at high temperatures [**32, 33**]. In this work, I observed InSb(111)B 3x3(In-rich) and 2x2(Sb-rich) reconstruction. Although both are Sb faces, 2x2 has a more robust trimmer than 3x3[**33**]. From my work, I try to survey the quantum well state (QWS) thickness dependence at $\overline{\Gamma M}$ direction in Bi on InSb (111) B in both reconstructions.

2.2 Substrate Material

Indium Antimony (InSb)

Indium Antimony (InSb) is an III-V semiconductor with protected reversal symmetry and a narrow band gap of 0.17eV at 300K [**34-37**] and 0.23eV at 80K [**38**] (**Fig. 2.1 (a)**). As a semiconductor, its electronic density is null near the Fermi level, as shown in the experimental ARPES measurement at room temperature (300K). It crystallizes in the Zinc-Blende (ZnS) structure, consisting of two different elements distributed in two face-centered cubic lattices with relative translational shifts (1/4, 1/4, 1/4) in the diagonal direction. Its space group is the $F\bar{4}3m$ with the following Wyckoff positions: (0, 0, 0) for In and (1/4, 1/4, 1/4) for Sb. The corresponding lattice parameter is a=6.47Å. The calculated electronic bands in **Fig. 2(a)** show a direct band gap at Γ point of approximately 0.17eV [**26, 39**]. The gap value strongly correlates to the electronegativity of the group V element, i.e., Sb, in this case. If one considers InP, the P is more electronegative, favoring a more substantial charge transfer, increasing the gap [**39**]. In ARPES band dispersion, the light hole is visible, shown in **Fig. 2.1 (b)**, but the heavy hole is not observed, but the top peak is observed at 0.2eV a $\bar{\Gamma}$, which may be a valance band (VB) top and consists of the band gap.

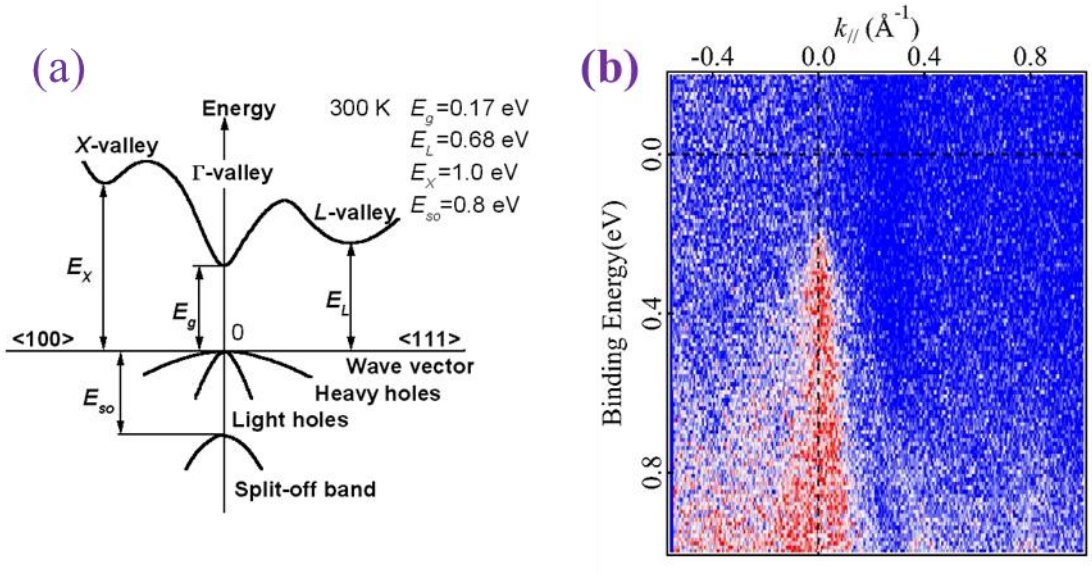

Fig. 2.1 Band Structure of InSb at 300K [26] **(a)** In theory, below the Fermi surface, heavy holes and light holes touch the Fermi level **(b)** In my experiment, observed light holes with a tiny gap from the Fermi level (~200meV) at 40eV linear horizontal light energy.

InSb(111) surface

Atomic structure

The investigation of the polar {111} surfaces dates back to the late 1950s; and both theoretical and experimental information has provided strong evidence that the ideal {111} crystal surfaces exhibit an exciting feature: along a given {111} direction the crystal will always be cation (A) or anion (B) terminated. Therefore, InSb (111) has two different terminations, namely by In or Sb, labeled as the A or B face, respectively. As a result, the A and B surfaces can display different reconstructions under the same preparation protocol. The cover is primarily grown by Molecular Beam Epitaxial (MBE) techniques. At the same time, the InSb(111)A face has 2x2 and $(2\sqrt{3} \times 2\sqrt{3})$R30° reconstruction, as well as 2x2 reconstruction [40-42], and the InSb (111)B face has a (3x3) reconstruction in In-rich or high temperature and 2x2 reconstruction in Sb-rich or lower temperatures (**Fig. 2.2**).

J. Waver previously explained the InSb (111) B-3x3 structure using XRD and STM, where he identified 6-atom rings on top of a slightly bucked InSb top double layer. Two types of rings were found: an elliptic ring composed of 4 In and 2 Sb atoms and a trigonal ring with 3 In and 3 Sb atoms. In addition, this study found that InSb (111) B-3x3 reconstructions have three types of rings, namely α, β, and γ.

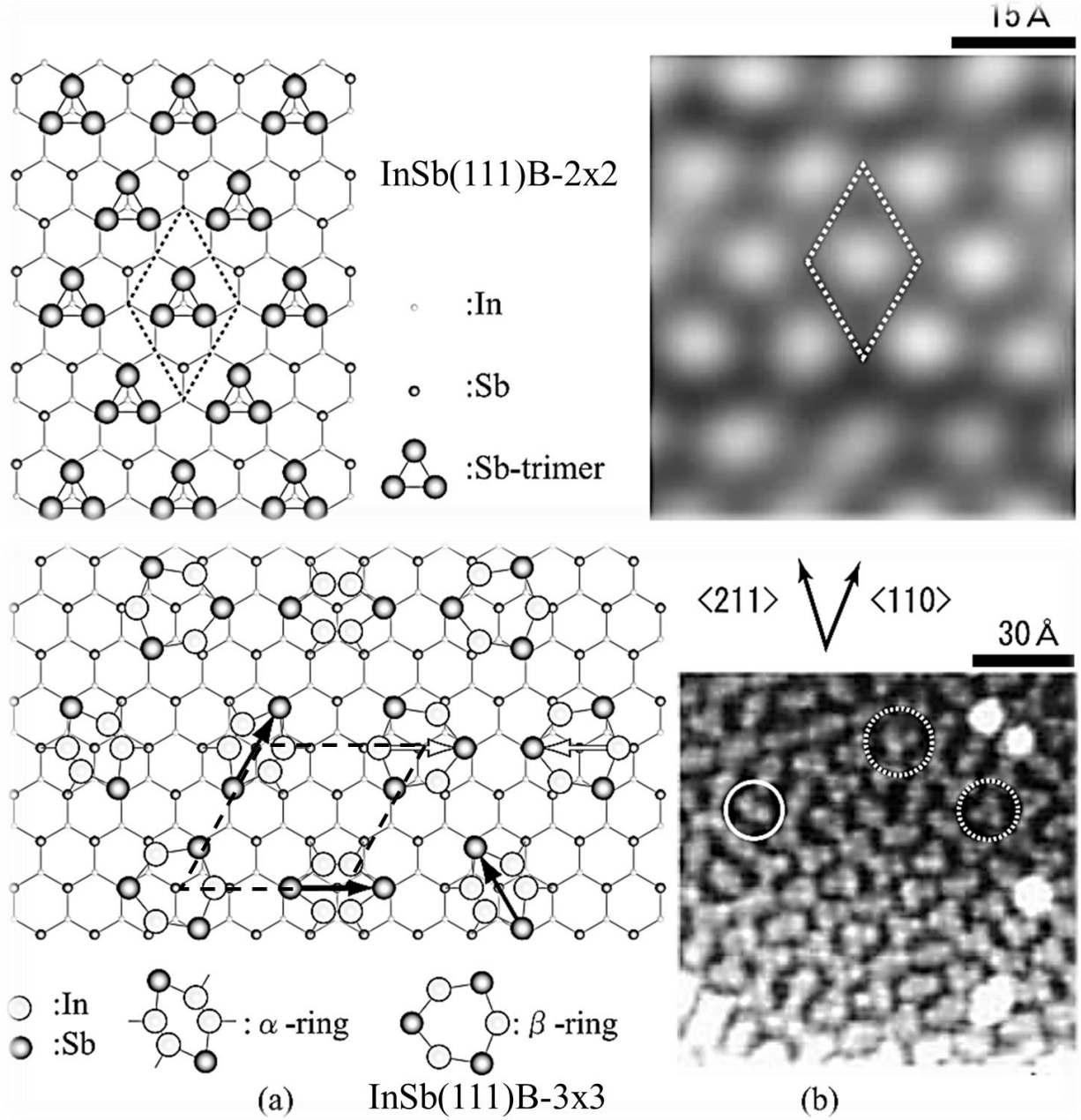

Fig. 2.2. Two stable different reconstructions observed in InSb (111) B surface **(a)** Model of 2x2(top) and 3x3(bottom) reconstructions, **(b)** STM image of the corresponding model. Unit cells (2x2) and (3x3) are highlighted by solid lines [**41**].

On the other hand, the Sb-rich or low-temperature reconstruction has well-known 2x2 reconstructions and a trimmer located in the T_4 site. In this model, the Sb-trimers transfer their excess electronic charge to the rest of the Sb atoms, filling all Sb dangling bonds. This work will investigate the interaction of Bi and Sb under Sb-rich conditions in the 2x2 reconstruction and the In-rich case in 3x3 reconstructions.

Electronic Structure of InSb(111)B

The electronic band structure of InSb has been previously investigated by various researchers [41-45], indicating that it is a direct band gap semiconductor. The lowest direct gap $E_o\Gamma_8\Gamma_{15}) \rightarrow \Gamma_6(\Gamma_1)$ occurs at 0.18 eV, with a SO-splitting gap $E_o + \Delta_o[\Gamma_7\Gamma_{15} \rightarrow \Gamma_6(\Gamma_1)$of 0.99 eV at 300 K (Fig. 2.1). My experimental results align with this finding, presenting a similar effect of approximately 0.2eV in ARPES data along with the corresponding energy distribution curve (EDC) (Fig. 2.3). As a result, two types of holes, heavy and light holes are active near the Fermi surface, with degeneracy near Γ the point.

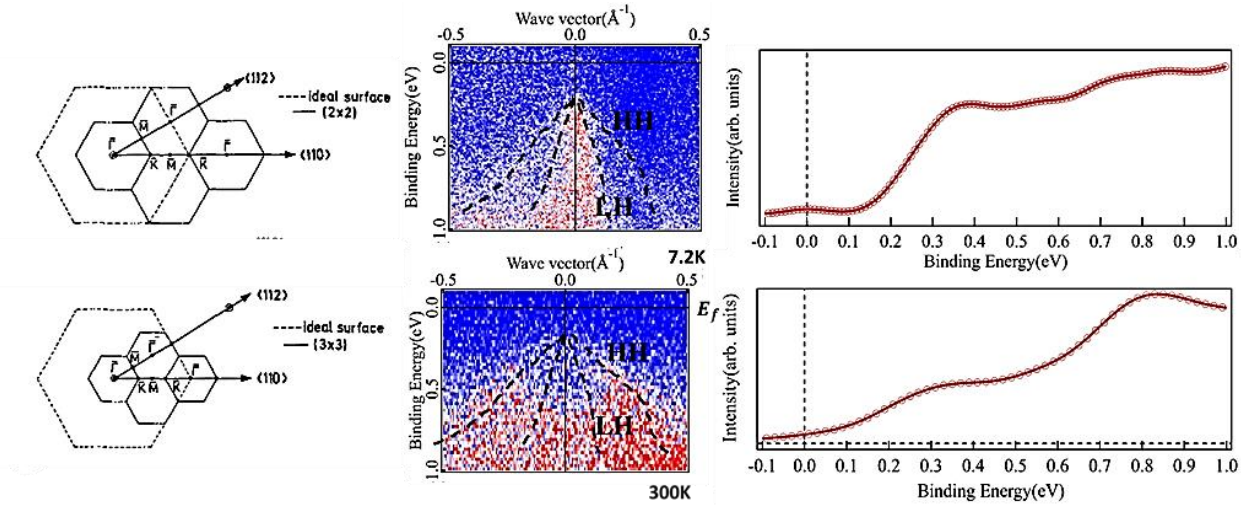

Fig. 2.3 Surface Brillouin zones for the 2×2 and 3×3 reconstructions, corresponding band dispersion, and energy distribution curve (EDC).

The SBZ of the 3×3 and 2×2 reconstructions are illustrated in **Fig. 2.3**, where ΓK denotes the Conner of the hexagon, M represents the middle of each line and is the center of the high symmetry point. All features are nearly identical, with the only distinguishable factor being the size of the hexagon. Thus, both 2×2 and 3×3 exhibit similar electronic characteristics, featuring narrow band gaps, as evidenced by the ARPES data. However, the core-level analysis yielded different results due to variations in atomic position, concentration, and model.

2.3 Deposited material:

Bismuth

For this research purpose, I chose bismuth (Bi) as a deposited material on InSb (111) B substrate since bismuth (Bi) is a group of V atoms in the periodic table and shows semi-metallic behavior. In fundamental physics, we know that, according to the band structure, three different types of material are classified, e.g., metal, semiconductor, and insulator, as shown in **Fig. 2.4 (a)**. In

the case of metal, some overlap, some have zero gaps, and some have narrow gaps. But there are other types of metal known as semi-metals, its properties lie between metal and semiconductor. In the case of bulk, it has an indirect band gap between the conduction band minimum (CBM) and valance band maximum (VBM), which are very sallow near Fermi energy (E_g) (**Fig. 2.4 (a)**).

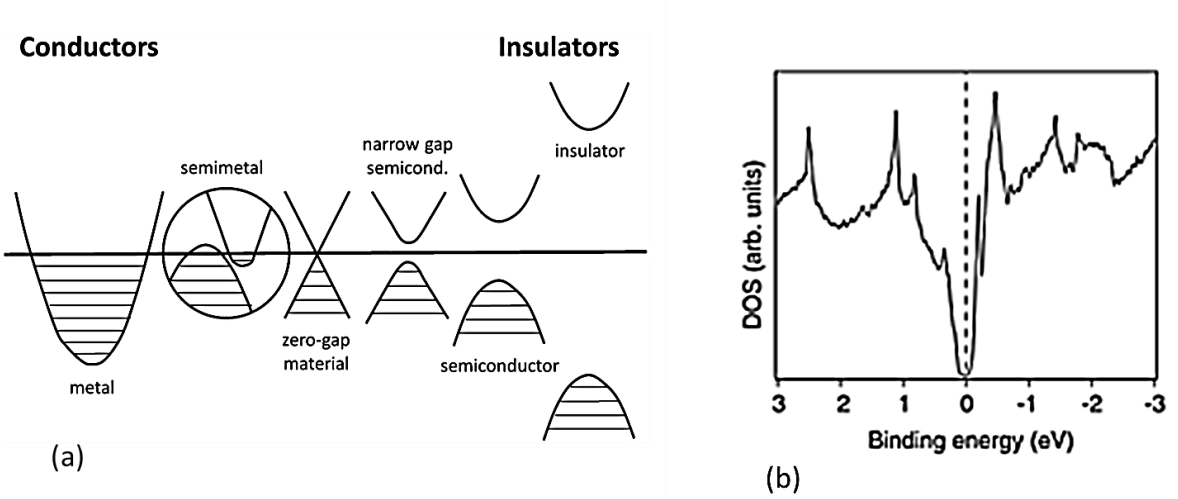

Fig. 2.4. (a) Band Structure of different materials at equilibrium, where the solid line between the CBM and VBM is Fermi level, height is energy is the density of available states. (b) Bulk Bi DOS was calculated with the tight-binding parameters determined by Liu and Allen [**46**].

In contrast, semiconductors are characterized by a relatively small forbidden energy gap between VBM and CBM (generally between 0.1 and 0.2 eV) in the Brillouin zone, whereas metals overlap between CBM and VBM. Semi-metals, on the other hand, have a unique band structure that lies between the two former cases. The Brillouin zone of semi-metals exhibits a band gap, but there is an overlap between the valence and conduction bands at some points. As a result, the DOS of a semi-metal shows a decrease near the Fermi level by several orders of magnitude (without becoming exactly null), as shown in **Fig. 2.4 (b)**.

Bismuth (Bi) is well-known for its significant spin-orbit interaction due to its massive core electrons and heavy non-radioactive properties. As a result, it exhibits a considerable amount of magnetic field without an applied magnetic field, making it an ideal material for demonstrating the quantum hall effect and strong spin-orbit coupling. Previous theoretical studies predict that a 2D Bi film should be a topological insulator (TI) and exhibit topologically protected one-dimensional states at its edges [**3, 4**]. Additionally, it has been observed that alloying Bi with Sb causes a topological phase transition to occur at a specific concentration, x, as seen in the relative alloy which $x \approx 0.04$was the first 3D topological insulator discovered

$Bi_{1-x}Sb_x$[47, 48]. Since Bi is the parent of many Topological Insulators (TI's), it is important to investigate whether a topological phase transition can be observed in Sb-rich conditions. Therefore, Bi and Sb terminated InSb substrates were chosen for this study.

Atomic structure

In this work, I will focus on describing the rhombohedral frame for bulk Bismuth as it provides distinct indices for a specific crystallographic orientation as shown in **Figure. 2.5(a)**. The space group for this frame is R$\bar{3}$m. Throughout this study, I will use the rhombohedral frame and the basis vectors C_1, C_2, and C_3, which correspond to the binary, bisectrix, and trigonal axes respectively, and are depicted in **Figure 2.5 (b)** [2, 49]. It is important to note that while the rhombohedral frame is the most used frame to describe Bismuth, there are also other frames, such as hexagonal and pseudo-cubic, listed in **Table. 2.1**, which can also be used and provide different indices for crystallographic orientations. For a comprehensive overview of the different structures and their corresponding indices, I recommend referring to the review by Hofmann [1]. By focusing on the rhombohedral frame and using the appropriate indices, I can accurately describe the structure of bulk Bismuth and gain a deeper understanding of its crystallographic properties, allowing us to investigate the behavior of ultrathin Bismuth films on InSb substrates and explore their electronic structure and properties.

Overall, the use of the rhombohedral frame provides clarity and consistency in describing the crystallographic orientation of bulk Bismuth. By focusing on this frame and using appropriate indices, I can accurately analyze and interpret experimental and theoretical results throughout this study.

The use of the rhombohedral frame enables us to see that the Bi (111) bilayer unit cell is composed of two atoms, as shown in **Fig. 2.7**, with one atom located at the corners and the other near the center. The elongated cube has a ratio of d1/d2 = 0.88 for each side length, and the lattice parameter a_{rh} is 4.7236 Å at 4.5 K [50, 51]. Because $d_1 = d_2$, the atom near the center of the rhombohedron has only three nearest neighbors and a set of three second-nearest neighbors. The bilayers are arranged along the [111] direction, and the first nearest neighbors are strongly bonded through covalent bonds.

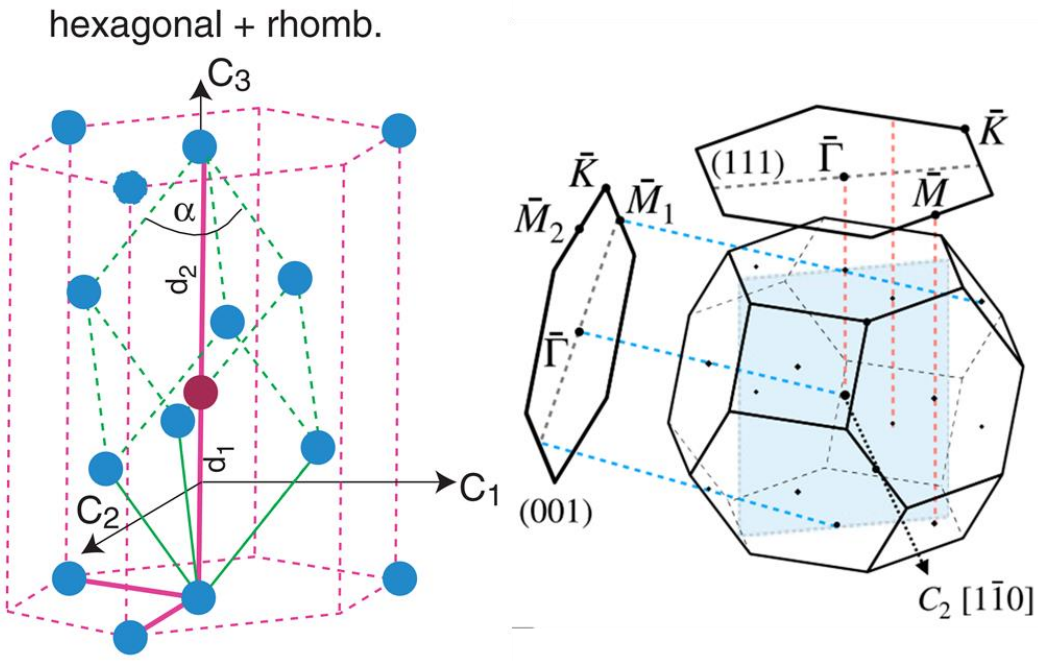

Fig. 2.5. Bi crystal structure from a different direction, (a) atomic position, (b) Brillouin zone **[2].**

Table. 2.1 Comparison between two different notations (111) and (001) [2].

Notation	Bi (111)	Bi (001)
Lattice System	Rhombohedral	Hexagonal
Axes	Trigonal (C_3, z)	Trigonal (C_3, z)
Atom (Per unit cell)	2	6
Length ratio (d_1/d_2)	0.88	1
Angle (α)	57.35^{o}	60^{o}
Bilayer height	3.9Å	3.9Å
Lattice constant	4.53Å	4.53Å
Space group	R$\bar{3}$m (166)	R3m (160)

The primitive vectors of the rhombohedral unit cell can be expressed as follows:

$$a_1 = \left(-\frac{1}{2}a, -\frac{\sqrt{3}}{6}a, \frac{1}{3}c\right) \quad a_2 = \left(-\frac{1}{2}a, -\frac{\sqrt{3}}{6}a, \frac{1}{3}c\right) \quad a_3 = \left(0, -\frac{\sqrt{3}}{3}a, \frac{1}{3}c\right) \qquad (1.12)$$

Where a=4.5332Å and c=11.7967Å represent the lattice parameters in the hexagonal frame, as mentioned previously in the text.

Electronic properties

Electronic properties are a crucial factor in understanding the behavior and state of electrons in a material. Bulk Brillouin Zone (BBZ) is essential for this purpose, and the Bi structure shows regular face-center cubic, which can be indicated as the BBZ of the A7 Arsenic structure, as shown in **Fig. 2.7**. The real space structure of Bi is the rhombohedral structure with $\alpha = 57.35^{\circ}$ and d1/d2 = 0.88, which is responsible for its semi-metallic behavior. The calculated band from **Fig. 2.6** shows a band gap, but some bands intercept the Fermi level close to high-symmetry points. The bands under the Fermi level EF consist of 2 s bands and 3 p bands, with the last p band intercepting EF and giving rise to electron and hole pockets at L and T high symmetry points, respectively. Above EF, the three bands correspond to 3 other p bands. The s bands, which have the angular momentum l=0, are not influenced much by SOC (red bars) [**2**].

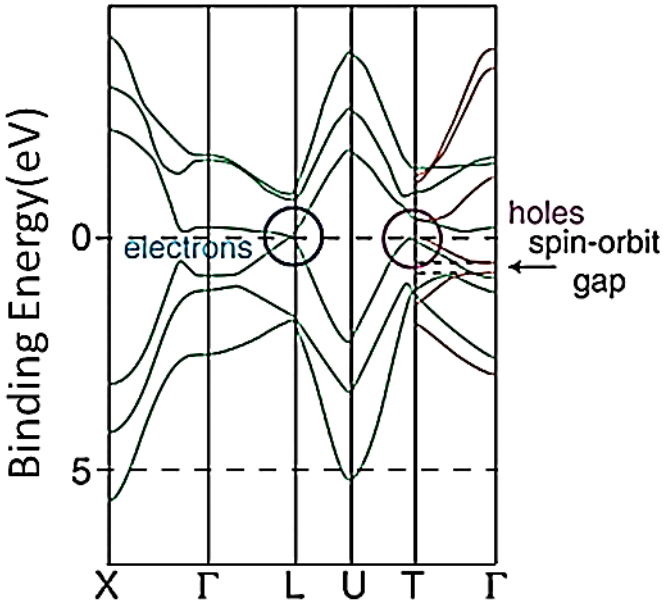

Fig. 2.6. Calculated Bi band structure taken from [**46**].

On the other hand, although SOC has a considerable effect on several p bands and the hole pocket at T, it does not lift spin degeneracy due to the bulk symmetry of Bi [**1, 53**]. However, the vacuum/material interface breaks the symmetry of Bi when studying specific surfaces, ultimately causing band splitting when combined with SOC contributions.

Bi (111) surface

Atomic structure

Bi consists of bilayers stacked in the [111] direction, with atomic bonds strongly linked between each bilayer through covalent bonding. This unique arrangement allows for a natural cleavage

plane along the [111] direction, making it the favored direction for epitaxial growth. Choosing Bi as the material is ideal due to these properties. The hexagonal structure observed on the Bi (111) surface, as depicted in **Fig. 2.7(a)**, is composed of two layers forming a single bilayer (BL). When viewed from the side **(Fig. 2.7(b))**, the bilayers are weakly interconnected by van der Waals-like bonds [2]. Consequently, epitaxial growth or cleavage of this surface results in a terminus characterized by a complete BL layer. Surface reconstructions are typically absent in this system, as the only degree of freedom is the inter-bilayer distance at the surface, which differs from the bulk by less than 2% at 140K [52].

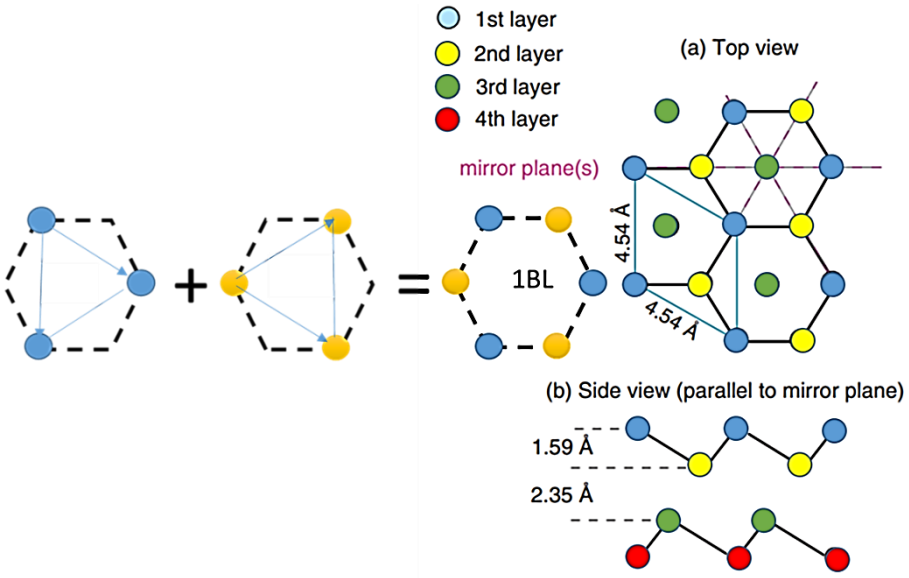

Fig. 2.7. Bi bilayer formation, (a) 1BL case, (b) top view of the multi-BL case, and each layer consisting of a 2D trigonal lattice, the solid lines indicate covalent bonds between the atoms with the BL and dashed lines indicate the mirror planes of the structure, (c) side view [1].

Electronic structure

Bismuth is a well-known element due to its unique surface state [2] and is the first experimentally confirmed 3D TI $Bi_{1-x}Sb_x$ alloy [47]. However, its surface state is extremely robust, and bulk Bi is theoretically topologically trivial, leading to disagreement between the calculated band structure and experimental results. Additionally, Bi has the strongest SOC among non-radioactive atoms, making it a subject of intense study for understanding the effects of SOC, $\bar{M}$ particularly near the conduction band (CBM) and valence band (VBM) with only a 10meV difference. These properties make Bi an attractive candidate for integration into new fields, such as spintronics, and the combination of experimental angle-resolved photoemission spectroscopy (ARPES) measurements with theoretical first-principles calculations is a highly effective means of investigation.

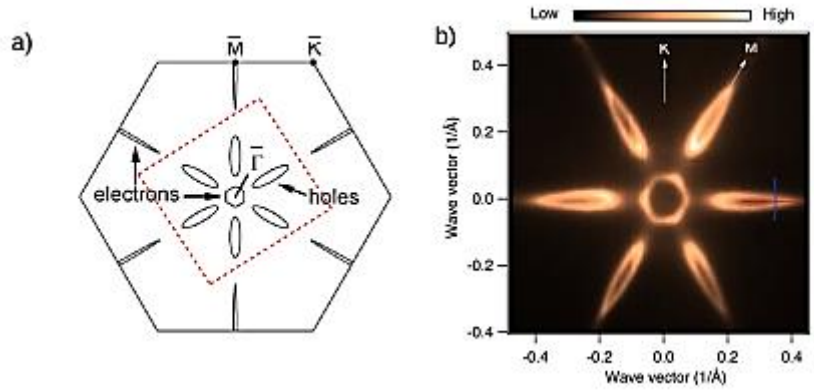

Fig. 2.8. The schematic drawing of the bulk Brillouin zone for Bi (111), where the hole and electron pockets are drawn along a specific direction (source [**53**]), (b) A Fermi surface mapping was measured using circularly polarized light exhibiting an electron pocket at the Γ point and six-hole pockets in the $\overline{\Gamma M}$ directions within a six-fold symmetry (from [**54**]). The photon energy used for the spectra is $h\nu = 18eV$.

Fig. 2.8 depicts the bulk Brillouin zone, which exhibits a 3-fold symmetry that is transformed into a 6-fold symmetry when projected onto the (111) plane. A Fermi Surface mapping conducted using ARPES techniques on Bi crystals reveals a single electron pocket centered at the Γ point and six-hole pockets in the directions, separated by an angle of 60◦, as shown in **Fig. 2.8 (b)**. The dispersions of the hole and electron pocket bands are highlighted in the $\overline{\Gamma M}$ cross-section displayed in **Fig. 2.9 (b)**.

To understand the role of SOC in Bi band dispersion, a theoretical understanding of the Bi crystal is crucial. Koroteev et al. [**55**] conducted a study where ARPES measurements and first-principles calculations were compared by superimposing along $\overline{\Gamma M}$ and $\overline{\Gamma K}$ directions. Bi's time-reversal symmetry, i.e., (k, ↑) = (−k, ↓), and inversion symmetry, i.e., (k, ↑) = (−k, ↑) [**56**], both hold simultaneously, making the states doubly degenerate within the bulk. However, the inversion symmetry is broken at the surface, and the surface can be viewed as a 2D free electron gas that experiences a potential varying along the normal to the surface. Consequently, the electrons from the surface plane are immersed in a magnetic field, which interacts differently, in the relativistic case, with the two different spins (↑ and ↓), resulting in a band splitting. Calculations were conducted with and without the SOC terms, and **Fig. 2.9 (a) shows** that SOC splits the surface states in both $\overline{\Gamma M}$ and $\overline{\Gamma K}$ directions. The degeneracy persists only at the Γ point vicinity and the $\bar{M}$ point. The latter case is explained because $\bar{M}$ is a surface TRIM point halfway between two Γ points [**1**]. The states near the $\bar{M}$ point are reported to be more surface resonance states, i.e., states that share energy levels with pristine bulk states [**53**]

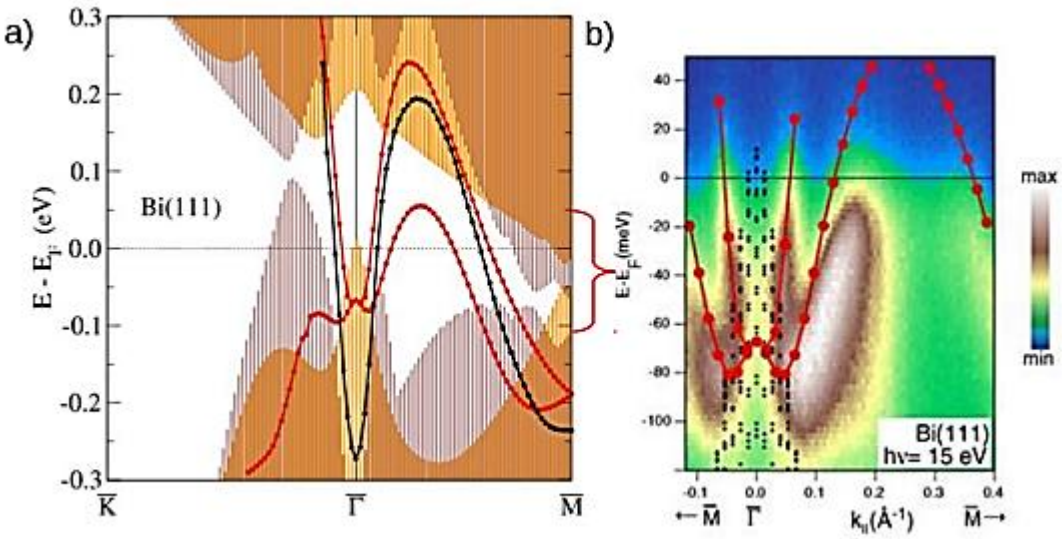

Fig. 2.9. (a) The superimposed between the theoretical calculation in the projected bulk state from a tight-banding model, and (b) experimental results at 15eV, along $\overline{\Gamma M}$ and $\overline{\Gamma K}$ direction, where the surface bands without (black) and with (red) SOC-induced splitting and the projected bulk bands without (violet) and with (yellow) SOC, their overlap being in brown, demonstrate the high importance of Spin-Orbit Splitting [**55**].

In a previous report, ultrathin films of intrinsic Bi were deposited mainly on Si (111) 7 × 7 substrate, where quantum-sized effects occurred, and a thickness dependency was identified. These phenomena were first observed by Hirahara et al. [**3, 57- 59**], who suggested thickness-dependent Quantum well states in ultrathin films of Bi. Due to its large Fermi wavelength λ_F = 30 nm, Bi exhibits quantum-sized effects in thin films with a thickness of d ~ λF, resulting in the formation of QWS as shown in **Fig. 2.10**. Relativistic first-principles calculations show that the QWS in these Bi thin films is completely spin-degenerated [**3**], which contradicts Rashba split states. This suggests that these thin films have a weak interaction with the substrate as if no inversion symmetry breaking is occurring. However, QWS hybridized with Rashba surface states, close to the M high-symmetry point, leading to the lifting of the spin splitting of the surface states where the Rashba effect appears to be predominated by the parity effect [**59**].

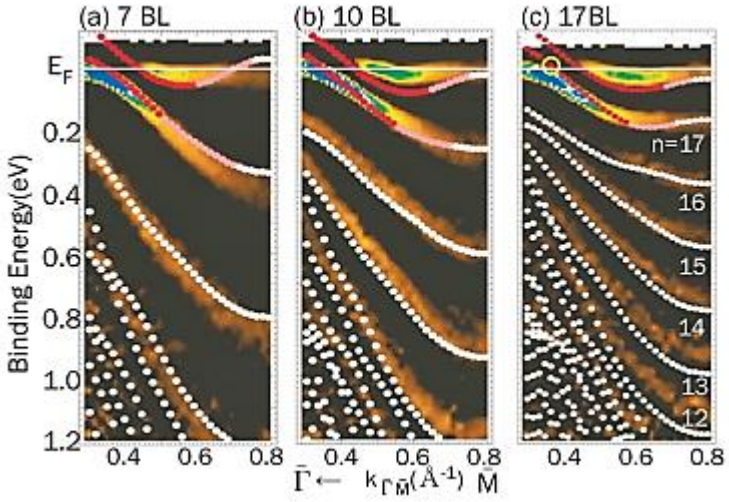

Fig. 2.10. Thickness-dependent QWS observed in band dispersion measured on the Bi/Si (111) 7×7 from Hirahara et al. [**3**] of the Bi thin film. The number of QWS increases with the number of bilayers of Bi.

On the other hand, Takayama et al. [**60-62**] confirmed the existence of one-dimensional edge states by analyzing the spin polarization of the electronic band as a function of film thickness [**Fig. 2.11**]. They observed that the edge states disappear when going towards 8 BL. However, the Rashba spin-polarized states, which are still distinguishable at 40 MLs, begin to hybridize with each other until they strictly overlap slowly.

Additionally, the Bi/Si (111) system displays an asymmetry in the in-plane spin polarization of the Rashba surface states within Bi [**62**]. Furthermore, depositing around 15 bilayers of Bi on Si (111) leads to the formation of islands on the topmost layer arranged in a triangular shape, exhibiting one-dimensional edge states with Rashba spin splitting **[61]** as depicted in **Fig. 2.11**. Bi has been proposed as a potential Topological Insulator in previous studies, but experimental verification of this phase of matter is still outstanding. Theoretical research is working on identifying suitable substrates and delving into the limits of the predicted non-trivial phase of Bi.

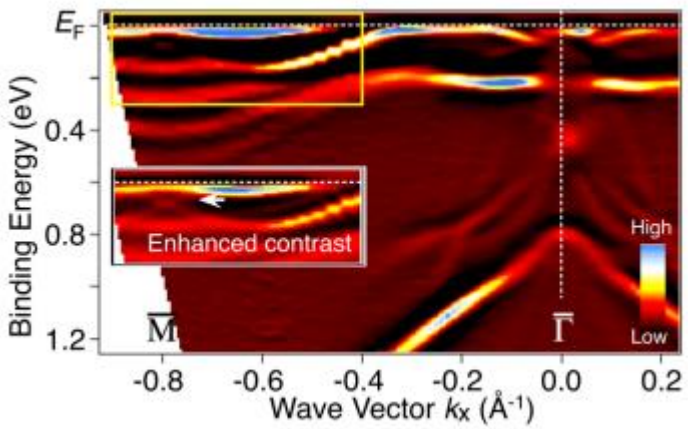

Fig. 2.11. One dimensional edge state was observed in band dispersion along $\overline{\Gamma M}$ measured on the Bi/Si (111) 7 × 7 from Takayama et al. [**61**].

Fig. 2.12(a) is an example of such a study that simulated a ribbon of a single bilayer of Bi (111) using a tight-binding model [**63**]. The study found that both zigzag and armchair terminated edges are Quantum Spin Hall (QSH) systems, with a non-trivial Z_2 number $\nu = 1$ determined using the "parity method" [**65**]. Surface states, corresponding to edge states, were found to lie within the bulk band gap and were determined to be well-localized, with a penetration depth of only a few lattice constants. The study theorizes that this localization in k-space means de-localization in real space and that the minimal size of the system to get the QSH effect is expressed by this distance. The simple Bi (111) bilayer system is also reportedly resistant to magnetic disorder as only a portion of the bulk states vanish when magnetic impurities are introduced, while a part of the edge states remains.

Another theoretical study [**64**] investigated the effect of inter-bilayer distance on the strength of the inter-bilayer bonding and its influence on film thickness. **Fig. 2.12 (c)** presents the results of band calculations performed using a first-principles method and varying the inter-bilayer distance for 2 (top row) or 3 (bottom row) BL systems. The study found that the inter-bilayer energy bond is an essential parameter for the 2D TI phase of Bi, with an intermediate energy bond of 0.3-0.5 eV/bond, stronger than van der Waals bonds but weaker than usual chemical bonds. The energy band gap closes for both systems from the case $\Delta d2 = 2$ Å and reopens when the distance increases further. Only the 2-bilayer system showed a parity exchange when the gap closed, indicating a change of Z_2 topological number ν from 1 to 0, implying a transformation from non-trivial to trivial. The authors determined ν for a system of up to 8 bilayers and found that the thin films were non-trivial each time, suggesting that non-triviality does not depend on the film thickness (up to the 3D limit). This finding contradicts a previous

study that predicted an oscillation between non-trivial and trivial topological numbers with an increase in the number of bilayers [66]. The authors estimate that 1- to 4-bilayer systems are intrinsic 2D TIs, whereas 5- to 8-bilayer systems are 2D TIs squeezed between two non-trivial metallic layers, with the latter case reaching the computational power limitation.

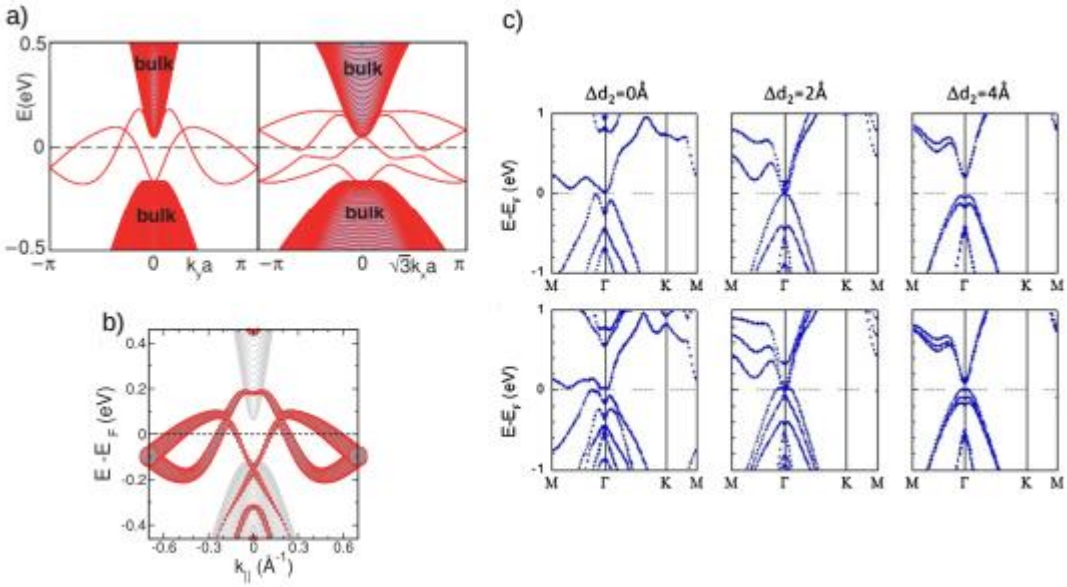

Fig. 2.12. Energy bands were calculated using a tight binding model (a) for ribbons with surface states intercepting EF within the bulk band gap, for zigzag edge (left) and armchair edge (right) cases, and first-principles calculations (b) confirming the band dispersion for the zigzag case (from [63]). Electronic bands calculated (c) considering only 2 BL (upper row) and 3 BL (lower row) with different inter-BL distances [64]: a closing and re-opening of the band gap are shown in both cases.

In a recent study, Inbar et al. [67], presented new findings on the Bi/InSb system in higher BL shown in **Fig. 2.13**. The study investigated the surface states and quantum-well states of ultrathin Bi (111) films with varying thicknesses using ARPES measurements. The Fermi surface of the 5.4 BL thick Bi (111) film at E_F (**Fig. 2.13(a))** demonstrates the presence of surface states, which RHEED suggests, may exist at even greater thicknesses. This confirms the topological nature of the Bi film and supports previous studies suggesting the existence of topologically non-trivial states in Bi films. The observation of surface state band degeneracy at $\bar{M}$ (**Fig. 2.13 (b and c)**), indicated by X, further supports the breaking of inversion symmetry. Interestingly, as the film thickness decreases, the separation between the Fermi level crossings near $\bar{M}$ decreases (**Fig. 2.13(d**)), suggesting that the surface states become more confined or localized with decreasing film thickness, consistent with the expected behavior of quantum-

well states. The energy distribution curves at the $\bar{M}$ point (**Fig. 2.13(e))** provide further insight into the energies of the quantum-well states.

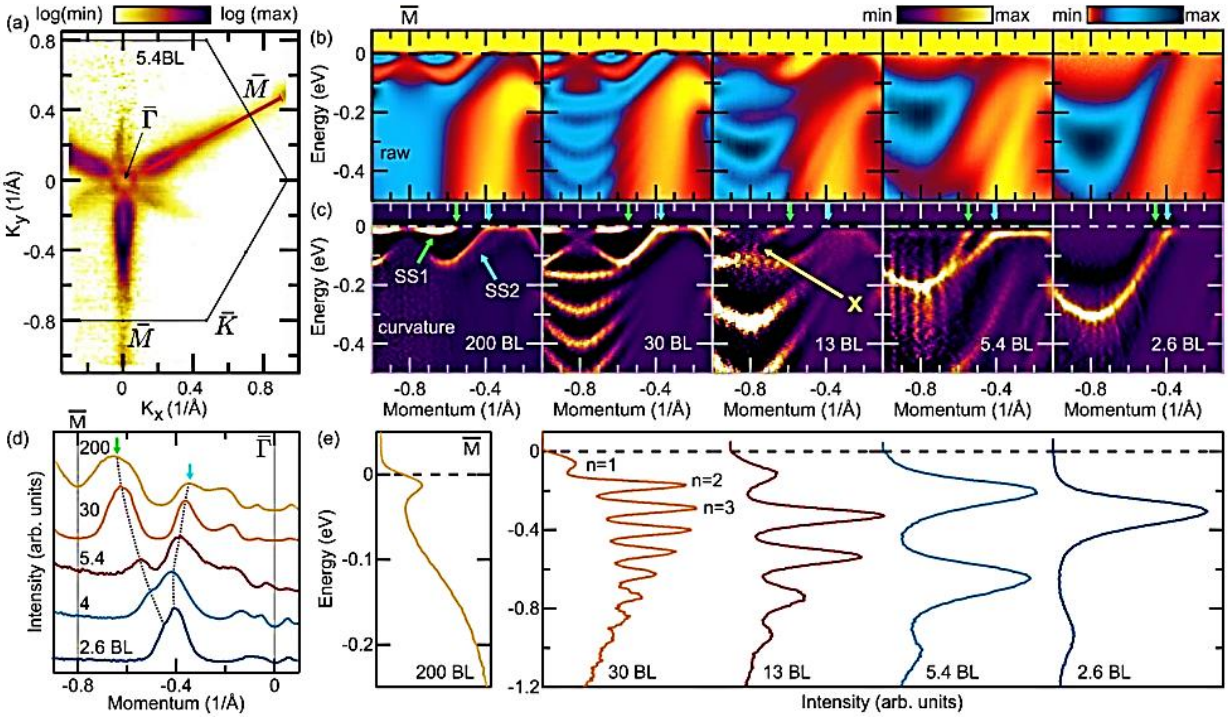

Fig. 2.13. The ARPES measurements were conducted using an incident photon energy of 37.5 eV. In panel (a), the Fermi surface of a 5.4 atomic layer (BL) thick Bi (111) film. The corresponding energy-momentum (E-k) cuts along the $\overline{\Gamma M}$ path are highlighted in panels (b) and (c). Panels (b) and (c) display the raw ARPES images and curvature plots, respectively, enhancing the dispersive features of the surface states. The surface state band degeneracy at $\bar{M}(k = 0.8\text{Å}^{-1})$, indicated by X, is observed because of the breaking of inversion symmetry. Panel (d) presents the momentum distribution curves at E_F, showing the Fermi level crossings of the surface states near $\bar{M}$. The crossings, highlighted by arrows in panels (c) and (d), exhibit a decreasing separation as the films become thinner. Panel (e) shows the energy distribution curves at the $\bar{M}$ point, displaying the energies of the quantum-well states that are further analyzed in Figure 4(e) of the study.

These findings have significant implications for the understanding and potential applications of ultrathin Bi films. However, the observations of surface states and the breaking of inversion symmetry in Bi films are limited to films thicker than 2.6BL, as no ARPES results were shown for thinner films. Therefore, the long-debated problem of the semi-metal to semiconductor transition in the ultrathin Bi (111) case remains unsolved. Nevertheless, these findings are promising for higher BL cases, where they solve another debated problem of whether bulk Bi

(111) is topologically trivial or non-trivial. However, I have some questions about their funding because the low temperature is more suitable for checking the QWS state character rather than the SS character. In the ultrathin case, the decreasing separation between Fermi level crossings with decreasing film thickness indicates the confinement of surface states in ultrathin films. Additionally, the presence of quantum-well states suggests that the properties of Bi films can be tuned by controlling the film thickness, opening possibilities for engineering the band structure and surface properties of ultrathin Bi films. This could pave the way for the realization of novel electronic and optoelectronic devices.

Therefore, the findings contribute to a deeper understanding of the surface states and quantum-well states in ultrathin Bi films, but it should be noted that the observations of surface states and the breaking of inversion symmetry are limited to films thicker than 2.6BL. However, it has been shown that new surface states can be observed in films as thin as 1 BL, which highlights the potential for tailoring the properties of Bi films through controlled film thickness. These insights provide valuable guidance for the design and development of future topological and spintronic devices.

2.4 Reference

1. Rumble J R (ed) 2018 CRC Handbook of Chemistry and Physics 99th edn (Boca Raton, FL: CRC Press).

   https://edisciplinas.usp.br/pluginfile.php/4557662/mod_resource/content/1/CRC%20Handbook%20of%20Chemistry%20and%20Physics%2095th%20Edition.pdf

2. Ph. Hofmann “The surfaces of bismuth: Structural and electronic properties”, Surface Science **81**, 191–245 (2006). https://doi.org/10.1016/j.progsurf.2006.03.001

3. T. Hirahara, T. Nagao, I. Matsuda, G. Bihlmayer, E. V. Chulkov, Y. M. Koroteev, P.M. Echenique, M. Saito, and S. Hasegawa, “Role of Spin-orbit coupling and Hybridization effects in the electronic structure of ultrathin Bi films”, Physical Review Letters **97**, 146803 (2006). https://doi.org/10.1103/PhysRevLett.97.146803

4. F. Reis, G. Li, L. Dudy, M. Bauernfeind, S. Glass, W. Hanke, R. Thomale, J. Schafer, R. Claessen, “Bimuthene on a SiC substrate: A candidate for a high-temperature quantum spin Hall material”, Science **357**, 287-290 (2017). https://doi.org/aai8142

5. T. Hirahara, G. Bihlmayer, Y. Sakamoto, M. Yamada, H. Miyazaki, S. Kimura, S. Blugel, and S. Hasegawa, “Interfacing 2D and 3D Topological Insulators: Bi (111)

Bilayer on Bi2Te3", Physical Review Letters **107**, 166801 (2011). https://doi.org/10.1103/PhysRevLett.107.166801

6. Y. L. Chen, J. G. Analytis, J. H. Chu, Z. K. Liu, S. K. Mo, X. L. Qi, H. J. Zhang, D. H. Lu, X. Dai, Z. Fang, S. C. Zhang, I. R. Fisher, Z. Hussain, Z. X. Shen, "Experimental Realization of a 3DTI, Bi2Te3", Science **325**, 178 (2009). https://doi.org/10.1126/science.1173034

7. T. Hirahara, N. Fukui, T. Shirasawa, M. Yamada, M. Aitani, H. Miyazaki, M. Matsunami, S. Kimura, T. Takahashi, S. Hasegawa, and K. Kobayashi, "Atomic and Electronic Structure of Ultrathin Bi (111) Films Grown on Bi2Te3(111) Substrates: Evidence for a Strain-Induced Topological Phase Transition", Physical Review Letters **109**, 227401 (2012). https://doi.org/10.1103/PhysRevLett.109.227401

8. M. –Y. Yao, F. Zhu, C. Q. Han, D. D. Guan, C. Liu, D. Qian, and J. –F. Jia, "Topologically nontrivial bismuth (111) thin films Grown on Bi2Te3", Scientific Reports **6**, 21326 (2016). https://doi.org/10.1038/srep21326

9. M. Chen, J. –P. Peng, H. –M. Zhang, L.-L. Wang, K. He, X.-C. Ma, and Q. –K. Xue, "Molecular beam epitaxy of bilayer Bi (111) films on topological insulator Bi2Te3: A scanning tunneling microscopy study", Applied Physics Letters **101**, 081603 (2012). https://doi.org/10.1063/1.4747715

10. C. McGinley, A. A. Cafolla, B. Murphy, D. Teehan, P. Moriarty, "The interaction of bismuth with the GaAs (111) B surface", Applied Surface Science **152**, 169-176 (1999). https://doi.org/10.1016/S0169-4332(99)00311-6

11. M. C. Richter, J. M. Mariot, M. A. Gafoor, L. Nicolaï, O. Heckmann, U. Djukic, W. Ndiaye, I. Vobornik, J. Fujii, N. Barrett, V. Feyerg, C. M. Schneider, K. Hricovini, "Bi atoms mobility-driven circular domains at the Bi/InAs (111) interface", Surface Science **651**, 147-153 (2016). https://doi.org/10.1016/j.susc.2016.03.032

12. L. Nicolaï, J. –M. Mariot, U. Djukic, W. Wang, O. Heckmann, M. C. Richter, J. Kanski, M. Leandersson, T. Balasubramanian, J. Sadowski, J. Braun, H. Ebert, I. Vobornik, J. Fujii, J. Minár and K. Hricovini, "Bi ultra-thin crystalline films on InAs(1 1 1)A and B substrates: a combined core-level and valence-band angle-resolved and dichroic photoemission study", New Journal of Physics **21**, 123012 (2019). https://iopscience.iop.org/article/10.1088/1367-2630/ab5c14/meta

13. S. Cho, Y. Um, Y. Kim, G. K. L. Wong, J. B. Ketterson, J. Hong, “Bi epitaxy on polar InSb(111) A/B faces”, Journal of Vacuum Science & Technology A **20**, 1191 (2002). https://doi.org/10.1116/1.1479735

14. C. Liu, Y. Zhou, G. Wang, Y. Yin, C. Li, H. Huang, D. Guan, Y. Li, S. Wang, H. Zheng, C. Liu, Y. Han, J. W. Evans, F. Liu, and J. Jia, “Sierpiński Structure and Electronic Topology in Bi Thin Films on InSb(111)B Surfaces”, Physical Review Letter **126**, 176102 (2021). https://dx.doi.org/10.1103/PhysRevLett.126.176102

15. Z. Jiang, Ph.D. dissertation, Virginia Polytec & State Uni.A M Jean-Louis, C Hanlon Phys Status Solidi **34** (1969) 329.

16. D. Alamo, J. A., “Nanometer-scale electronics with III-V compound semiconductors”, Nature **479**, 317–323(2011).

17. K. Tomioka, M. Yoshimura, and T. A. Fukui, “III-V nanowire channel on silicon for high-performance vertical transistors”, Nature **488**, 189–192, https://doi.org/10.1038/nature11293

18. S. Oktyabrsky, and P. D. Ye, “Fundamentals of III–V Semiconductor MOSFETs” Springer, 2010. https://www.studmed.ru/oktyabrsky-s-ye-pd-eds-fundamentals-of-iii-v-semiconductor-mosfets_cbda347b8eb.html

19. Mimura, T., Hiyamizu, S., Fujii, T. & Nanbu, K., “A new field-effect transistor with selectively doped GaAs/n-AlxGa1−xAs heterojunctions”, Jpn. J. Applied Physics **19**, L225–L227(1980).

20. Bennett, B. R., Magno, R., Boos, J. B., Kruppa, W. & Ancona, M. G., “Antimonide-based compound semiconductors for electronic devices: A review” Solid-State Electron **49**, 1875–1895(2005). http://dx.doi.org/10.1016/j.sse.2005.09.008

21. Martinez-Blanque, C. et al. “Electrostatic performance of InSb, GaSb, Si and Ge p-channel nanowires” J. Phys. D: Appl. Phys. 50, 495106 (2017). https://iopscience.iop.org/article/10.1088/1361-6463/aa9543/meta

22. J. L Webb, J. Knutsson, M. Hjort, S. G. Ghalamestani, K. A. Dick, R. Timm, and Anders Mikkelsen “Electrical and surface properties of InAs/InSb nanowires cleaned by atomic hydrogen” Nano Letter **15**, 4865–4875 (2015). https://pubs.acs.org/doi/epdf/10.1021/acs.nanolett.5b00282

23. J. L. Webb, J. Knutsson, M. Hjort, S. R. McKibbin, S. Lehmann, C. Thelander, K. A. Dick, R. Timm, and A. Mikkelsen "Imaging atomic scale dynamics on III-V nanowire surfaces during electrical operation", Scientific Reports **7,** 12790 (2017).

24. Ö. Gül, H. Zhang, F. K. de Vries, J. V. Veen, K. Zuo, V. Mourik, S. Conesa-Boj, M. P. Nowak, D. J. van Woerkom, M. Quintero-Pérez, M. C. Cassidy, A. Geresdi, S. Koelling, D. Car, S. R. Plissard, E. P. A. M. Bakkers, and L. P. Kouwenhoven "Hard superconducting gap in InSb nanowires", Nano Letter **17**, 2690–2696 (2017). https://doi.org/10.1021/acs.nanolett.7b00540

25. Y. Ma, J. Zhou, J. Pištora, M. Eldlio, N. Nguyen-Huu, H. Maeda, Q. Wu, and M. Cada "Subwavelength InSb-based slot waveguides for THz transport: concept and practical implementations", Scientific Reports **6**, 38784(2016). https://doi.org/10.1016/j.rinp.2020.103299

26. W. Liu, A.Y. Chang, R.D. Schaller, D.V. Talapin, Colloidal InSb nanocrystals, J. Am. Chem. Soc. **134**, 20258e20261(2012). https://doi.org/10.1021/ja309821j

27. F.W. Wise, Lead salt quantum dots: the limit of strong quantum confinement, Accounts Chem. Res. **33**, 773e780 (2000). https://doi.org/10.1021/ar970220q

28. A. Yoffe, Low-dimensional systems: quantum size effects and electronic properties of semiconductor microcrystallites (zero-dimensional systems) and some quasi-two-dimensional systems, Adv. Phys. **42,** 173e262 (1993). https://ui.adsabs.harvard.edu/link_gateway/2002AdPhy..51..799Y/doi:10.1080/00018730110117451

29. Hernández-Calderón, I. & Höchst, H. Angle-resolved photoemission of α-Sn (111) and the polar (111) and (111) surfaces of InSb. Surf. Sci. 152–153, 1035–1041. https://doi.org/10.1016/0039-6028(85)90518-7

30. Nakada, T. & Osaka, T. Sb trimer structure of the InSb(111)B-(2 × 2) surface as determined by transmission electron diffraction. Physical Review Letter 67, 2834–2837. https://doi.org/10.1103/PhysRevLett.67.2834

31. J. Wever, H.L. Meyerheim, W. Moritz, V. Jahns, D. Wolf, H. Schulz, L. Seehofer, R.L. Johnson, "A new type of reconstruction on the InSb(111)B surface determined by grazing incidence x-ray diffraction", Surface Science 321, L225(1994). https://epub.ub.uni-muenchen.de/5874/1/Moritz_Wolfgang_5874.pdf

32. A. J. Noreika, M. H. Francombe, and C. E. C Wood, “Growth of Sb and InSb by molecular beam epitaxy”, Journal of Applied Physics **52**, 7416–7420.

33. K. Oe, S. Ando, and K. Sugiyama, “RHEED study of InSb films grown by molecular beam epitaxy”, Japan Journal of Applied Physics **19**, L417 (1981). https://iopscience.iop.org/article/10.1143/JJAP.19.L417/pdf

34. C.B.M. Andersson, U.O. Karlsson, M.C. Hgtkansson, L.O. Olsson, L. Ilver, J. Kanski, P.-O. Nilsson, “Surface atomic structure of InAs (111) B-2 x 2 and InSb(111)B-2 x 2 studied by core level spectroscopy”, Surface Science **347**, 190-206 (1996). https://doi.org/10.1016/0039-6028(95)00972-8

35. W. Liu, A.Y. Chang, R.D. Schaller, D.V. Talapin, Colloidal InSb nanocrystals, J. Am. Chem. Soc. **134**, 20258e20261 (2012). https://doi.org/10.1021/ja309821j

36. M.I. Khan, X. Wang, K. Bozhilov, C.S. Ozkan, Templated fabrication of InSb nanowires for nanoelectronics, J. Nanomater. 2008 (2008). https://doi.org/10.1155/2008/698759

37. S. Yamaguchi, T. Matsumoto, J. Yamazaki, N. Kaiwa, A. Yamamoto, Thermoelectric properties, and figure of merit of a Te-doped InSb bulk single crystal, Appl. Phys. Lett. 87 (20) (2005) 201902. https://doi.org/10.1063/1.2130390

38. Y. Yang, L. Li, X. Huang, G. Li, L. Zhang, Fabrication, and optical property of single-crystalline InSb nanowire arrays, J. Mater. Sci. 42 (8) (2007) 2753e2757. http://dx.doi.org/10.1007/s10853-006-1272-4

39. A. Rahul, R. Verma, S. Tripathi, Vishwakarma, Effect of substrate temperature on the electrical and optical properties of electron beam evaporated indium antimonide thin films, Mater. Pol. 30 (4) (2012) 375e381. https://doi.org/10.2478/s13536-012-0044-x

40. M. L. Cohen and J. R. Chelikowsky. Electronic Structure and Optical Properties of Semiconductors. Springer, 1988. https://link.springer.com/book/10.1007/978-3-642-97080-1

41. K.Inada, R.Takahashi, N.Naruse, T.Kadohira, S.P Cho, and T.Osaka, “Nucleation and evolution of InSb(111)B-3x3 surface”, 表面科学 第 24 巻 第 2 号 （2003). http://dx.doi.org/10.1380/jsssj.24.105

42. J. R. Chelikowsky and M. L. Cohen, “Nonlocal pseudopotential calculations for the electronic structure of eleven diamond and zinc-blende semiconductors”, Physical Review B **30**, 4828 (1984). https://doi.org/10.1103/PhysRevB.14.556

43. S. N. Sahu, J. T. Borenstein, V. A. Singh, and J. W. Corbett, “Semi-Empirical Tight Binding Calculations for the Energy Bands of the Diamond and Zincblende Type Semiconductors”, Physica Status Solidi B **122**, 661 (1984). https://doi.org/10.1002/pssb.2221220231

44. M.-Z. Huang and W. Y. Ching, “A minimal basis semi-ab initio approach to the band structures of semiconductors”, Journal of Physics Chemistry of Solids **46**, 977 (1985). https://doi.org/10.1016/0022-3697(85)90101-5

45. S. Massidda, A. Continenza, A. J. Freeman, T. M. de Pascale, F. Meloni, and M. Serra, “Structural and electronic properties of narrow-band-gap semiconductors: InP, InAs, and InSb”, Physical Review B **41**, 12079 (1990). https://doi.org/10.1103/PhysRevB.41.12079

46. Y. Liu and R. E. Allen, “Electronic structure of the semimetals Bi and Sb”, Physical Review B **52**, 1566–1577 (1995). https://doi.org/10.1103/PhysRevB.52.1566

47. D. Hsieh, D. Qian, L. Wray, Y. Xia, Y. S. Hor, R. J Cava, and M. Z Hasan, “A topological Dirac insulator in a quantum spin Hall phase”, Nature **452**, 970-974 (2008). https://doi.org/10.1038/nature06843

48. D. Hsieh, Y. Xia, L. Wray, D. Qian,1 A. Pal, J. H. Dil, J. Osterwalder, F. Meier, G. Bihlmayer, C. L. Kane, Y. S. Hor, R. J. Cava, M. Z. Hasan, “Observation of Unconventional Quantum Spin Textures in Topological Insulators”, Science **323** 919-922(2009). https://doi.org/10.1038/nature06843

49. M. H. Cohen, “Energy Bands in the Bismuth Structure. I. A Nonellipsoidal Model for Electrons in Bi”, Physical Review **121**, 387–395 (1960). https://doi.org/10.1103/PhysRev.121.387

50. P. Cucka and C. S. Barrett, “The Crystal Structure of Bi and Solid Solutions of Pb, Sn, Sb, and Te in Bi. Acta Crystallographica”, 15:865–872, 1962. https://doi.org/10.1107/S0365110X62002297

51. J. M. Ziman, “Principles of the Theory of Solids”, Cambridge University Press, 1972. https://doi.org/10.1017/CBO9781139644075

52. H. Mönig, J. Sun, M. Koroteev, G. Bihlmayer, J. Wells, E. V. Chulkov, K. Pohl, and Ph. Hofmann, “Structure of the (111) surface of bismuth: LEED analysis and first-principles calculations”, Physical Review B, 72:085410, 2005. https://doi.org/10.1103/PhysRevB.72.085410

53. C. R. Ast and H. Höchst, “Electronic structure of a bismuth bilayer,” Physical Review B, 67:113102, 2003. https://doi.org/10.1103/PhysRevB.67.113102

54. Y. Ohtsubo, J. Mauchain, J. Faure, E. Papalazarou, M. Marsi, P. Le Fèvre, F. Bertran, A. TalebIbrahimi, and L. Perfetti, “Giant Anisotropy of Spin-Orbit Splitting at the Bismuth Surface,” Physical Review B, 109:226404, 2012. https://doi.org/10.1103/PhysRevLett.109.226404

55. Yu. M. Koroteev, G. Bihlmayer, J. E. Gayone, E. V. Chulov, S. Blügel, P. M. Echenique, and Ph. Hofmann. Strong Spin-Orbit Splitting on Bi Surfaces. Physical Review Letters, 93(4):046403, 2004. https://doi.org/10.1103/PhysRevLett.93.046403

56. M. Z. Hasan and C. L. Kane, “Colloquium: Topological insulators,” Rev. Mod. Phys. 82, 3045–3067 (2010). https://doi.org/10.1103/RevModPhys.82.3045

57. T. Hirahara, K. Miyamoto, I. Matsuda, T. Kadono, A. Kimura, T. Nagao, G. Bihlmayer, E. V. Chulkov, S. Qiao, K. Shimada, H. Namatame, M. Taniguchi, and S. Hasegawa. Direct observation of spin splitting in bismuth surface states. Physical Review B, 76:153305, 2007. https://doi.org/10.1103/PhysRevB.76.153305

58. T. Hirahara. The Rashba and quantum size effects in ultrathin Bi films. Journal of Electron Spectroscopy and Related Phenomena, 201:98–104, 2014. https://doi.org/10.1016/J.ELSPEC.2014.08.004

59. T. Hirahara, K. Miyamoto, A. Kimura, Y. Niinuma, G. Bihlmayer, E. V. Chulkov, T. Nagao, I. Matsuda, S. Qiao, K. Shimada, H. Namatame, M. Tanigucho, and S. Hasegawa. Origin of the surface-state band-splitting in ultrathin Bi films: from a Rashba effect to a parity effect. New Journal of Physics, 10:083038, 2008. http://dx.doi.org/10.1088/1367-2630/10/8/083038

60. A. Takayama, T. Sato, S. Souma, T. Oguchi, and T. Takahashi. Tunable Spin Polarization in Bismuth Ultrathin Film on Si (111). Nano Letters, 12:1776–1779, 2012. https://doi.org/10.1021/nl2035018

61. A. Takayama, T. Sato, S. Souma, T. Oguchi, and T. Takahashi. One-Dimensional Edge States with Giant Spin Splitting in a Bismuth Thin Film. Physical Review Letters **114**, 066402, 2015. https://doi.org/10.1103/PhysRevLett.114.066402

62. A. Takayama, T. Sato, S. Souma, and T. Takahashi. Giant Out-of-Plane Spin Component and the Asymmetry of Spin Polarization in Surface Rashba States of Bismuth Thin Film. Physical Review Letters **106**, 166401, 2011. https://doi.org/10.1103/PhysRevLett.106.166401

63. M. Wada, S. Murakami, F. Freimuth, and G. Bihlmayer. Localized edge states in two-dimensional topological insulators: Ultrathin Bi films. Physical Review B **83**, 121310(R), 2011. https://doi.org/10.1103/PhysRevB.83.121310

64. Z. Liu, C.-X. Liu, Y.-S. Wu, W.-H. Duan, F. Liu, and J. Wu. Stable Nontrivial Z2 Topology in Ultrathin Bi (111) Films: A First-Principles Study. Physical Review Letters, **107**, 136805, 2011. https://doi.org/10.1103/PhysRevLett.107.136805

65. L. Fu and L. Kane. Topological insulators with inversion symmetry. Physical Review B, **76**, 045302 (2007). https://doi.org/10.1103/PhysRevB.76.045302

66. S. Murakami. "Quantum Spin Hall Effect and Enhanced Magnetic Response by Spin-Orbit Coupling" Physical Review Letters **97,** 236805, (2006). https://journals.aps.org/prx/abstract/10.1103/PhysRevX.2.029901

67. H. S. Inbar et a., "Inversion Symmetry Breaking in Epitaxial Ultrathin Bi (111) Films", https://arxiv.org/ftp/arxiv/papers/2302/2302.00803.pdf

Chapter 3

Experimental Background

3.1 Introduction

3.2 Experimental Method

3.3 Experimental Results

3.5 Reference

Chapter 3

Experimental background

3.1 Introduction

In this chapter, I will give the basic information about the significant parts of my experimental work, such as Ultra-High Vacuum (UHV), Molecular Beam Epitaxial (MBE), Reflection High Energy Electron Diffraction (RHEED), Core Level Photoelectron Spectra (CLPES), and Angle-Resolved Photoemission Spectroscopy (ARPES). So, the experiment was performed at the Ultra-Violet Synchrotron Orbital Radiation (UVSOR), Institute of Material Science (IMS) Japan [**1**]. This is a very suitable place and working environment with the highest brilliance of light sources and is an excellent place for synchrotron light. So, in this chapter, I will discuss all the necessary things.

3.2 Experimental Methods

For experiments of this nature, achieving an Ultra-High Vacuum (UHV) environment with a leak-free chamber is crucial. The experimentalists designed the system to attain UHV conditions within 24 to 30 hours and maintain it for a two-week experimental run. Therefore, selecting a leak-free and contamination-free environment is crucial to ensure that the heating elements achieve optimum conditions and prevent air molecules from entering the chambers during film growth. Attaining a UHV chamber is central to obtaining good results in these types of experiments. Therefore, I explored various ways to achieve a high vacuum level, including calculating impingement rate or molecular flux rates per unit area from a surface in contact with an ideal gas at a pressure P during experiments.

$$F = \frac{P}{\sqrt{2\pi m k_B T}} \qquad \textbf{3.1}$$

Here, T represents as the temperature, m is the molecular mass, and k_B is the Boltzmann constant.

The equation in **3.1** provides a calculation for the impingement rate at a pressure of 10^{-6} Pa. At room temperature (300 K), the surface will be covered by a monolayer gas molecule for almost 1 second. However, since the experimental process runs for several hours, it is crucial to maintain a contamination-free sample surface during the experiment. The pressure remaining

should be greater than 10^{-8} Pa, which is an excellent vacuum level. However, in this experiment, it is possible to reach as low as 9.5×10^{-8} Pa, which is good enough for experiments.

To achieve a high vacuum level in an ultra-high vacuum (UHV) chamber, it is crucial to minimize the impingement rate or molecular flux rate of gas molecules onto the chamber surfaces. This can be achieved through several measures:

Leak-free chamber design: To maintain a high vacuum level, it is crucial to ensure a leak-free chamber design. This can be achieved by implementing properly designed and checked seals, gaskets, and joints to minimize any gas leakage into the chamber.

High-quality vacuum components: Using high-quality vacuum pumps, valves, and fittings made from materials with low outgassing rates is essential in maintaining a high vacuum level, as discussed in the previous paragraph. These components should have low permeability to gas and be able to withstand the harsh UHV conditions without introducing contaminants.

Proper cleaning and preparation: Thoroughly cleaning and preparing the chamber surfaces before the experiment is crucial. Any contaminants on the surfaces can outgas and elevate the pressure, leading to a lower vacuum level. In-situ sputtering, solvent cleaning, and baking are effective cleaning techniques that can help achieve a clean and contamination-free environment. These techniques are commonly used in UHV systems to ensure that the surfaces to be studied are free from any unwanted contaminants that may affect the experiment's outcome. The authors employed these techniques to prepare the surfaces before their study to ensure the surfaces were clean and free from any contaminants that could interfere with their measurements.

Pumping systems: For the experiment, the authors used turbo molecular pumps, which are effective pumping systems that can achieve high pumping speeds and efficiently evacuate the chamber to maintain a high vacuum level. Additionally, ion pumps are also commonly used in UHV systems to remove gas molecules from the chamber.

Bakeout: Performing a bakeout procedure is crucial in removing any residual contaminants and improving the vacuum quality. In this experiment, the authors performed the bakeout at different temperature settings. Specifically, the sample transfer line was heated to 85℃°C, the body temperature was raised to 130℃°C, the joint temperature was almost 95 ℃°C, and the

Argon (Ar) line was heated to approximately 87 ℃°C. The bakeout process lasted for almost one day until the pressure reached approximately 9.5×10^{-8} Pa.

It is crucial to emphasize that achieving and maintaining a high level of vacuum in a chamber designed for ultrahigh vacuum (UHV) requires a meticulous approach. This involves the careful design, implementation of top-notch components, adherence to proper cleaning procedures, and employment of efficient pumping systems, all of which were thoroughly discussed in the experiment. Numerous experts in the field recommend precautionary measures such as leak-free chamber design, utilization of high-quality vacuum components, meticulous cleaning and preparation processes, and the utilization of an effective pumping system. By diligently adhering to these measures, researchers can significantly reduce the rate of impingement and effectively control the presence of gas molecules within the chamber. Consequently, this creates an ideal environment for conducting experiments involving thin films and ensures the generation of accurate and reliable results.

Molecular Beam Epitaxy (MBE)

Molecular beam epitaxy (MBE) is a technique utilized in the creation of heterostructures, which are thin layers of dissimilar semiconductor materials possessing specific electronic properties. These heterostructures are essential in the development of advanced electronic and optoelectronic devices, such as quantum wells and superlattices. MBE has proven to be highly effective in producing precise surfaces and interfaces using materials such as GaAs, InP, InAs, and InSb [**2-10**].

The MBE (Molecular Beam Epitaxy) experiment involves using various components in a chamber, such as a substrate holder, cleaning setup, evaporator, RHEED gun, and a screen in **Fig. 3.1 (a)**. The main chamber operates on the principle of epitaxial growth, where atoms are deposited on a substrate to form a film with specific electronic properties.

Substrate Selection and Preparation: The first step in substrate preparation is to carefully choose the appropriate substrate, such as InSb (111), which has a favorable lattice match with bismuth. To ensure optimal conditions, the surface undergoes a thorough cleaning process that involves sputtering and annealing. These methods effectively eliminate any impurities or contaminants before ion deposition.

Evaporator: The evaporator used in the experiment has a handmade alumina crucible where the highly purified Bi sources are loaded. To initiate the evaporation process, the evaporator is heated by passing an electric current through a tungsten filament, which causes the Bi sources to evaporate through thermionic emission.

Evaporate on Substrate: The Bi atoms in the molecular beam reach the substrate surface and undergo deposition. The substrate holder positions the substrate to receive the Bi atoms. The substrate is heated to a high temperature, typically around 180-250 ℃, which promotes adhesion and diffusion of the Bi atoms, resulting in the layer-by-layer growth of an epitaxial Bi film.

Monitoring with RHEED: During the growth process, the RHEED gun emits high-energy electrons that interact with the surface of the growing film, producing a diffraction pattern that is captured on the screen. This pattern provides real-time information about the growth of the film, including its crystal structure and quality. The connection between the RHEED system and the ARPES system, as shown in **Fig. 3.1(b)**, will be discussed in the photoemission section later.

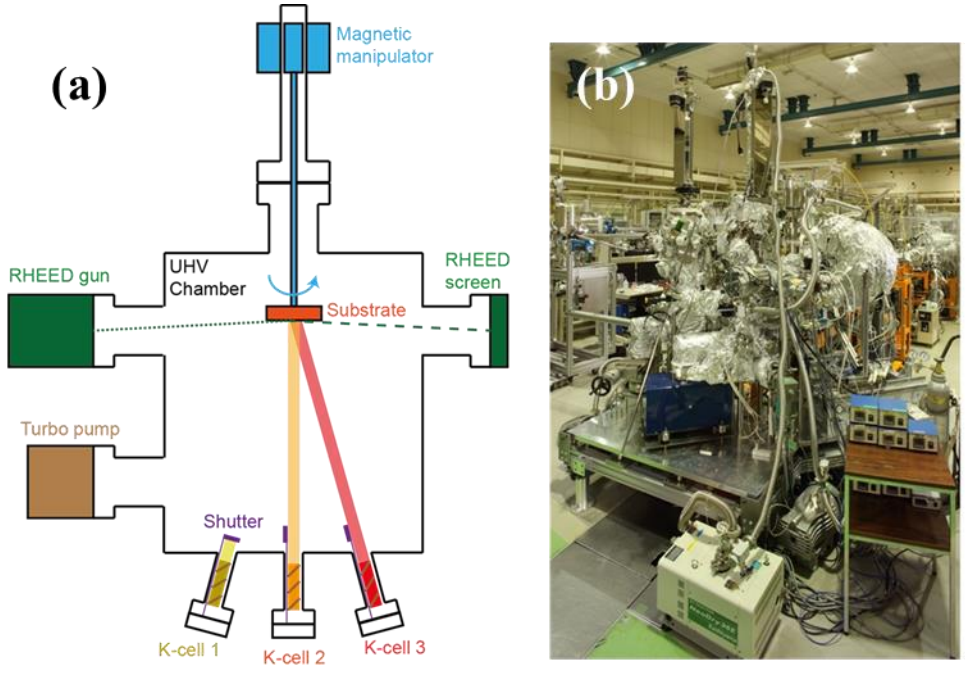

Fig. 3.1 (a) A simple sketch showing the main component of the MBE chamber. (b) Combination of MBE (Front side) and ARPES (back side).

To obtain a high-quality RHEED pattern, a pristine surface is crucial, which requires proper substrate cleaning. In my experiment, I used a repeated cycle of sputtering and annealing to

effectively clean the substrate. During this process, I maintained the annealing temperature between 250-300°C and performed 2-3 annealing cycles, each lasting 30 minutes. This series of annealing steps is of utmost importance as it involves heating the substrate, prompting the atoms on the surface to rearrange and migrate, effectively removing any remaining impurities. By employing this repeated cycle of annealing, I achieved a clean surface, which is essential for obtaining a high-quality RHEED pattern.

Conversely, the sputtering process was conducted within a vacuum chamber with a pressure of 6.4×10^{-4} Pa. Argon gas was introduced into the chamber and ionized, generating Ar+ ions. These ions were then accelerated to a voltage of 0.5 keV and directed toward the substrate, effectively sputtering off any contaminants present on its surface. This step is essential in ensuring a pristine surface for subsequent processes.

Another crucial aspect of the MBE process is the maintenance of an appropriate substrate temperature during film deposition. Typically, the growth temperature of thin films is determined through trial and error. In my experiment, I maintained the growth temperature of InSb at room temperature to prevent any undesired reactions between the Bi and InSb.

Reflection High-Energy Electron Diffraction (RHHED)

Figure. 3.2 depicts the diffraction geometry of RHEED, which is utilized to obtain real-time information about thin film samples. RHEED works on the principle that an accelerated electron gun produces an electron beam that grazes the sample surface at a glancing angle. The scattered electrons then appear on the fluorescent screen and the image is measured by a charge-coupled device to obtain the diffraction pattern **[11]**.

In reciprocal space, a sphere that forms reciprocal rods, also known as the Ewald sphere, can be imagined. Each diffraction spot on the RHEED screen originates from these rods. Due to the diffraction geometry, the diffraction spots form a series of circles on the RHEED screen known as Laue circles, as shown in **Fig. 3.2(b)**. The first circle is L_0, L_1, L_2 labeled a, followed by subsequent circles. The RHEED pattern provides information about the reconstructed lattice, lattice constant, and thickness quality of the film. A high-quality film will have bright, sharp diffraction spots against a black background indicating a well-ordered and sharp crystal

structure. Conversely, a rough surface will result in fuzzy spots with bright or white backgrounds.

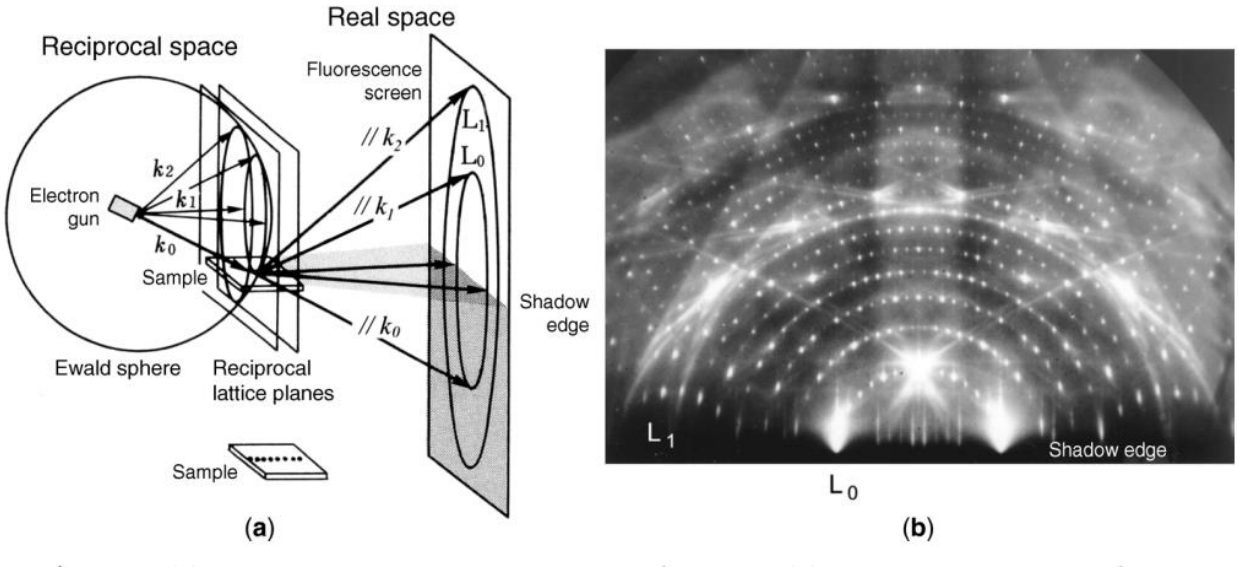

Fig. 3.2 A schematic view of the diffraction geometry of RHEED [**11**]. The RHEED pattern was taken from a Si (111)-7x7 reconstructed surface. The electron beam was 15keV in energy with [112] incidence in azimuth direction and about 3° in glancing angle θ_g to attain a surface-wave resonance condition.

RHEED oscillation provides real-time information on growth phenomena, allowing researchers to understand growth mode and thickness by observing the peaks. The growth must occur in a layer-by-layer manner with an ideal time interval between each layer (**Fig. 3.3 (a)**). By tracking the intensity of the RHEED pattern over time, the number of deposited film layers can be determined. RHEED oscillation produces maximum intensity when a complete layer has been deposited.

As films grow, the surface becomes rougher and rougher; thus, RHEED intensity reaches the minimum. As the film continues growing, the surface starts becoming smothered. As a result, the RHEED intensity increases and reaches the maximum when another film layer has been deposited. Therefore, each oscillation peak of RHEED intensity represents the growth of a bilayer film. In the case of 3D growth mode, after the first peak, the surface goes too rough, and then no peak forms (**Fig. 3.3**).

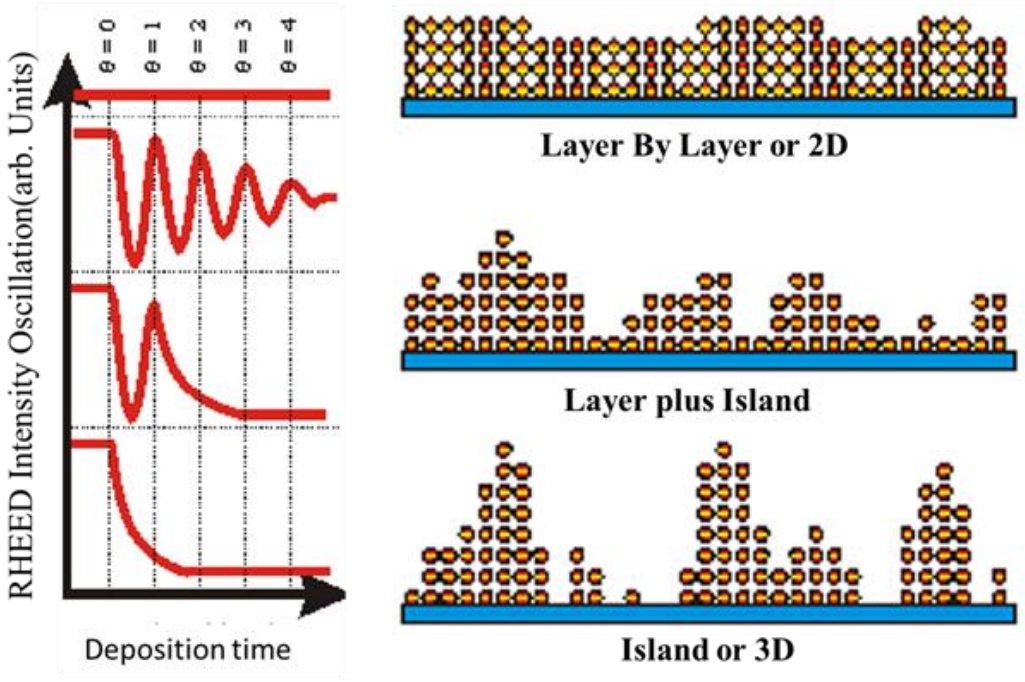

Fig. 3.3. RHEED oscillation corresponding growth phenomena, (a) an example of ideal RHEED oscillation, where each peak represents each bilayer. (b) Compared with different growth modes, the top one shows layer-by-layer mode, the middle layer plus island, and the bottom one island growth mode, respectively [**4**].

Photoelectron Spectroscopy

Photoelectron Spectroscopy (PES) utilizes high-energy photons to ionize molecules. This phenomenon was first described by Albert Einstein in 1905, for which he was awarded the Nobel Prize in 1921 [**13**]. In PES, when photons are absorbed by electrons in a sample, they can escape if their energy is higher than the sample's work function. These photoelectrons carry information about the material's binding energy and wavenumber as shown in **Fig. 3.4(a)**., which gives insights into the material's electronic and band structure.

Therefore, the electronic properties of the sample can be inferred from the recorded data by an energy analyzer shown in **Fig. 3.4(a)**. Achieving high-resolution and precise observations is highly dependent on the degree of freedom (**Fig. 3.4(b)**). The coaxial and rotational axes determine the translation and rotational degrees of freedom. The X-axis and Z-axis are perpendicular and parallel to the analyzer slit, respectively, while the Y-axis aligns with the lens axis of the analyzer. On the other hand, the polar (θ), tilt (φ), and azimuthal (ϕ) angles of rotation around the Z-axis, X-axis, and Y-axis, respectively, define the rotational axis as shown in **Fig. 3.4(b)**.

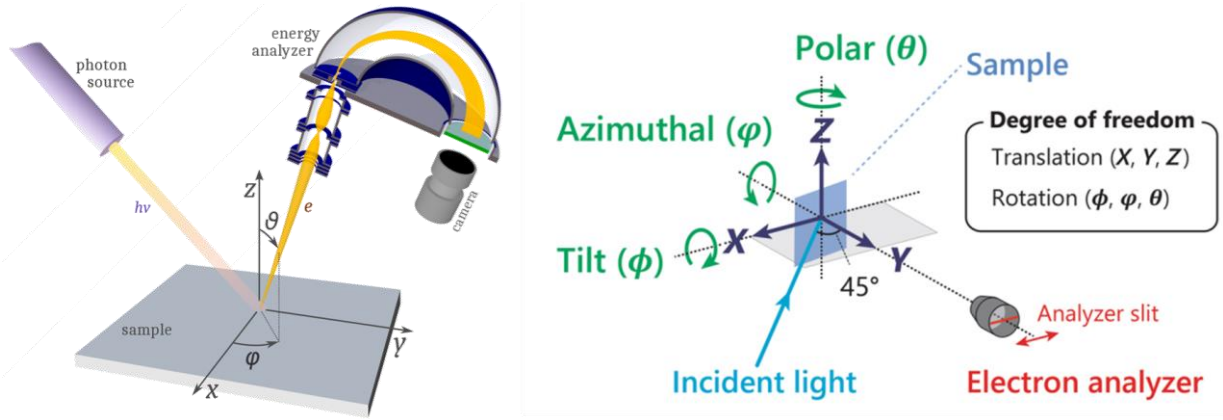

Fig. 3.4. (a) A schematic showing the angle-resolved photoemission geometry [**14**]. (b) Experimental geometry, where a goniometer manipulates the sample rotational and translational degrees of freedom [**15**].

In this study, I also examine the k-space ARPES mapping by varying the translational degrees of freedom along the X-axis to understand the band dispersion condition. Therefore, the photoemission process is a fundamental step, and a more comprehensive explanation can be found in **Fig. 3.5**. We use a 3-step model that has been widely accepted in the photoemission community [**13-15**] to comprehend the underlying physics.

1. In **Fig. 3.5(1)**, the photoemission process, we adopt a 3-step model to understand the essential physics. The optical excitation involves the exciting of an occupied electronic state (initial state) at energy E^i into an unoccupied state (final state) at energy E^f through photon absorption, $E^f - E^i = h\nu$. The energy of the exciting photon is described in a one-electron approximation via Fermi's Golden Rule formalism.

2. In **Fig. 3.5(2)**, the transport of the excited electron to the surface can be described using an effective mean free path, which is proportional to the probability that the excited electron will reach the surface without scattering. However, inelastic scatterings of electrons can give rise to a continuous background in the photoemission spectra, which is typically disregarded or subtracted.

3. In **Fig. 3.5(3)**, the escape of the photoelectron into the vacuum, after reaching the surface, gains energy, overcomes the material's work function and eventually emits from the surface. During this process, the momentum perpendicular to the surface is not conserved, and the electron is refracted at the interface between two materials, like the behavior of light following Snell's Law. However, the parallel component of the momentum remains conserved.

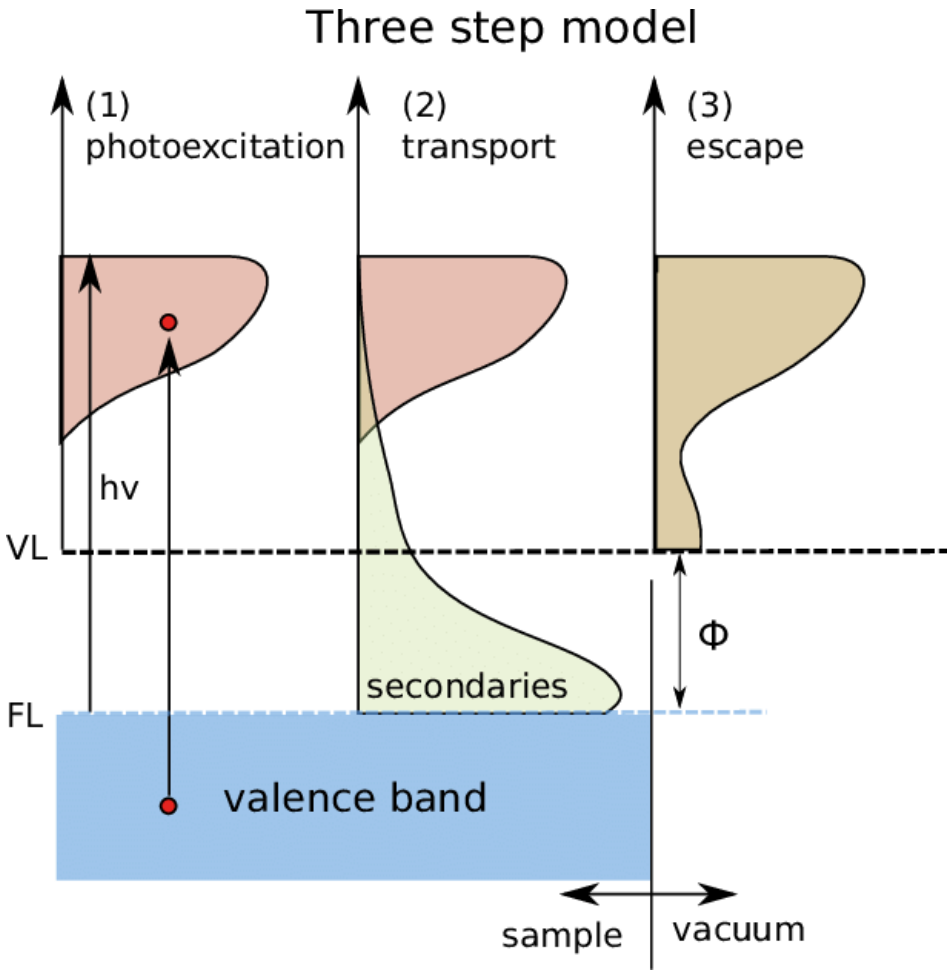

Fig. 3.5. Three-step model of photoemission process [**14**].

The key aspect here is that momentum is conserved throughout the process. This means that the total momentum before the photoemission event (photon momentum + electron momentum inside the material) must be equal to the total momentum afterward (photoelectron momentum + recoil momentum of the material).

Now, let's see how this relates to the angle of the photoelectron:

Momentum and k-vector: The momentum of an electron inside the material can be described by its k-vector, which has a magnitude (|k|) related to the electron's speed and direction. During photoemission, the momentum parallel to the surface is conserved, meaning that the parallel component of the photoelectron's momentum must be equal to the parallel component of the initial electron's momentum.

Angle and k-vector parallel component: The angle at which the photoelectron is emitted is related to the parallel component of its k-vector. Electrons emitted perpendicular to the surface have a k-vector parallel component of zero, while those emitted at grazing angles have a larger parallel component.

Therefore, by precisely measuring the angle at which the photoelectron is emitted in ARPES (Angle-Resolved Photoemission Spectroscopy) in **Fig. 3.4(a)**, one can indirectly determine the parallel component of its k-vector within the material. This important information, combined with the measured binding energy, enables us to accurately map the material's electronic band structure. This methodology provides us with a comprehensive understanding of the material's electronic structure, bonding, and properties, which in turn offers valuable insights into its behavior and potential applications.

Thickness Calculation by Theoretical Model

In this study, the calculation of thickness is crucial, and two important factors were employed for this calculation. The first factor is the analysis of RHEED (Reflection High-Energy Electron Diffraction) oscillations, as illustrated in **Fig. 3.3**, where each peak in the graph corresponds to the formation of a new layer. However, the ARPES results suggested, that after first layer formation, the missing point is the Rashba effect and Quantum Well State (QWS). The absence of these observations can be attributed to the fact that the substrate used in this study was a semiconductor material, and the Rashba effect may be still present on the material's surface, but the reason is SOC effect of Bi is not so much comparing other heavier materials, because the SOC is the heart of the Rashba effect. Moreover, the occurrence of QWS is a common phenomenon in the case of a single Bilayer (1BL), but surprisingly, this phenomenon was not observed in the first layer.

The possible reason is that:

a. **Strong bulk inversion asymmetry:** Bulk InSb inherently possesses a strong inversion asymmetry, which typically contributes to the Rashba effect at interfaces. However, in my study involving the metal/semiconductor system with less than 1BL, the interfacial potential at the interface was nearly symmetric, effectively canceling out the bulk effect.

b. **Spin-orbit coupling in Bi:** Compared to other heavier elements like Pb or TI, Bi has a less spin-orbit coupling strength. This further diminishes the Rashba effect in the Bi/InSb system down to 1BL.

To examine the concept of thickness, I will discuss the features of Quantum Well Structure (QWS) formation and its dependence on thickness. This analysis is based on the solution of the Schrodinger equation, which is a fundamental equation in the field of quantum mechanics. The equation is named after the renowned Austrian physicist, Erwin Schrodinger, and it serves to describe the behavior of matter at the atomic and subatomic levels. By establishing a relationship between the wave function of a particle and its total energy, the Schrodinger equation allows us to comprehend the diverse phenomena that occur in the microcosm.

The equation written in its most general form is time-dependent.

$$i\hbar\, \partial\psi(x,t) / \partial t \;=\; -\hbar^2/2m\, \partial^2\psi(x,t) / \partial x^2 \;+\; V(x)\, \psi(x,t) \qquad \textbf{3.2}$$

where:

i is the imaginary unit.

$\hbar$ is the reduced Planck constant

ψ (x, t) is the wave function of the particle, representing its probability distribution in space and time

m is the mass of the particle

V(x) represents the potential energy function of the system, describing the forces acting on the particle.

This equation signifies that the rate of change of the wave function over time ($i\hbar\, \partial\psi$ (x, t) / ∂t) is proportional to the sum of its kinetic energy (-$\hbar^2$/2m $\partial^2\psi$ (x, t) / ∂x^2) and potential energy (V(x) ψ (x, t)). The solution of the Schrödinger equation depends heavily on the specific potential energy function (V(x)) of the system. Different systems present different complexities, leading to diverse solution methods.

The Schrödinger equation plays a crucial role in understanding the formation of quantum well states, those discrete energy levels arising from the confinement of electrons and holes within a narrow potential well. Here's how these two concepts are interlinked:

a. Quantum Confinement:

If I consider a heterostructure, where layers of two materials with different bandgaps are stacked together as shown in **Fig. 3.6**, an interesting phenomenon occurs in the case of photoemission. One side of the heterostructure is the substrate, while the other side is a vacuum. The thickness of the deposited materials acts as a discrete quantum well in the z-direction.

In a heterostructure, the material with the narrower bandgap behaves like a potential well that can trap electrons and holes from the wider bandgap material shown in **Fig. 3.6**. When the width of this well is comparable to the de Broglie wavelength of the confined particles (usually electrons or holes), their movement becomes restricted, which is known as quantum confinement.

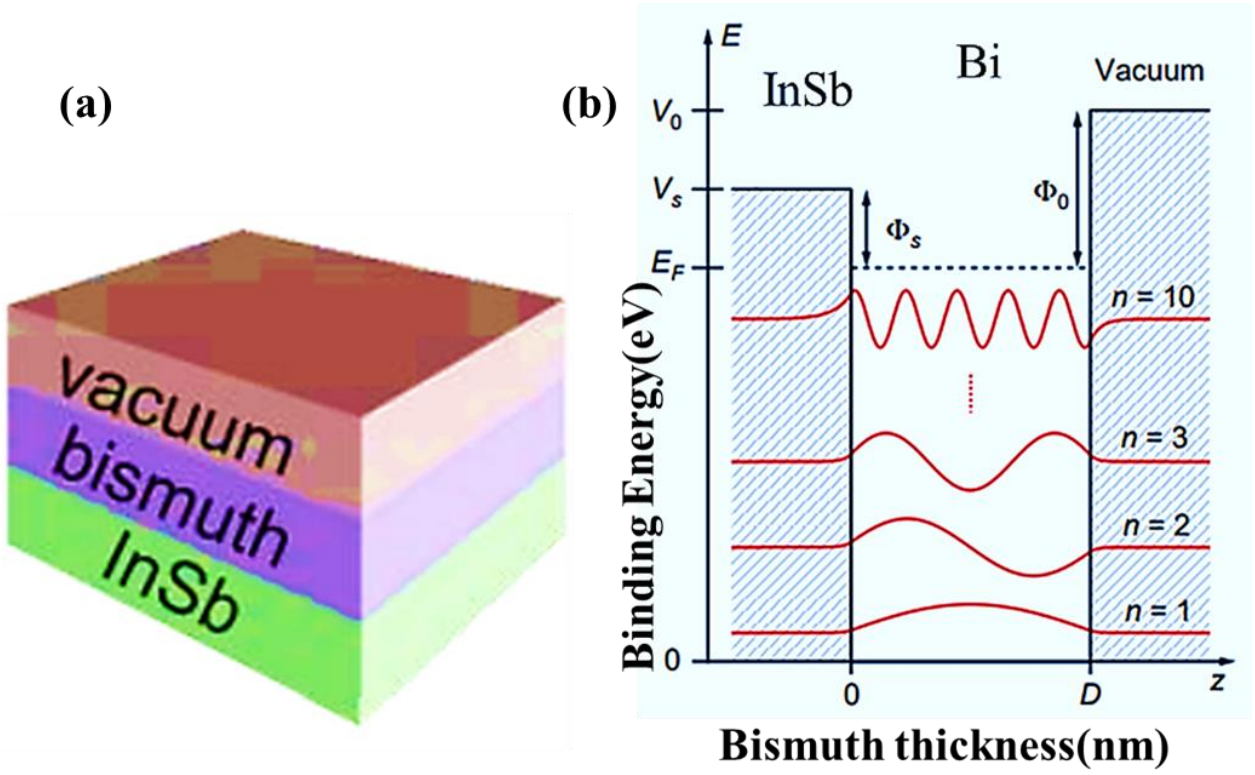

Fig. 3.6. The Quantum well state formation concept in heterostructure system, (a) My working system, (b) Quantum confinement like as the particle in a box with two potentials well.

b. Quantization of the Energy Levels:

Due to confinement, the electrons and holes can no longer move freely as they did in the bulk material. Their wave functions become quantized, meaning they can only exist in specific discrete energy states within the well shown in **Fig. 3.7**. The Schrödinger equation comes into play here. It governs the behavior of the confined particles by relating their wave function to their total energy. By solving the Schrödinger equation for the specific potential profile of the quantum well, I can determine the allowed energy levels and wave functions of the confined particles.

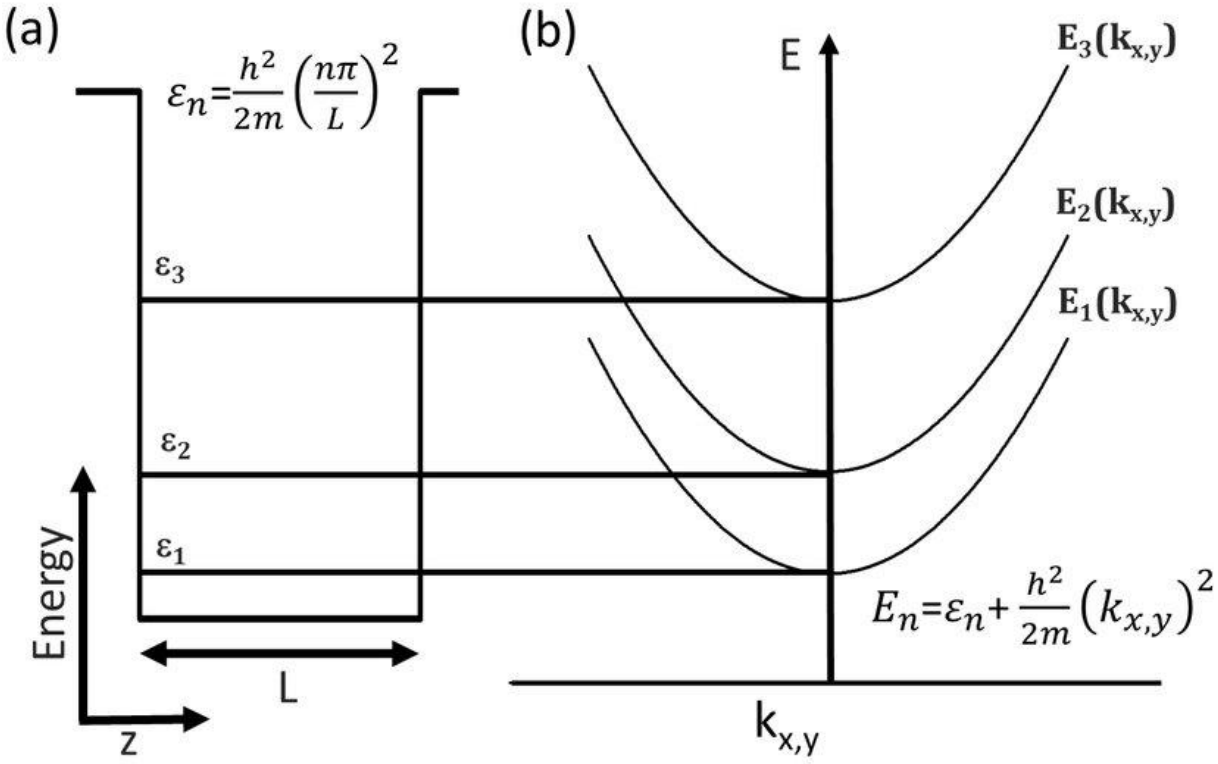

Fig. 3.7. (a) Energy levels in the conduction band of a quantum well with the confinement length L in the z-direction, (b) In-plane dispersion as a function of the wavevectors in the free x and y directions.

The Wentzel-Kramers-Brillouin (WKB) approximation is an interesting topic in quantum mechanics that provides valuable insights into the behavior of particles near surfaces. When a charged particle approaches a perfectly conducting surface, the surface induces a charge with an opposite sign, resulting in the formation of a potential wall. The potential is proportional to 1/r, where r represents the distance between the particle and the surface. It diverges as the particle gets closer to the surface and resembles the reflection of the real potential in a mirror. This potential profile plays a crucial role in various surface phenomena and quantum

mechanical effects. By employing the WKB approximation, I can derive a mathematical description of the particle's behavior near the surface and analyze its allowed energy levels and wave functions. The existence of the potential and the bound states associated with it have significant implications for phenomena such as adsorption, electron emission, and surface interactions. The phase accumulation model (PAM), derived directly from the Bohr-Sommerfeld quantization condition, provides a framework for understanding the existence of quantum-well states with a quantum number. The Bohr-Sommerfeld quantization condition states that the phase accumulated by a wave function along a closed path in phase space must be an integer multiple of Planck's constant. In the context of quantum wells, the phase accumulation model considers a particle confined within a well potential. The wave function of the particle is characterized by a quantum number n, representing the energy level or the number of nodes in the wave function. The Bohr-Sommerfeld quantization condition is applied to this confined system, stating that the phase accumulated by the wave function as it travels around the closed path corresponding to the well must be quantized.

The phase accumulation model provides a relationship between the wave vector k, which is proportional to the momentum of the particle, and the potential energy and the width of the well. By considering the phase accumulation around the edges of the well, this relationship allows for the determination of the allowed energy levels and wave functions of the quantum-well states.

$$2k_z d + \phi_{tot} = 2\pi(n-1) \qquad \textbf{3.3}$$

Where k_z is the wavevector perpendicular to the film plane, the film thickness, d, is the product of the number of BLs, N, and t is the BL thickness: $d = N * t$, t = 3.95Å. The total phase shift ϕ_{tot}, is the sum of the phase shifts at each interface: $\phi_{tot} = \phi_{Bi-vacuum} + \phi_{Bi-InSb}$.

The total phase shift, which is the sum of the phase shifts at each interface, is a crucial parameter in determining the electronic and optical properties of thin films. It can be calculated using the appropriate theoretical models based on the properties of the materials and the film structure.

In summary, the experimental procedure involves introducing the sample into a UHV chamber and monitoring the pressure to achieve optimal conditions. The sample is then subjected to baking and degassing techniques to reach a pressure of 10^{-7}10 10^{-8}Pa. The experiment consists of a repeated cycle of sputtering and annealing. Sputtering is carried out by introducing Ag+ gas to reduce the vacuum pressure to around 10^{-4}Pa, while annealing involves heating

the sample to 280 to 300°C. The evaporation process begins once a clean sample and suitable conditions for evaporating Bi on InSb (111) B-3×3 are indicated by a beautiful RHEED 3×3 pattern. To monitor the growth morphology, a real-time quartz crystal microbalance *insitu* is connected to the UHV chamber. The microbalance collects the deflected beam, also known as the RHEED oscillation peak, which represents the formation of one layer. However, it cannot confirm whether the growth layer is a monolayer or a bilayer. The evaporation rate of 1Å/min is crucial in determining the presence of a bilayer, as it takes at least 4 minutes to confirm the first bilayer formation. Further details on the growth morphology will be presented in the results section.

After completing the growth process, the next step involves conducting photoemission experiments to analyze the electronic structure. In this case, I employ the ARPES (Angle-Resolved Photoemission Spectroscopy) technique to obtain information about the electronic properties, as shown in **Fig. 3.4**. To understand the observed electronic structure and its relation to the metal-to-semiconductor transition, they use the PAM (Phase Accumulation Model) model, which is based on the WKB (Wentzel-Kramers-Brillouin) approximation. Theoretical simulations based on this model are used to support and verify the new observations and the relationship between the metal-to-semiconductor transition.

3.5 Reference

1. https://www.uvsor.ims.ac.jp/beamlines/5U/ebl5u.html
2. K. Takayanagi, Y. Tanishiro, M. Takahashi, and S. Takahashi, “Structural analysis of Si (111) -7×7 by UHV-transmission electron diffraction and microscopy”, Journal of Vacuum Science & Technology A **3**, 1502 (1985). https://doi.org/10.1116/1.573160
3. Q. Wang, W. Zhang, L. Wang, K. He, X. Ma, and Q. Xue, “Large-scale uniform bilayer graphene prepared by vacuum graphitization of 6H-SiC (0001) substrates”, Journal of Physics: Condensed Matter 25, 95002 (2013). http://dx.doi.org/10.1088/0953-8984/25/9/095002
4. R. F. C. Farrow, D. S. Robertson, G. M. Williams, A. G. Cullis, G. R. Jones, I. M. Young, and P. N. J. Dennis, “The growth of metastable, heteroepitaxial films of α-Sn by metal beam epitaxy”, Journal o. Crystal Growth 54, 507-518 (1981). https://doi.org/10.1016/0022-0248(81)90506-6

5. I.Hernández-Calderón, and H.Höchst, "Angle-resolved photoemission of α-Sn(111) and the polar (111) and (111) surfaces of InSb", Surface Science, 152–153, 2, 1035–1041(1985). https://doi.org/10.1016/0039-6028(85)90518-7
6. T. Nakada, and T. Osaka, "Sb trimer structure of the InSb(111)B-(2 × 2) surface as determined by transmission electron diffraction", Physical Review Letters 67, 2834–2837(1991). https://doi.org/10.1103/PhysRevLett.67.2834
7. J. Wever, H.L. Meyerheim, W. Moritz, V. Jahns, D. Wolf, H. Schulz, L. Seehofer, R.L. Johnson, "A new type of reconstruction on the InSb($\overline{111}$) surface determined by grazing incidence x-ray diffraction", Surface Science 321, L225–L232(1994). https://doi.org/10.1016/0039-6028%2894%2990179-1
8. T. Hirahara, G.Bihlmayer, Y.Sakamoto, M.Yamada, H.Miyazaki, S.Kimura, S.Blugel, and S.Hasegawa, "Interfacing 2D and 3D Topological Insulators: Bi (111) Bilayer on Bi_2Te_3", Physical Review Letters **107**, 166801(2011). https://doi.org/10.1103/PhysRevLett.107.166801
9. C. McGinley, A. A Cafolla, B. Murphy, D. Teehan, P. Moriarty, "The interaction of bismuth with the GaAs (111) B surface", Applied Surface Science **152**, 169(1999). https://doi.org/10.1016/S0169-4332(99)00311-6
10. L. Nicolaï, J.M. Mariot, U. Djukic, W. Wang, O. Heckmann, M. C. Richter, J. Kanski, M. Leandersson, T. Balasubramanian, J. Sadowski, J. Braun, H. Ebert, I. Vobornik, J. Fujii, J. Minár and K. Hricovini, "Bi ultra-thin crystalline films on InAs(1 1 1)A and B substrates: a combined core-level and valence-band angle-resolved and dichroic photoemission study", New Journal of Physics **21**, 123012(2019). http://dx.doi.org/10.1088/1367-2630/ab5c14
11. S. Hasegawa, "REFLECTION HIGH-ENERGY ELECTRON DIFFRACTION (RHEED)", Characterization of Materials, 2012. http://www-surface.phys.s.u-tokyo.ac.jp/papers/2012/CharacteriMat(Hasegawa)201202.pdf
12. C. Liu, Y. Zhou, G. Wang, Y. Yin, C. Li, H. Huang, D. Guan, Y. Li, S. Wang, H. Zheng, C. Liu, Y. Han, J. W. Evans, F. Liu, and J. Jia, "Sierpiński Structure and Electronic Topology in Bi Thin Films on InSb(111)B Surfaces", Physical Review Letter **126**, 176102 (2021). https://dx.doi.org/10.1103/PhysRevLett.126.176102
13. Ph. Hofmann "The surfaces of bismuth: Structural and electronic properties", Surface Science **81**, 191–245 (2006). https://doi.org/10.1016/j.progsurf.2006.03.001

14. A. Einstein, “Uber einen die Erzeugung und Verwandlung des Lichtes betreffenden heuristischen Gesichtspunkt”, *Ann. Phys.* **17** 132– 48 (2005). https://doi.org/10.1002/andp.19053220607
15. https://en.wikipedia.org/wiki/Angle-resolved_photoemission_spectroscopy
16. H. Iwasawa, H. Takita, K. Goto, W. Mansuer, T. Miyashita, E. F. Schwier, A. Ino, K. Shimada, and Y. Aiura, “Accurate and efficient data acquisition methods for high-resolution angle-resolved photoemission microscopy”, Scientific Reports, **8,** 17431 (2018). https://doi.org/10.1038/s41598-018-34894-7

Chapter 4

Theoretical Calculation

4.1 Introduction

4.2 InSb Bands Structure Formation

4.3 Bismuth BL Formation

4.4 Reference

Chapter 4

Theoretical Calculation

4.1 Introduction

Density Functional Theory (DFT) calculations have become a powerful tool for understanding the electronic structure and properties of materials at the quantum level and for comparison with experimental results. Quantum Espresso is a widely used software package that performs DFT calculations and simulates the behavior of various materials [1]. In this study, I utilized Quantum Espresso to investigate the structural and electronic changes of Bismuth and Indium Antimonide (InSb), a metal and semiconductor compound. Specifically, I explored the transformation of its cubic structure to a hexagonal one and its impact on the crystal lattice's heavy hole and light hole effects, which were reflected in the experimentally obtained results [2-5]. These effects are particularly noticeable in the $\overline{\Gamma K}$ direction and less prominent in the $\overline{\Gamma M}$ direction.

InSb is well-known for its unique properties, including a narrow direct bandgap that is ideal for various optoelectronic applications. It is crucial to comprehend the changes in its electronic structure due to structural transformation to tailor its properties to meet specific device requirements. Additionally, I examined the impact of Spin-Orbit Coupling (SOC), which introduces relativistic effects into my calculations, and compared it to calculations performed without SOC. SOC can significantly influence the electronic structure of materials, especially those containing heavy elements, and its presence or absence in this study will shed light on how it affects the heavy-hole and light-hole effects observed.

In this chapter, I will try to provide a comprehensive analysis of the structural and electronic transformations in InSb as it transitions from a cubic to a hexagonal structure, focusing on the pronounced differences in the $\overline{\Gamma K}$ and $\overline{\Gamma M}$ directions. I will also assess the role of SOC in these changes, ultimately contributing to a deeper understanding of the materials science behind this fascinating semiconductor compound. After that, I introduce the Bi (111) on the slab and compare it with experimentally obtained results. If anyone is interested in replicating this study, they should refer to my previous research, including my M.Sc. thesis paper, which contains the

Quantum espresso code and other relevant work [6-12]. Moreover, a working knowledge of Quantum Espresso, Linux, and Python is necessary.

4.2 Formation of InSb band Structure

The formation of the InSb band structure is a complex interplay between its atomic arrangement and the quantum mechanical properties of its electrons within its crystal lattice. To understand the origin of the band structure, it is necessary to examine the theoretical model where bands can be approximated as parabolic in k-space. The energy of a carrier in the band E(k) = $\hbar^2k^2/_{2m^*}$ is related to an effective mass m*. A simple model includes a single parabolic conduction band and a single parabolic valence band. A more detailed model may include more bands and the nonparabolicity of those bands. For instance, the Kane model comprises four nonparabolic bands, which include one conduction band and three valence bands, as given by [2].

$$\text{Conduction band } E_c = E_g + \frac{\hbar^2k^2}{2m} + \frac{P^2k^2}{3}\left(\frac{2}{E_g} + \frac{1}{E_g+\Delta}\right),$$

$$\text{Heave-hole band } E_{v1} = \frac{\hbar^2k^2}{2m},$$

$$\text{Light-hole band } E_{v2} = \frac{\hbar^2k^2}{2m} - \frac{2P^2k^2}{3E_g},$$

$$\text{and split-off band } E_c = -\Delta + \frac{\hbar^2k^2}{2m} - \frac{P^2k^2}{3(E_g+\Delta)},$$

All of which can be approximated by parabolic bands of different effective masses. The band structure of InSb is shown in **Fig. 4.1**. To find out the origin of the obtained band structure, I reproduced the same structure with quantum espresso. Quantum Espresso is a computational software package that can be used to calculate the electronic structure of materials using density functional theory (DFT), and the calculations depend on several factors, including the choice of pseudopotentials, exchange-correlation functional, and k-point grid as well as the SOC and no SOC effect with the DFT+U correction.

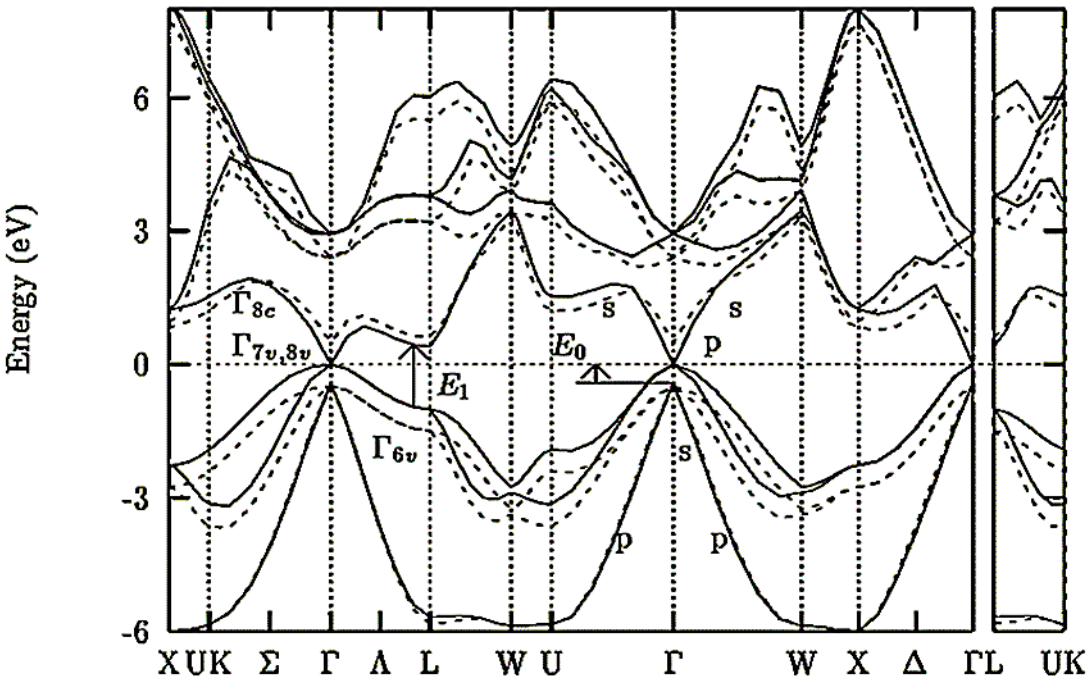

Fig. 4.1. Band structure of InSb showing 4 Kane model bands with the effect of SOC (solid line) and no SOC (dashed line) **[3]**.

To maintain consistency with previous research, I used the cubic structure with space group 216 (F-43m) for DFT calculations. This choice was made because of the high symmetry of the structure and the simplified analysis of electronic band structures. The atoms were positioned at the origin (0, 0, 0), with Sb atoms set at (0.25, 0.25, 0.25) **(Fig. 4.2(a))**. I used ultrasoft pseudopotential (USPP) and Perdew-Burke-Ernzerhof (PBE) exchange-correlation functions in dense k points. To reflect the cubic structure and compare it with reference results, I used ibrav=2 to touch all the symmetry points shown in **Fig. 4.2 (b)**.

Let us now compare the band structures shown in **Fig.4.1 and Fig. 4.2(c)**. In non-relativistic calculation results in a zero-gap at the Γ point, and other bands almost remain the same consistent with previous results obtained with SOC. It is worth noting that recent pseudopotentials include the d orbital effect, whereas older results only affected the s and p bands. The total calculation is based on two functions, and other parameters remain the same, with the relativistic effect being the differentiating scalar-relativistic calculation (SRC), where I used a cutoff wavefunction of 27 Ry and cutoff charge density of 180 Ry to obtain accurate results. These results remained almost the same in full relativistic calculations (FRC). However, the valence band configuration and core band configuration provide the changing factors in the FRC.

In the next section, I will present detailed results on this point. Upon performing FRC, which considers SOC effects shown in **Fig. 4.2 (d)**, I observed that the heavy hole (HH) and light hole (LH) degenerate into one band and this degenerated effect is visible after applying SOC, which is consistent with recently published ARPES results [**12**]. This could explain why previous ARPES studies did not observe a distinguished band between the HH and LH as reported in [**13-14**].

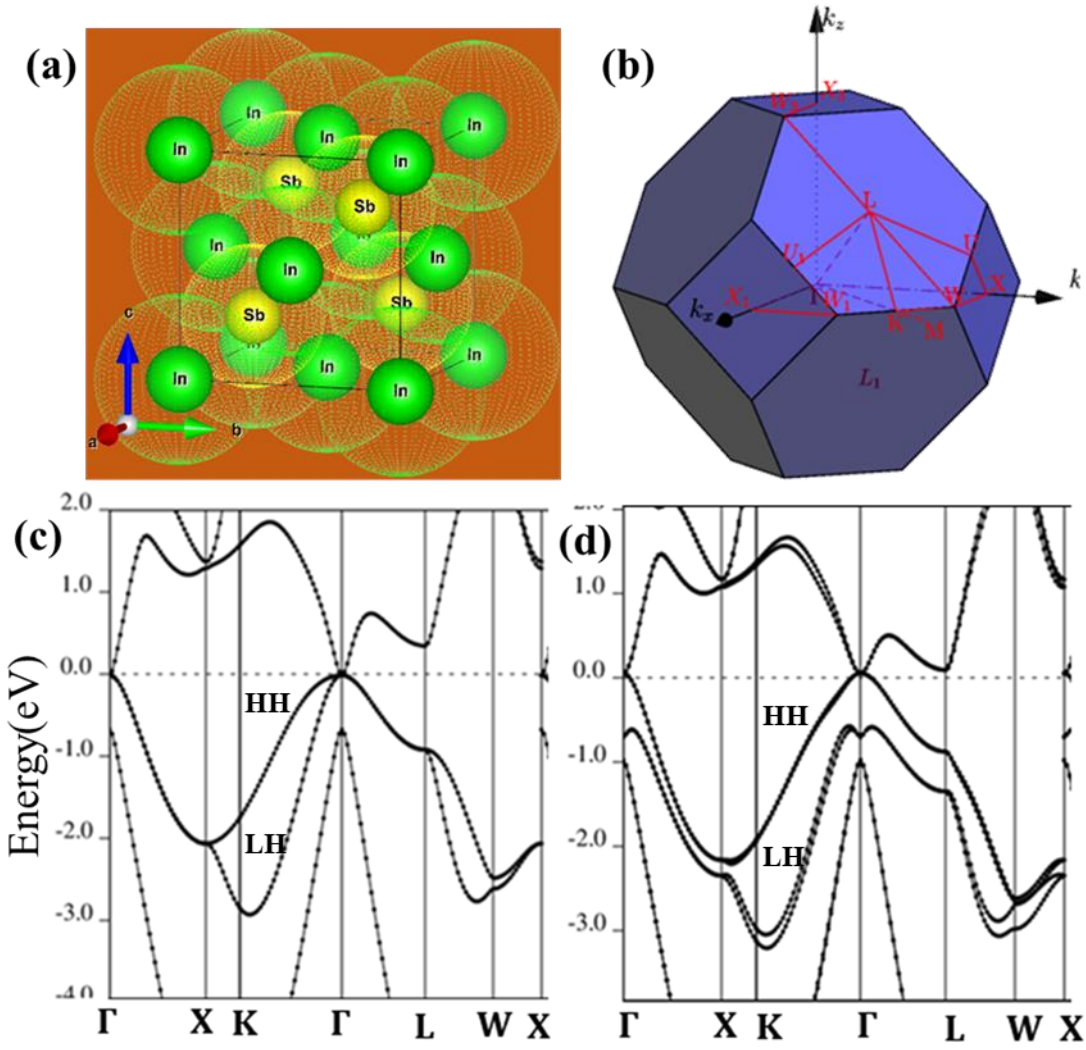

Fig. 4.2. InSb band structure by quantum espresso, (a) atomic configuration for cubic lattice, (b) Brillouin zone for ibrav=2, all the symmetry point check in this configuration, (c) using be pseudo without relativistic effect, (d) with relativistic effects, where atomic position chosen as cubic 0.00 and 0.25, and lattice constant is taken as in-plane value 4.58Å.

The effects of relativistic calculations with shape modification to a hexagonal structure were investigated in this study.

SRC and FRC differ based on the pseudopotential (PP). SRC checks each of the one-orbital

effects, while FRC includes the effect of multiple orbitals, denoted as spin-orbit coupling (SOC).

In this study, I employed pseudopotential files such as, In.pbe-dn-rrkjus_psl.1.0.0.UPF and Sb.pbe-n-rrkjus_psl.1.0.0UPF for SRC. These files represent the pseudopotential for Indium (In) and Antimony (Sb) using the Perdew-Burke-Ernzerhof (PBE) exchange-correlation functional for quantum espresso DFT calculations, and the "dn-rrkjus_psl" designation indicates that spin-orbit coupling (dn) and scalar-relativistic effects (rrkjus) are included.

The specific version number "1.0.0" indicates the version of the pseudopotential file, which is periodically updated to improve accuracy and include more refined calculations. For full relativistic calculations (FRC), I used In.rel-pbe-dn-rrkjus_psl.1.0.0.UPF and Sb.rel-pbe-n-rrkjus_psl.1.0.0UPF, which consider two s, three p, and d orbital effects in the valence configuration. In the case of SRC, only one s and p effect are considered.

Now, if I compare the previously established band structure with my calculations, it may be comparable, as shown in **Fig. 4.2.** and **Fig. 4.3**. If I go from the Γ high symmetry line to the K direction, one can easily show the so-called heavy hole and light hole mostly visible in ΓK direction; other directions are not visible. Because the heavy hole and light hole bands are a result of the crystal symmetry and the presence of spin-orbit coupling (SOC) in the material. In the absence of SOC, the bands would cross with each other at certain high symmetry points in the Brillouin zone. However, when SOC is included, the bands become split due to the spin-orbit interaction, resulting in distinct heavy-hole and light-hole bands. The observation that the heavy hole and light hole bands are more clearly visible in the $\overline{\Gamma K}$ direction suggests that this is a preferred direction for their dispersion. In other directions, the bands may overlap or exhibit folding effects, making it difficult to clearly distinguish between heavy hole and light hole states.

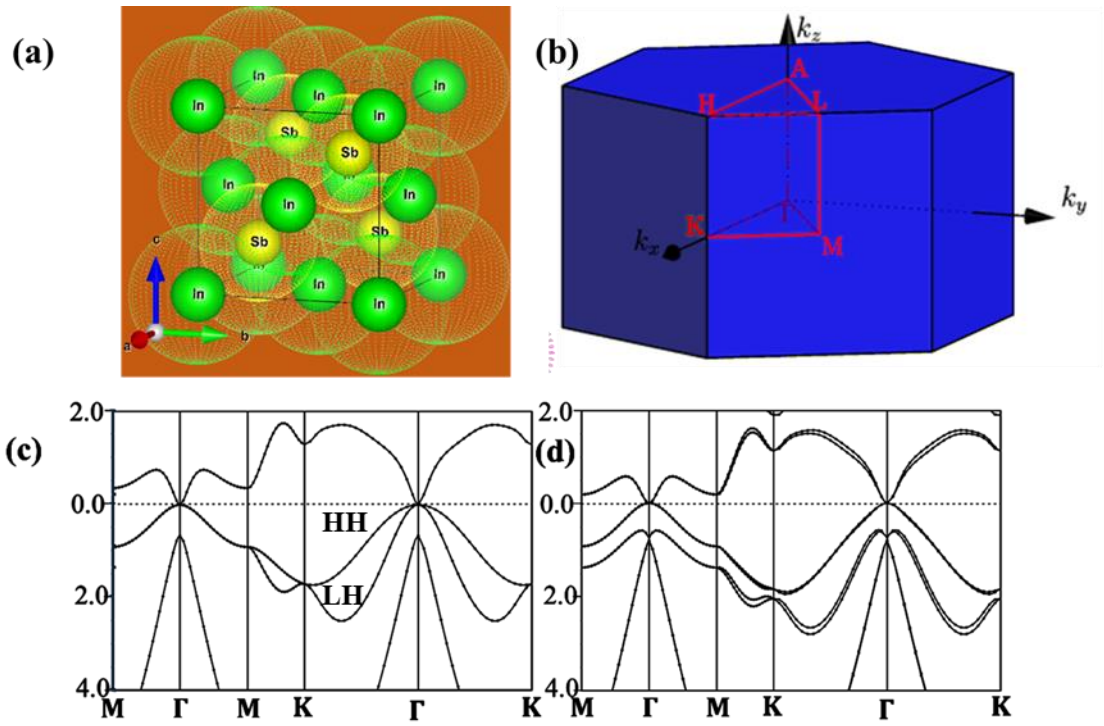

Fig.4.3. (a)The crystal structure of the cubic InSb, (b) Corresponding Brillouin zone boundary for suggesting hexagonal shape case by quantum espresso, and (c and d) cubic structure shape modified as hexagonal calculating band structure of this 1DL freestanding InSb(111) case, where (c) scalar relativistic (SR) case means no spin-orbit coupling (SOC) effect included, (d) full relativists (FR) case means included spin-orbit coupling (SOC).

Furthermore, the analysis and interpretation of the band structure becomes more intricate with the introduction of fine relativistic corrections (FRC). FRC accounts for more elaborate relativistic effects beyond the fundamental SOC, which can influence the band gap and alter the band dispersion. This can pose a challenge to determine the precise features of the heavy hole and light hole bands, especially when using experimental methods such as angle-resolved photoemission spectroscopy (ARPES).

The reference to ARPES results based on InSb suggests that experimental findings are supporting the presence of folding effects that hinder clear distinction between the heavy hole and light hole states, even when SOC is included [5]. ARPES is a powerful technique for studying the electronic band structure and can provide valuable insights into the behavior of charge carriers in materials like InSb. This is clearly shown in Fig. 4.3(d), where after SOC, the heavy hole, remains on the same position band, and the light hole shifts downwards, exhibiting little Rashba splitting of the bands [4].

However, it is worth noting that in experimental studies, substrates are typically cleaned in the [111] direction due to the hexagonal shape of InSb. Additionally, the ibrav=4 parameter in Quantum ESPRESSO, which denotes hexagonal symmetry for 2D growth, remains comparable to the experimental findings. This parameter is specified in the input file to determine the lattice vectors of the simulation cell.

The parameter ibrav=4 in QE denotes a hexagonal crystal structure with the simulation cell described by two lattice vectors in the x-y plane and a different lattice vector in the z-direction. The angles between these lattice vectors are 90 degrees, but the lengths of the lattice vectors in the x-y plane can vary.

When using ibrav=4, I need to provide additional input values such as celldm(1) (the length of the lattice vector in the x-y plane), celldm(3) (the length of the lattice vector in the z-direction). Where celldm is a set of parameters used to define the lattice vectors and scale the simulation cell. It stands for "cell dimension" and is an array of values defined in the input file. The celldm parameters depend on the chosen value of ibrav, which represents the crystal structure. Different values of ibrav require different sets of celldm parameters. For example, if ibrav=4 (hexagonal crystal structure), celldm consists of two values: celldm(1) for the length of the lattice vector in the x-y plane and celldm(3) for the length of the lattice vector in the z-direction.

celldm(1) represents the scaling factor for the lattice vector in the x-y plane.
celldm(2) is not used for ibrav=4.
celldm(3) represents the scaling factor for the lattice vector in the z-direction.
celldm(4) represents the ratio between the lengths of the lattice vectors in the x-y plane.

The specific values for celldm depend on the chosen crystal structure and can be calculated or obtained through experiments. Modifying the celldm parameters enables the adjustment of the simulation cell’s size and shape, which affects the system’s properties and behavior being simulated in Quantum ESPRESSO.

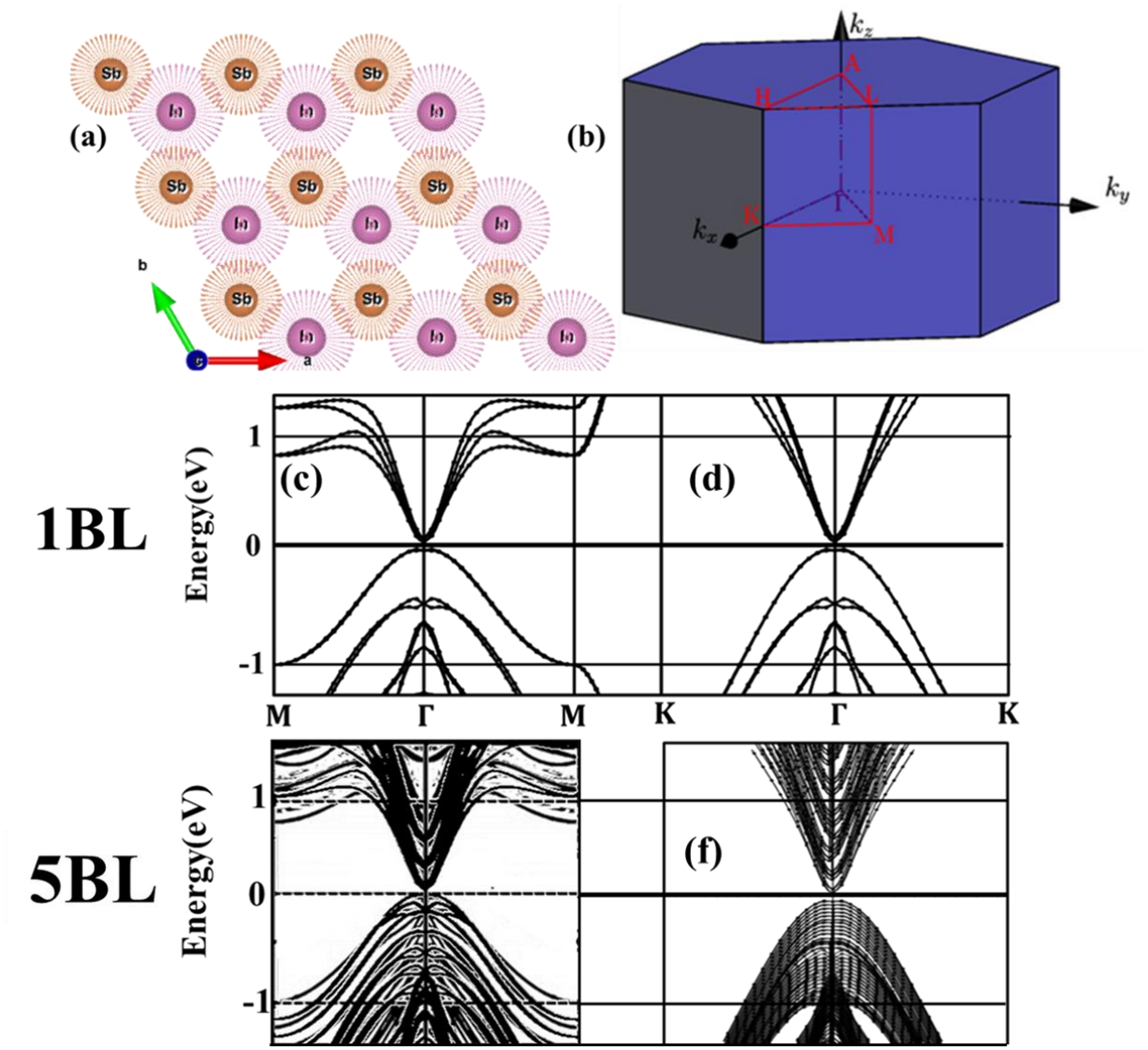

Fig.4.4. The slab bilayer formation as hexagonal shape of InSb (111) direction, (b) Calculating BZ, as irabv =4, corresponding band structure $\overline{\Gamma M}$ and $\overline{\Gamma K}$ direction, (c) 1BL (means 4 atoms, thickness almost 2Å), (d) 5BL (~10Å).

In this case, the atomic positions of In and Sb are considered as 0.00 and 0.25, respectively, and the symmetric position is $\overline{\Gamma M}$ and $\overline{\Gamma K}$ direction chosen for this work. The study also suggests that while the heavy hole and light hole effects can be observed in the $\overline{\Gamma K}$ direction of SRC calculations, they are not easily discernible in FRC calculations.

After examining the results, I decided to use a hexagonal slab calculation shape with the atomic positions of in and sb set at 0.00 and 0.25, respectively, and the symmetric position chosen for the <111> direction. The thickness of 1BL is almost 3.9Å, and the thickness of the other BLs changes with the z-direction and celldm(3), representing the cell dimension in quantum

ESPRESSO, as shown in the corresponding Brillouin zone in Fig. 4.4(b). Before SOC, the heavy hole and light hole could be identified in the $\overline{\Gamma K}$ in [111] direction, but after FRC, a small shift down and a fold at 0.5 eV occurred in both directions, as shown in Fig. 4.3(d). Therefore, as the shape changed from cubic to hexagonal in InSb (111) in Fig. 4.4(a), it became more apparent in Fig. 4.4(c). By increasing the thickness size by a factor of the z-direction and celldm, after 10BL, a thick slab was formed with no band gap like 1BL and visible inversion symmetry.

4.3 Bi BL Formation

To understand the formation of Bi (111) bilayer, I compared it with the recent results of Koroteev et al. (2008) [15] (Fig. 4.6(b and e)) and Inbar et al. (2023) [**17**] (Fig. 4.9). While one is based on free-standing and the other on substrate influence of Bi (111), I compared band structures with SOC and without SOC, where the 1BL case is almost comparable with the past results. However, the platform used in the previous studies was different; they used the FLEUR code [**16**], while I used quantum espresso, which is also an open-source tool for DFT calculation. In comparison led to the determination of the ideal lattice constant in-plane Bi (111) case and the c/a ratio of 3.08 Å optimized the structure, which suggests the same as the Bi (111) band structure. Although atomic position has little effect on band structure, the thickness of the band structure remains between 2.92 Å to 3.16 Å for 1BL, as shown in Fig.4.5(a), where the atomic position distance between 1ML and 2nd ML is almost 3Å. In the case of 2BL, where no SOC reflects the same as the Koroteev results, but after including SOC, it gives the Reasba-like non-degenerating band, which may be due to the DFT+U correction, as the latest full relativistic pseudo included the d orbital effects. As many papers suggested, the Rashba splitting band remains, which originated due to SOC.

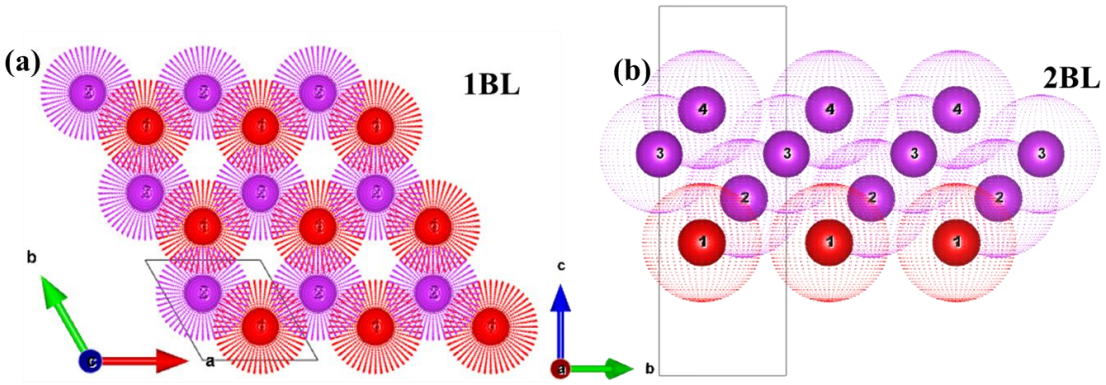

Fig.4.5. Bi formation is like a honeycomb structure, **(a)** 1BL case, two atoms in the unit cell, 3 atoms in 1ML, and other ML has another 3 atoms. **(b)** 2BL case and other 2ML cases like the ABCABC case.

Therefore, I compared experimental data with the theoretical calculations on free-standing Bi thin films by Koroteev et al. [15] to confirm the theoretical prediction of a free-standing band in ultrathin case Bi (111), as shown in **Fig. 4.6**. However, these findings differ slightly from theirs due to the influence of the substrate. This was evidenced by the clear peak shift observed in ARPES measurements of the Bi/InSb system, as suggested by CLPES.

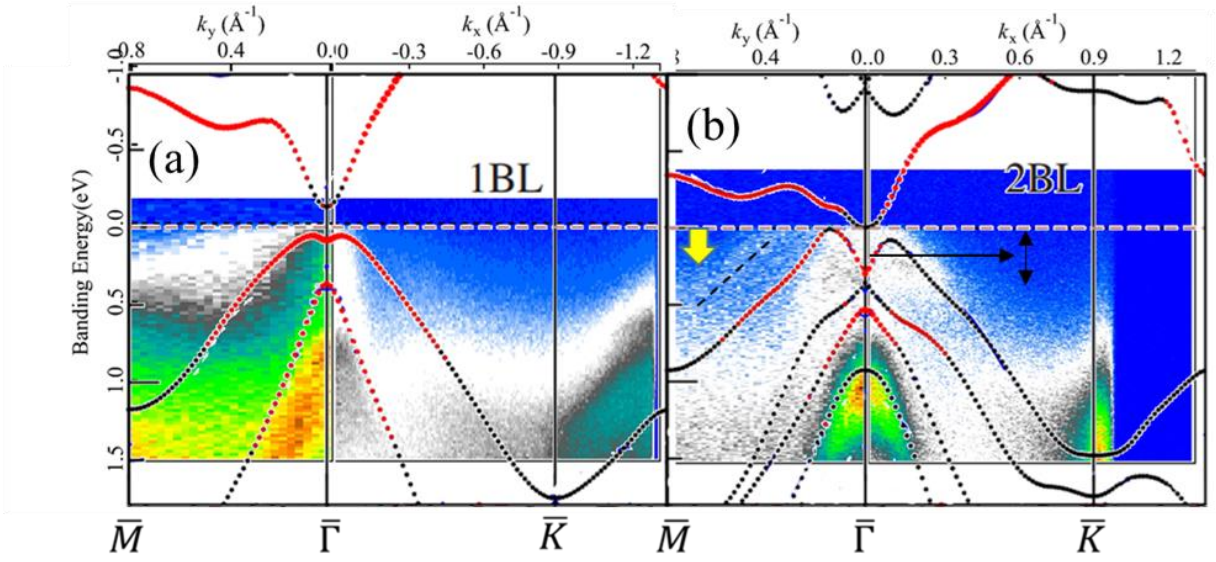

Fig. 4.6. My experimental ARPES band dispersion is superimposed with free-standing calculations by Koroteev et al. [15], (a) less than 1BL, (b) less than 2BL Bi (111)/InSb (111) B-3x3, dashed line indicated by the yellow pointer is QWS.

However, Koroteev's prediction suggests a slightly comparable band structure with SS. The obtained QWS in ultrathin Bi (111) BL is almost shifted up 0.5eV in **Fig. 4.6(b),** indicated by a dashed line with a yellow pointer, which is observed at nominally down to 2BL and after introducing substrate influence band dispersion suggested possible QWS formation starting from the 1BL case. Therefore, this comparison, shows that there are differences between the free-standing and substrate-influenced Bi band structures. Thus, I started my investigation from the 1BL case. According to DFT, Bi p states split into bonding and anti-bonding states, forming a gap between the lower and upper Fermi levels [**Fig. 4.7 (b)**]. However, in the experiment, it is difficult to observe because the states above the Fermi level cannot be observed due to an unoccupied state as the ARPES limitations in **Fig. 4.6**.

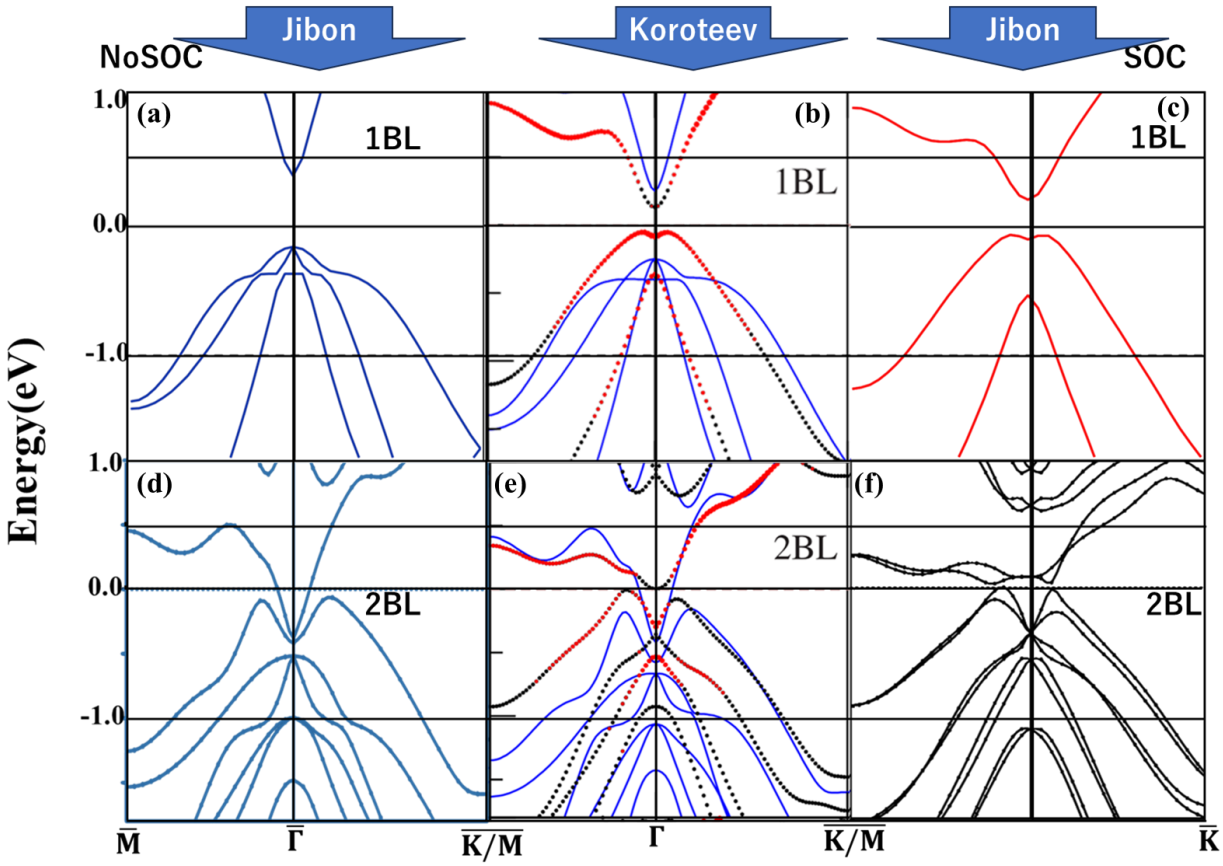

Fig. 4.7. Free-standing Bi (111) formation compared with the Koroteev et al. results, where the top row shows the 1BL (**a, b, c**) and the bottom row 2BL (**d, e, f**) case, and the left side (**a, d**) is scalar relativistic calculation (SRC) means without SOC, and the right side (**c, f**) free-standing full relativistic calculation (FRC) means with SOC. The middle section at the top (**b**) 1BL and the bottom (**e**) 2BL is comparable to Koroteev et al. results (2008) [**15**], where a thin blue line is calculated without including SOC and a red/black line after including SOC.

Below the Fermi energy, the theoretically predicted QWS states in the 1BL case are a little difficult to observe due to the substrate effect and SOC effect in Bi (111). These no SOC and SOC clearly give an ideal prediction of the 1BL case, but the 2BL with SOC little different phenomena shown, and the 1BL no SOC was almost the same; it may reason for the DFT+U correction because the latest full relativistic pseudo potential formation such a way included the d orbital effects although near fermi energy d has no effects. As many papers suggested, the Rashba splitting band remains, which originated due to SOC. Therefore, to find my exact experimental results, I compare them with the other results, that is Inbar et al. [**17**] in **Fig. 4.8**.

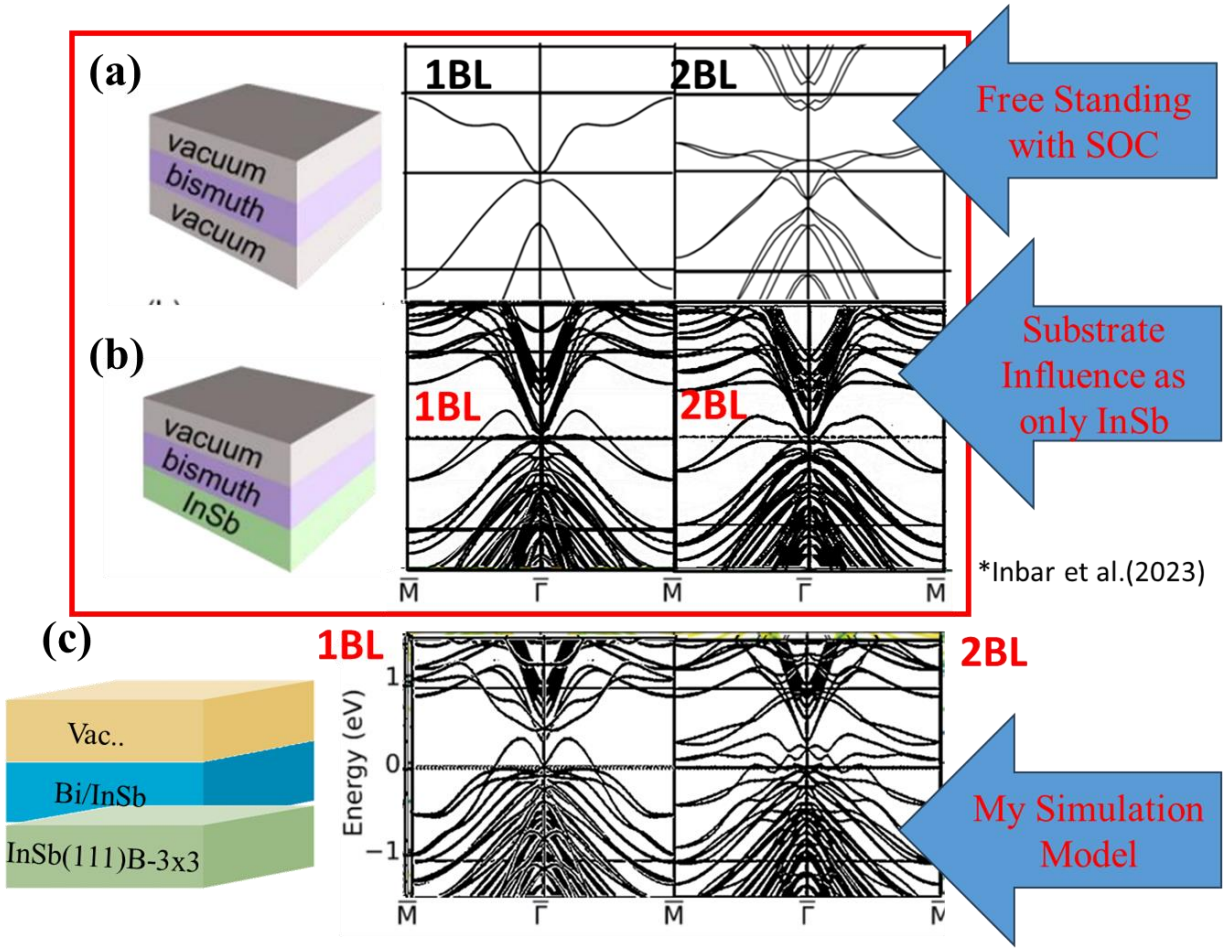

Fig. 4.8. Comparative DFT calculation between Inbar et al. [17] by VASP and mine by quantum espresso, were simulated. is reproduces results from Inbar et al. [17] and (c) in my simulation model.

After a comparative model. their results and my results suggest that the broken inversion symmetry remains at the $\bar{M}$ point, and the observed electron pocket is the signature of broken inversion symmetry. However, the higher BL shows trivial surface state crossing. To reproduce their results, I created a Bi (111) supercell on 10BL slab InSb, which almost reflects the findings of Inbar et al. [17]. My experiment does not exactly follow these results, so I adjusted some parameters by considering the 1BL slab and creating a supercell on this slab, where the lattice constant taken in between Bi and InSb, i.e. 4.56Å, and atomic position is considered as a hexagonal shape. However, the 2BL case almost reflects Inbar et al. [17] results, and the 1BL case shows slightly little different phenomena, compared to my experimental results.

To investigate new states down to 2BL cases, I deposited Bi (111) on InSb (111) B reconstructions, and checked the RHEED pattern for crystal quality, as explained in the previous chapter. The number of BL was determined by RHEED oscillation and found 3

distinguishable peaks shown in the next chapter, indicating that 3BL formation is possible depending on the substrate and experimental conditions. After that, I measured ARPES, which provided the band dispersion, and the new state located in this band dispersion is suggested. As successful formation of the 2BL band dispersion was due to thickness-dependent QWS at nearly 0.4 eV, whereas Inbar et al. observed it at 2.6BL at 0.3eV. In this point of view, my results support the new state formation as QWS at less than 2.6BL i.e., I found QWS down to 2BL shown in **Fig. 4.6(b)**, and the distinguishable features between 1BL and 2BL Fermi surface will be explained in more detail in the results sections.

4.5 Reference

1. https://www.quantum-espresso.org/Doc/user_guide_PDF/user_guide.pdf
2. Evan O. Kane, "Band Structure of Indium Antimonide", Journal of Physical Chemistry in Solids Vol.1, pg. 249-261 (1957). https://doi.org/10.1016/0022-3697(57)90013-6
3. Vladislav Dubikovskiy, "Optical Limiting: Numerical Modeling and Experiment", University of Central Florida Ph.D. Dissertation, Ch.4 pg.96 (2003).
4. Yang, S., M. Schröter, N. B., Strocov, V. N., Schuwalow, S., Rajpalk, M., Ohtani, K., Krogstrup, P., Winkler, G. W., Gukelberger, J., Gresch, D., Aeppli, G., Lutchyn, R. M., & Marom, N. (2022). Electronic Structure of InAs and InSb Surfaces: Density Functional Theory and Angle-Resolved Photoemission Spectroscopy. Advanced Quantum Technologies, 5(3), 2100033. https://doi.org/10.1002/qute.202100033.
5. J.K Modak et al. "Spin Polarization and Electronic structure calculation of Ni and Co_2MnSi thin film interface", Inter. J. Sci. Engi. Res. 6, 8, (2015). https://www.ijser.org/researchpaper/Spin-Polarization-and-Electronic-Structure-calculation-of-Nickel-and-Co2MnSi-thin-film-interface.pdf
6. P. Barman et al. "Lead-free novel perovskite Ba3AsI3: First-principles insights into its electrical, optical, and mechanical properties", Heliyon 9, 11 e21675(2023). https://doi.org/10.1016/j.heliyon.2023.e21675
7. M. Rasheduzzaman et al. "Structural, mechanical, thermal, and optical properties of inverse-Heusler alloys Cr_2CoZ (Z = Al, In): A first-principles investigation", Physics Letters A, 385, 126967 (2021). https://doi.org/10.1016/j.physleta.2020.126967
8. K. M Hossain et al. "Influence of antimony on the structural, electronic, mechanical, and anisotropic properties of cubic barium stannate", Materials Today Communications, 26, 101868(2021).

https://doi.org/10.1016/j.mtcomm.2020.101868

9. Md. Zahid Hasan et al. "Structural, mechanical, electronic, and anisotropic properties of niobium-doped strontium ferrite: first-principal calculations", Applied Physics A, 127, 36(2021). https://link.springer.com/article/10.1007/s00339-020-04219-5

10. Md. Khokon Miah et al. "Comprehensive study on the physical properties of tetragonal La*T*Ge$_3$ (*T* = Rh, Ir, or Pd) compounds: An *ab initio* investigation", AIP Advances, 11, 025046 (2021). https://doi.org/10.1063/5.0042924

11. Md. Zahid Hasan et al. "Insights into the physical properties of inverse-Heusler alloy Cr_2CoGa via density functional theory", Physica Scripta 96, 5 (2021). https://iopscience.iop.org/article/10.1088/1402-4896/abe90e/meta

12. Yang, S., Electronic Structure of InAs and InSb Surfaces: Density Functional Theory and Angle-Resolved Photoemission Spectroscopy. Advanced Quantum Technologies, 5(3), 2100033. https://doi.org/10.1002/qute.202100033

13. C. Xu et al. "Gapped electronic structure of epitaxial stanene on InSb(111)", Physical Review B, 97. 035122 (2018), https://doi.org/10.1103/PhysRevB.97.035122

14. M. Jardine et al. "First-Principles Assessment of CdTe as a Tunnel Barrier at the α-Sn/InSb Interface" ACS. Appl. Mater. Interfaces, 15, 12, (2023), https://doi.org/10.1021/acsami.3c00323

15. Y. M. Koroteev, G. Bihlmayer, E. V. Chulkov, and S. Blügel, "First-principles investigation of structural and electronic properties of ultrathin Bi films", Physical Review B **77**, 045428 (2008). https://doi.org/10.1103/PhysRevB.77.045428

16. See http://www.flapw.de for a program description.

17. H. S. Inbar et al. "| Inversion Symmetry Breaking in Epitaxial Ultrathin Bi (111) Films", arxiv (2023). https://arxiv.org/ftp/arxiv/papers/2302/2302.00803.pdf

Chapter 5

Results & Discussion

5.1 Introduction

5.2 Results

5.3 Discussion

5.4 Conclusion

5.5 Reference

Chapter 5

Results and Discussion

5.1 Introduction

This chapter presents a study on the electronic structure of bismuth thin films grown on indium antimonide substrates. The thickness of the films was found to influence the presence of quantum well states (QWS), with a new state observed in ultrathin films of less than 2 bilayers (BL). The study also confirmed the electronic structure of films with thicknesses from 1 monolayer (ML), providing insights into the conductivity and transition properties of bismuth. The findings suggest that the broken inversion symmetry remains at the $\overline{M/2}$ point, and the observed electron pocket is the signature of broken inversion symmetry. Moreover, the study provides a deeper understanding of metal/semiconductor interactions and their potential applications in advanced electronic devices.

Experimental Results

To address the research questions, I cleaned the substrate and deposited Bi on a pristine InSb substrate, as described in **Chapter 3**. As previously mentioned, the formation of bilayers was monitored through RHEED oscillation. These observations were supported by ARPES and DFT calculations, which utilized quantum espresso as discussed in **Chapter 4**.

RHEED Pattern

In this study, the InSb (111) B face was cleaned through repeated cycles of Ar^+ ion sputtering and annealing in the MBE chamber *in situ* attached to the beamline. A sharp RHEED pattern characteristic of the 3×3 surface reconstruction of InSb was observed after sample preparation [**Fig. 5.1**]. The intense white pattern and dark black background indicate substrate perfection. Bi was then deposited on the InSb (111) B-3×3 substrate using an evaporation technique, and pure Bi was evaporated from the alumina crucible at room temperature. After Bi depositing starts [**Fig. 5.1 (b)**], the RHEED pattern changed from 3×3 to 1×1 means substrate surface cover by Bi atoms [**Fig. 5.1 (c)**]. The high-quality Bi film growth on InSb(111)B-3×3 substrate was

confirmed by real-time RHEED oscillation. During the real-time 4 minutes Bi growth on InSb (111) B-3×3, the surface fractional rods derived from the 3×3 super-lattice of the InSb (111) B substrate changed from 3×3 to 1×1 [**Fig. 5.1(a to c)**]. But, without checking the key concept of RHEED pattern and oscillation, it is difficult to say anything about growth morphology.

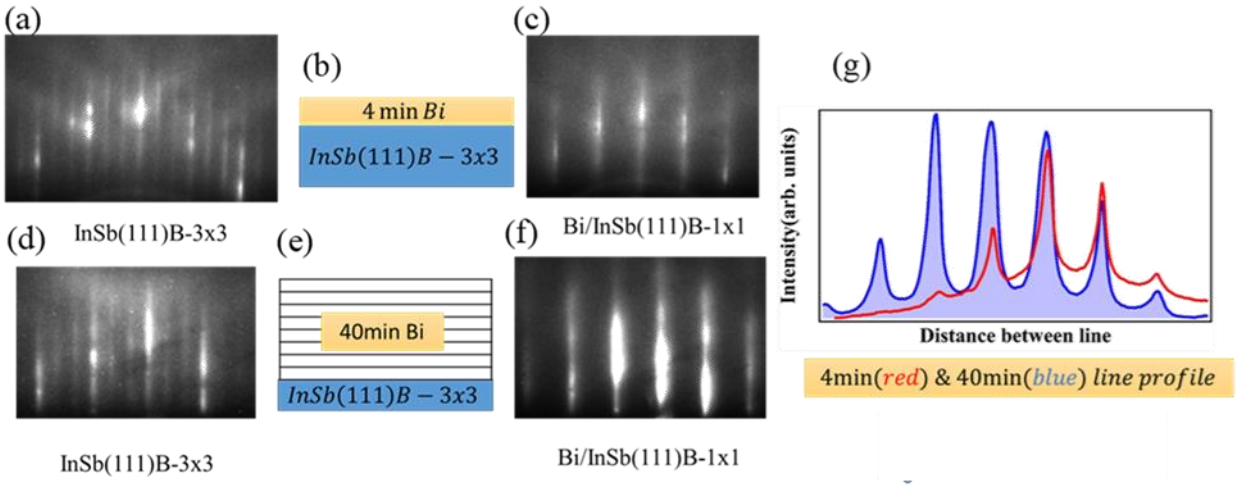

Fig. 5.1. RHEED pattern from clean surface to 40min Bi evaporation, **(a) &(d)** clean surface InSb(111)-3×3, **(b)** and **(e)** layer pattern, **(c)** 4 min Bi evaporation, **(f)** 40 min Bi evaporation, **(g)** Compare RHEED line intensity, 4 min(red), 40 min(blue), slight mismatch observed.

Therefore, this 1×1 reconstruction sustains until 40 min Bi deposition on InSb(111)B substrate; one can see the bright light on each rod, representing 1×1 features (**Fig. 5.1 (f)**). Due to the lattice-matched substrate InSb (lattice parameter: 4.58 Å) and deposited Bi (4.54 Å), it is a little bit difficult to observe a tiny line shift. From this point of view, I checked the line profile of the RHEED pattern integer-order rods between 4 min and 40 min Bi evaporation on InSb(111)B-3×3, and little shift was observed (**Fig. 5.1 (g)**). However, due to the slight difference (~0.5 Å or 0.05 nm), detecting peak shift from the RHEED diffraction rod width is difficult. In this direct evaporation, change the pattern intensity, which differentiates the 4 min and 40 min evaporation. So, for clear information, check the ten sets of real-time evaporation images and fit the line profile (**Fig. 5.2**).

However, as mentioned earlier, the difference in lattice constant between the InSb substrate (4.58 Å) and Bi (4.53 Å) is very small, only 0.8%, which makes it difficult to detect any significant shift in the pattern lines. To overcome this challenge, I calculated the lattice constant by measuring the average distance from each pattern line profile peak, with InSb as the reference for comparison, as shown in **Fig. 5.2.**

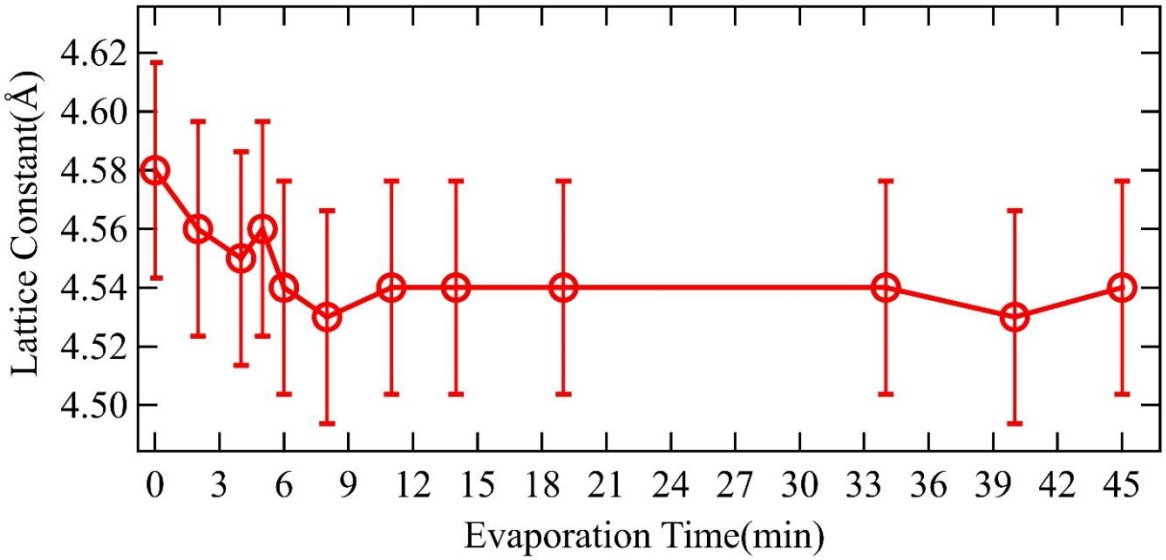

Fig. 5.2. Calculated lattice constant as a function of Bi evaporation time in InSb (111) B-3×3 substrate, where 0 minutes represent the InSb lattice constant and 9 minutes to 45 minutes after Bi deposition starts on clear substrate InSb(111)B-3x3 substrates.

The zero-evaporation time signifies the pristine state of the InSb (111) B-3×3 surface before the deposition of Bi on InSb. Upon Bi deposition, the lattice constant begins to decrease, reaching its lowest points at 8 and 40 minutes. These time intervals correspond to the thickness of 2 BL and the bulk or may be attributed to artifacts. As a result, there is a slight reduction in the lattice constant from 4.58 ±0.05 Å to 4.53 ±0.05 Å, which falls within the 0.8% error margin caused by the lattice mismatch between Bi and InSb. To ensure that this threshold is not exceeded by more than 0.8%, I thoroughly examined the potential impact and found that all data points remained within the range of error, indicating a negligible level of lattice mismatch in the early stages. This change holds significant significance as it contributes to the formation of a robust foundational structure in nature, allowing atoms to acquire sufficient energy for relaxation and the development of higher BL. Additionally, it suggests a prominent 2D symmetry on the surface. However, it is important to note that depending on experimental conditions and diffraction effects, certain RHEED peaks may undergo alterations. Nevertheless, the maximum change should remain within the lattice constant range between the substrate and the deposited material.

RHEED Oscillation

Fig. 5.3 displays RHEED oscillations of (00), but the (02) peak is more informative as it has almost four visible peaks compared to only three visible peaks on (00). The first peak maximum was observed at 3 minutes after the shutter opened, indicating the completion of the first monolayer (ML) growth, and the same as in the (00) lines. It should be noted that the evaporation rate was 1/minÅ and some system loss occurred, making it impossible to complete 1BL within 3 minutes (3.95Å), it must be 1ML (1.975Å).

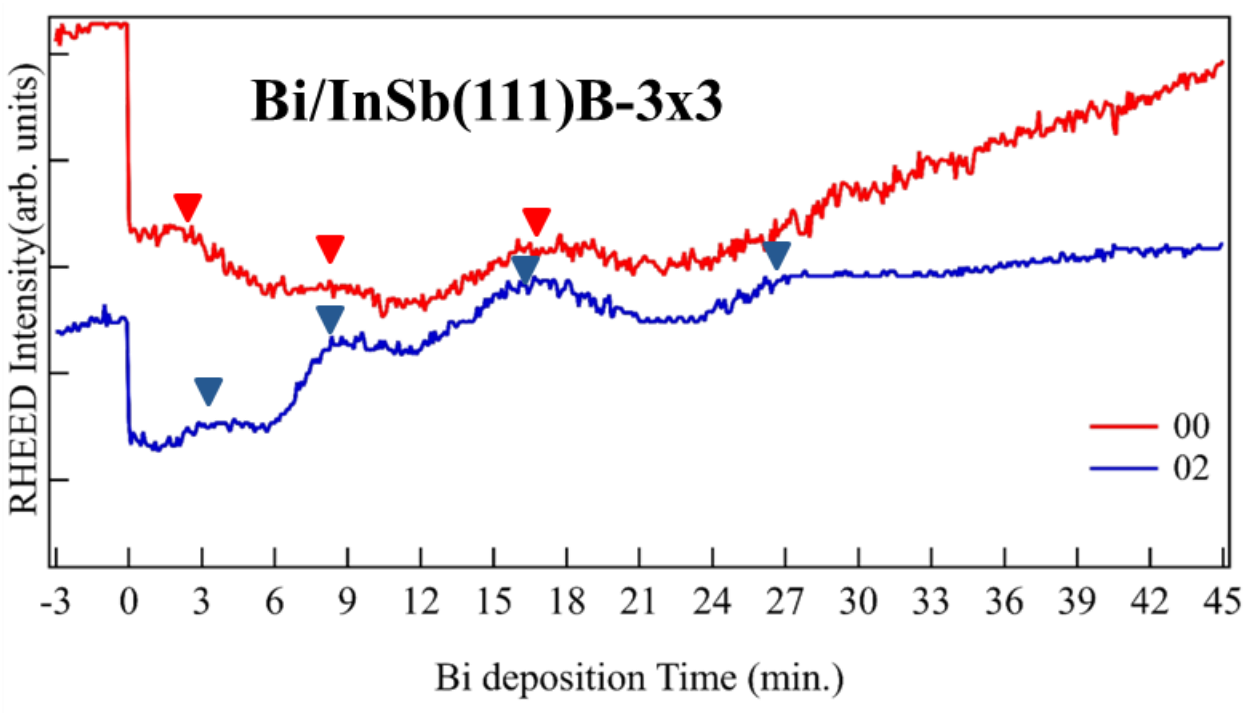

Fig. 5.3. RHEED oscillation as a function of real-time deposition of Bi/InSb(111)B-3×3 at 00 and 02 reciprocal rods.

Following the first peak, the second, third, and fourth are visible at 9, 18, and 27, respectively, 1st, 2nd, and 3rd, which suggested ideal growth phenomena and layer-by-layer (LBL) growth and key concept for bilayer (BL) formation. However, in a recent study, STM images were used to demonstrate the ST types of growth in this system suggesting monolayer formation [**12**].

ARPES Measurement

Band Dispersion along Γ*M* Direction

To obtain results that provide an understanding of the concept of thickness in the formation of the QWS formation start from more than 1BL thickness shown in **Fig. 5.4(b),** and thickness

dependency features observed in other BL **(Fig. 5.4(c-f)**, but down to 1BL no possible signature as shown in **Fig.5.4(a).** Therefore, I consider the energy distribution curve (EDC) and determined the peak position in the range 0.75Å to 0.85Å wavevector surrounded by $\bar{\mathbf{M}}$ point with intervals of 0.1Å. These results showed a slight shift in energy position compared to the previous report **[1]**. In such cases, I implement the QWS concept and calculate the thickness by PAM.

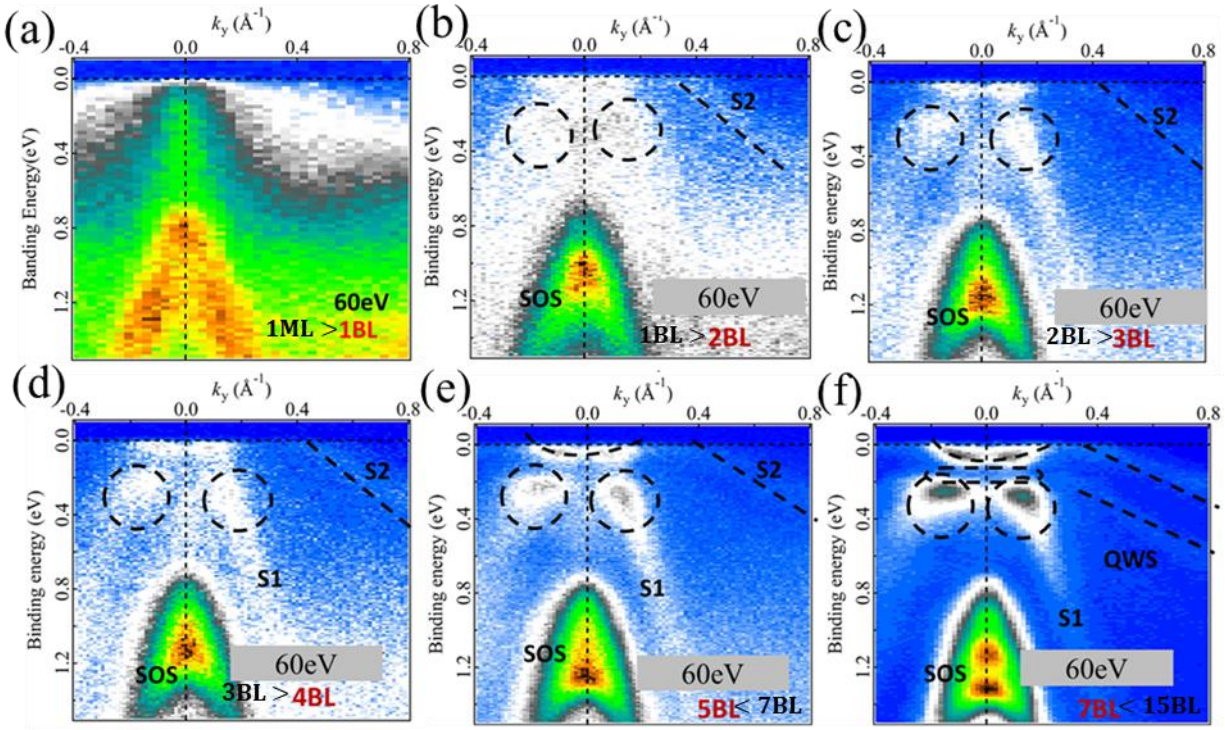

Fig. 5.4. The band dispersion along the $\overline{\Gamma M}$ direction of the Fermi surface, (a) 1ML<1BL, (b) 1BL<2BL, (c)2BL < 3BL, (d) 3BL<4BL, (e) 5BL>7BL, (f) 7BL>15BL, where light energy is linear horizontal 60eV, and temperature is 7.2K.

Phase Accumulation Model:

The phase accumulation model tracks the phase shift of the wavefunction during its back-and-forth travel within the well. The model matches the total phase shift to an integer multiple of **2π** to determine the allowed quantized energies of the quantum well states.

Based on this model, it is possible to easily understand the bilayer concept in the context of my experimental findings [**1**]. This is shown in **Fig. 5.5**, where the fitted results by PAM and QWS are presented. By comparison with Inbar et al. [**1**] results in **Fig. 5.5(b)**, my initial bilayer concept by QWS is a little bit contradicts and suggested monolayer formation after 4min Bi on InSb as shown in **Fig. 5.5(c)**, and which rejected other possible peculiar growth by RHEED

oscillation and suggested LBL with 9min interval of each BL in **Fig. 5.3**. The lowest QWS observed at 1.25BL and have a high resolution down to 1BL that is after 5min Bi on InSb, which reflected point like FS and band shift dispersion rejected semiconductor possibility and touch Fermi energy rejected semi-metal to semiconductor transition, but it's suggested semi-metal to metal transition after 5min Bi on InSb case.

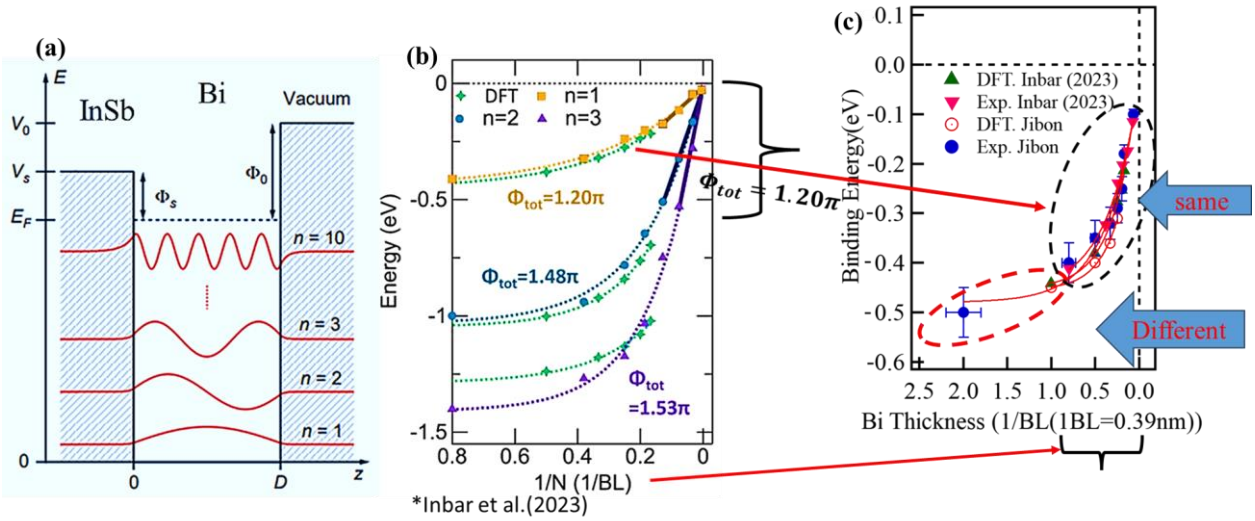

Fig. 5.5. The comparative ARPES data between Inbar et al. [**1**] and my experimental results, (**a**) the PAM model helps to understand thickness-dependent QWS formation. (**b**) Corresponding previous results by Inbar et al. [**1**], (**c**) where the exact band's position is observed by EDC, and due to thickness dependency phenomena, thickness almost reflected the same behavior, only distinct signature remains down to 1BL Bi films.

To obtain a deeper understanding of the observed phenomena, I conducted a comprehensive analysis by comparing the ARPES band dispersion and corresponding distribution curves. I begin the comparison by examining the pristine InSb(111)B surface shown in **Fig. 5.6(d)**, where a distinct band gap of approximately 0.17eV is evident. However, after the Bi evaporation process for 5 minutes, as shown in the RHEED pattern (**Fig. 5.6(a and b)**), significant changes can be observed. The RHEED oscillation displays a prominent peak after 3 minutes, as illustrated in **Fig. 5.6(c)**, and subsequently, the band gap completely disappears from the clean substrate band dispersion, as demonstrated in **Fig. 5.6(e)**.

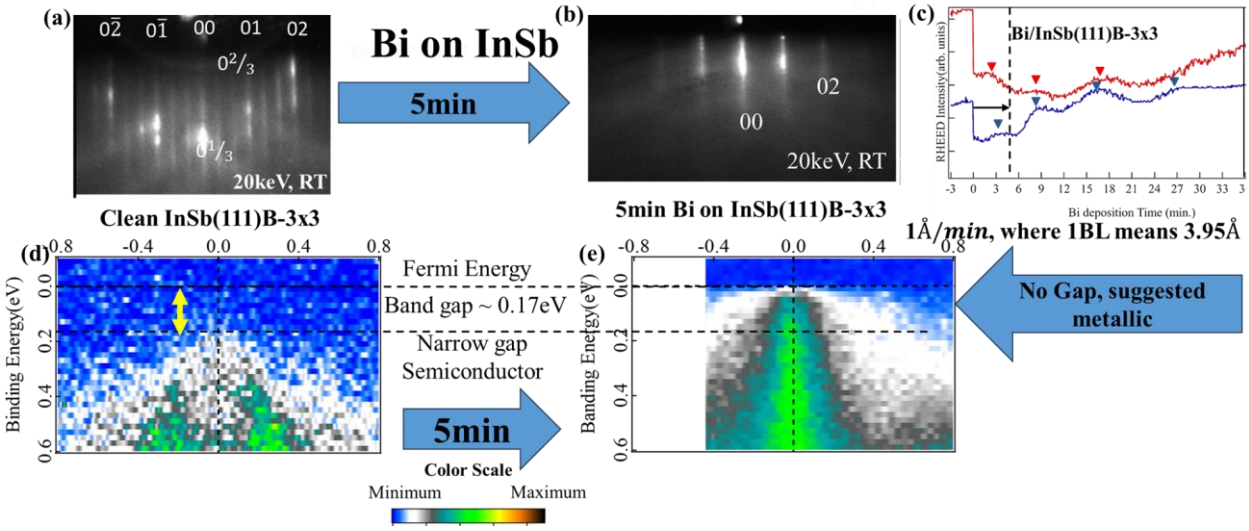

Fig. 5.6. (a) Clean surface InSb(111)B-3x3, (b) After 5min or 1ML Bi(111) on InSb(111)B, (c) RHEED Oscillation, (d) Band dispersion of InSb(111)B-3x3 along $\overline{\Gamma M}$ direction, (e) Band dispersion after 5min or 1ML Bi on InSb(111)B-3x3 along $\overline{\Gamma M}$ direction.

Fermi Surface along $\overline{\Gamma M}$ direction

Fig. 5.7 shows the constant energy Fermi contour that moves through Fermi energy to binding energy for two different thicknesses: 1ML and 1.25BL after PAM application in **Fig. 5.5**. The Fermi energy value of Eb = 0eV indicates that the 1ML case is different from the 1.25BL case.

A point-like feature emerges right next to the Fermi energy at 0eV, indicating the possibility of a crossing between the conduction band minimum (CBM) and valence band maximum (VBM). As a result, high-contrast point-like features are likely to be discovered. Based on the recommended 200meV energy window, some states are visible in the direction of $\overline{\Gamma M}$ for the 1ML case and are visible in the 1.25BL case. A more precise description of this phenomenon can be obtained by comparing band dispersion and DFT calculations.

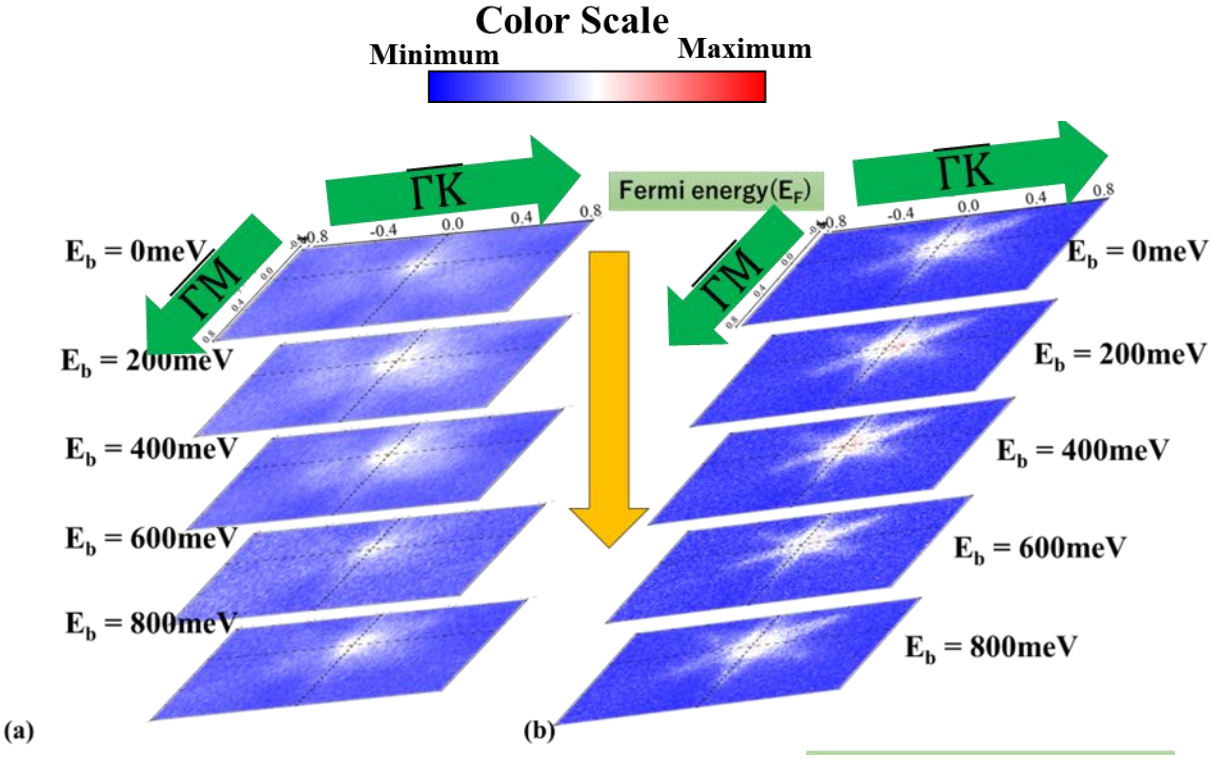

Fig. 5.7. The constant Fermi-energy contour of (a) 1ML, (b) 1.25BL Bi (111) on InSb(111)B.

Comparative study between ARPES band dispersion and DFT band calculations.

The 1.25BL Fermi contour (**Fig. 5.8(a)**) clearly suggested the bulk-like shape at 0meV, which is very close to the Fermi energy view. The band dispersion reflects the new states remain in a slightly different energy position compared to the 1.25BL results shown in **Fig. 5.8(a)**, which proves observed FS is 1ML **(Fig. 5.9)** because the thickness dependency phenomena suggested that, if thickness increases, the QWS changes the energy position proved by Hirahara et al. (2006) [**5**] and Inbar et al. [**1**]. Therefore, this is a good calibration tool for calculating the ultrathin thickness, and I found the same QWS as the suggested QWS.

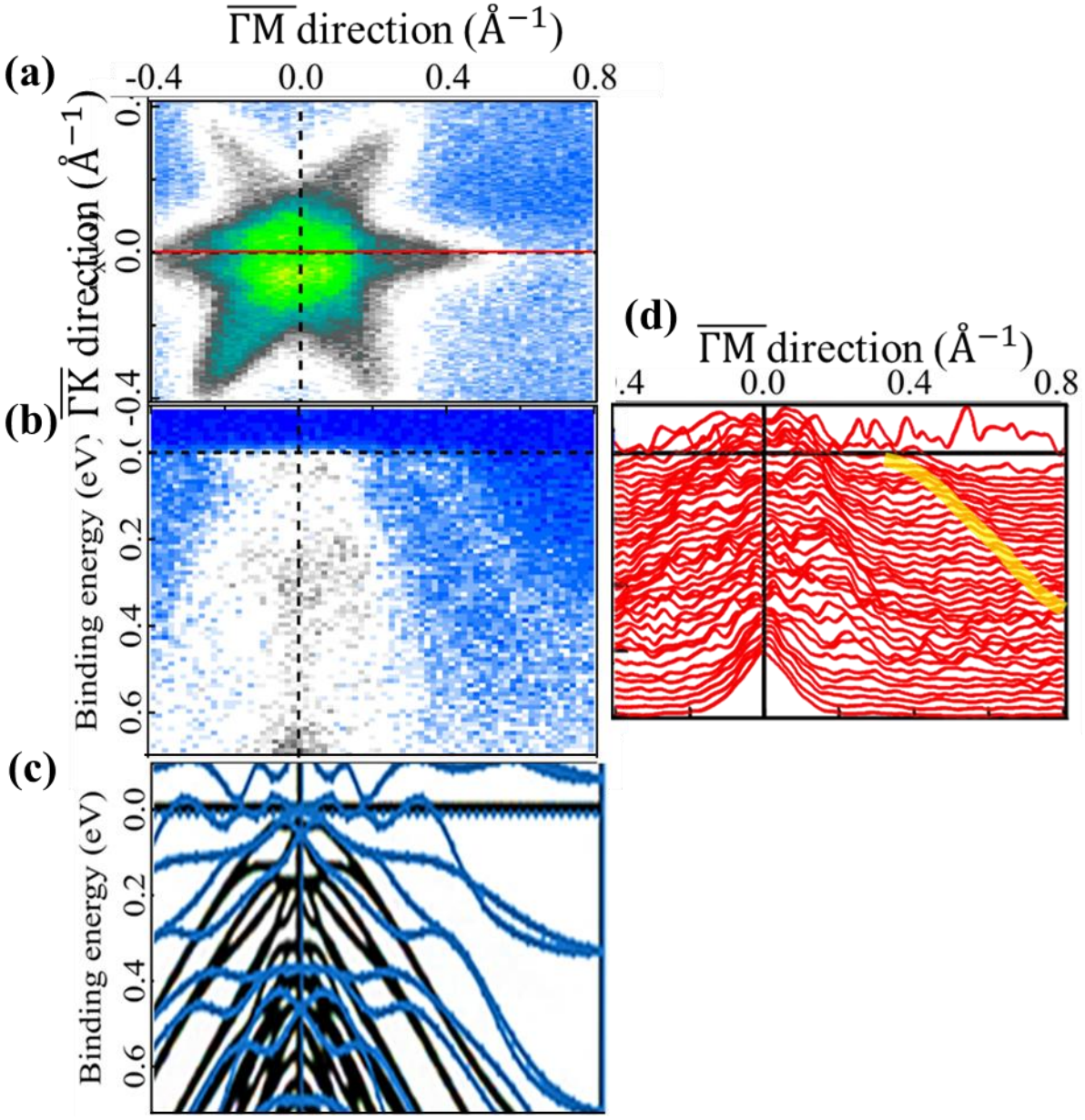

Fig. 5.8. The 2BL formation, (a) Fermi surface, (b) ARPES image, (c) Momentum distribution cure, (d) corresponding band structure calculation, where the blue line is the Bi/InSb interface and black comes from slab InSb.

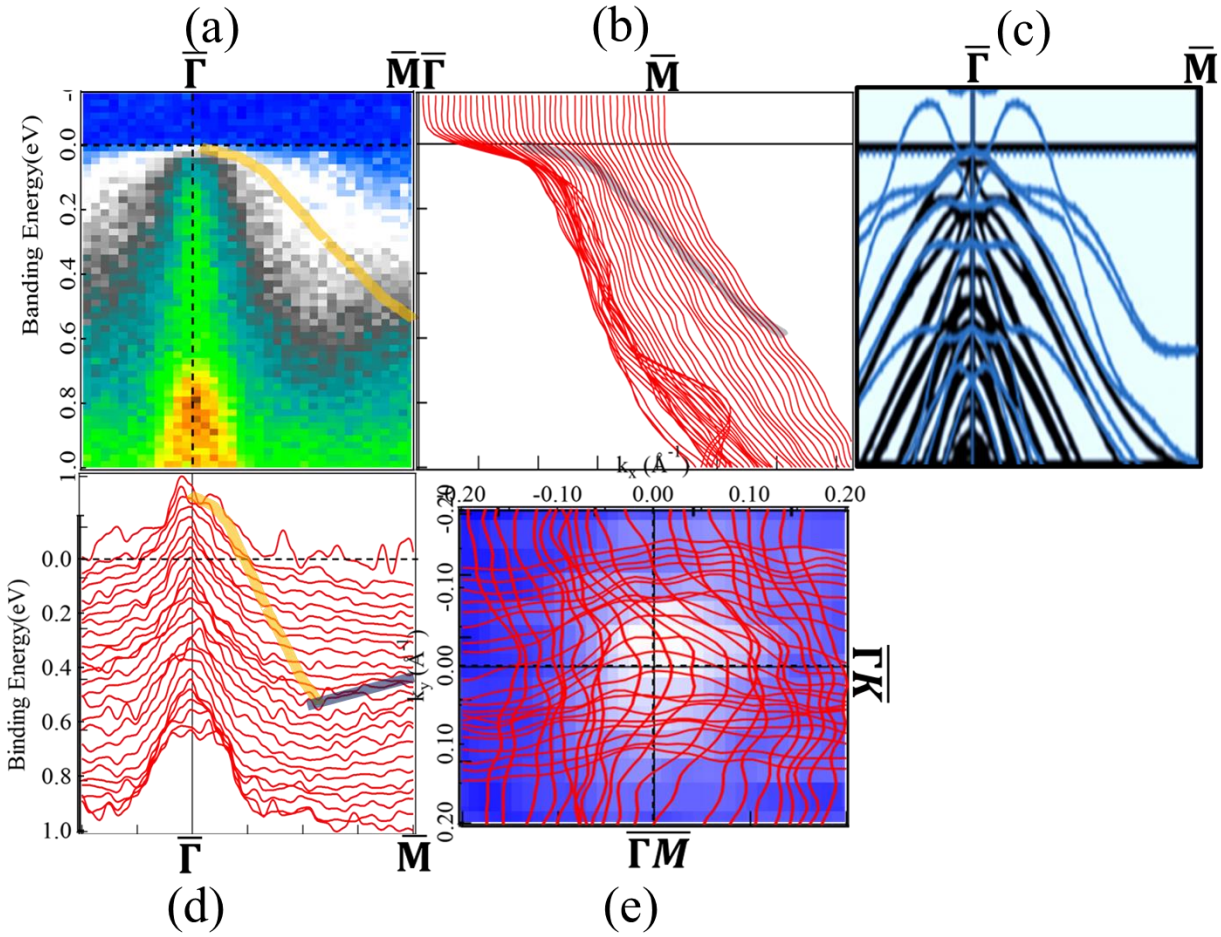

Fig. 5.9. The down to 1ML formation (a) ARPES image, (b) Energy distribution curves (possible peak shows by blue shadows), (c) Calculate band structure, where the blue line is the Bi/InSb interface and black comes from slab InSb. (d) momentum distribution curves (possible peak, to down going line in yellow, and up going line in blue), (e) corresponding intensity map on constant Fermi energy contour overlap by an intensity map shows circular like structure.

Upon closer examination down to the 1.25BL case in **Fig. 5.8(b, d)**, it is apparent that the state is more closely resembling a QWS, and no signature of symmetry breaking remains in the 1ML case in **Fig. 5.9**. However, the CBM approaches the Fermi energy, which may explain the observed bulk-like FS in the 1.25BL case. Additionally, my ARPES measurements may give an $\pm$0.01eV value near the Fermi energy (E_F) in the FS case, but the exact position of the Fermi energy is uncertain. To determine the precise Fermi energy position, I used a gold plate touch method. The possible reason for these types of points like the Fermi surface discussed below.

1. Charge transfer

Charge transfer occurs when electrons are transferred from one atom to another. In the case of Bi/InSb, possible charge transfer may occur from the Bi atoms to the InSb surface. This charge transfer could lead to the formation of a surface dipole layer, which could also affect the electronic properties of the system. As observed in the CLPES, the Sb4d peak shifted to a higher binding energy after Bi deposition, reflecting the possible charge transfer effect. This shift suggests the presence of new bands as well as substrate influence on the system's electronic properties.

2. Interface states

Interface states are electronic states that are localized at the interface between two materials. In the case of Bi/InSb, possible interface states could be created by the interaction between the Bi atoms and the InSb surface. These interface states could have a significant impact on the electronic properties of the system, such as affecting the density of states, the formation of new electronic states, and the charge transfer between the Bi atoms and the InSb surface, as observed in the CLPES with the sb4d peak shifting to a higher binding energy after Bi deposition.

In **Fig. 5.10,** I summarize experimental findings, which include the 1ML Fermi surface (a) and band dispersion (d). These results reject the previous prediction of SMSC and suggest a possible semi-metal-to-metal transition as the thickness decreases from thick to ultrathin (c). My experimental observations using ARPES, and theoretical calculations challenge the expectation of surface state modification by the substrate, revealing a remarkable transition from a semimetal to a unique metallic state with a persistent Fermi surface with at least 1 monolayer. The discovery of a surprising semimetal-to-metallic transition in ultrathin bismuth (Bi) films unlocks exciting possibilities for novel applications in diverse fields. Here are some potential applications inspired by the unique properties of this metallic state:

1. Transparent Conductors:

a. Ultra-thin, high-transparency electrodes: The metallic state down to 1 monolayer offers the potential for exceptionally thin and highly conductive transparent electrodes, which could revolutionize applications such as organic light emitted diodes (OLED) displays, touchscreens, and solar cells by improving light transmission and device efficiency.

b. Flexible and conformable electronics: The ultrathin nature of the Bi films, which exhibit metallic properties down to 1 monolayer, makes them ideal for integration into flexible substrates, enabling the development of bendable and stretchable displays, sensors, and other electronic devices. This offers great potential for the creation of flexible and conformable electronics that can improve device efficiency and performance.

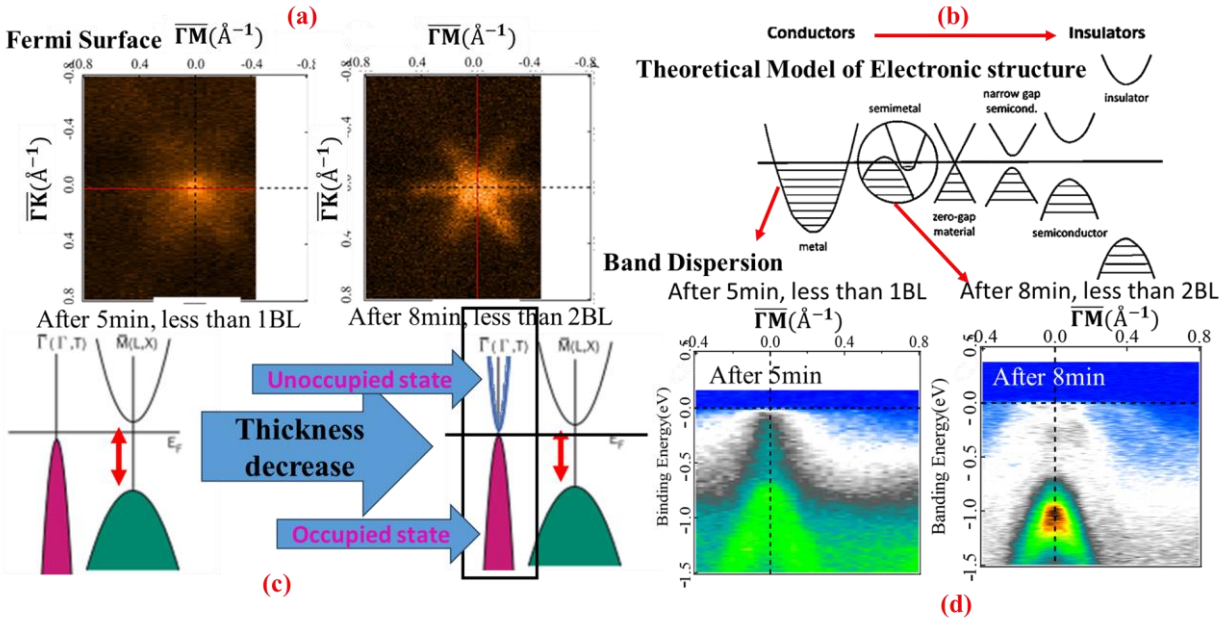

Fig. 5.10. The final summary of the total experiment and theoretical work, (**a**) Experimental Fermi surface, (**b**) Schematic drawing to understand the electronic structure of conductor to insulator journey, (**c**) Schematic model for semimetal to semiconductor transition, (**d**) Experimental band dispersion.

2. Plasmonics:

The unique properties of the metallic state, such as the circular Fermi surface and robust band dispersion, could be exploited to design plasmonic devices with enhanced light localization, propagation, and control. These properties offer potential advancements in areas such as optical metamaterials, nano-scale light sources, and ultra-sensitive biosensors.

3. Spintronics:

The spin-orbit coupling inherent in Bi could be utilized in combination with the metallic state to achieve spin-polarized transport in ultrathin films. This could lead to the development of new spintronic devices such as spin valves, spin filters, and logic gates with enhanced efficiency and functionality.

4. Quantum Materials:

Theoretical predictions suggest that specific thicknesses and surface interactions of ultrathin Bi films could lead to the realization of topological phases and Majorana fermions. This offers opportunities for studying exotic quantum phenomena and exploring potential applications in topological quantum computing.

5. Beyond Bi:

Understanding the mechanisms behind the unexpected metallic state in Bi could provide valuable insights into similar transitions in other materials. This knowledge could be applied to engineer novel electronic and topological properties in other thin-film systems, leading to a plethora of new device possibilities. Therefore, the exploration of ultrathin films beyond Bi is a promising avenue for future research and development.

5.4 Conclusion

This dissertation presents a comprehensive study on the electronic structure of thin films of heavy semi-metal Bismuth (Bi), focusing on the transition from monolayer (ML) to bilayer (BL) and the influence of spin-orbit coupling (SOC). Additionally, the growth of these thin films on indium antimonide (InSb) substrates with a lattice match of 0.08% is examined, as noted in [1].

Through experimental and theoretical investigations, I demonstrate that the substrate has a significant impact on the electronic structure of the Bi thin films. Specifically, they observed thickness-dependent quantum well states (QWS) caused by the phase accumulation model (PAM) [1]. Moreover, my findings confirm the existence of a new state in ultrathin films with less than 2BL, in line with theoretical predictions based on the band structure [4]. The thickness of the Bi films is accurately determined through energy and momentum distribution curve analysis using the PAM.

In thicker Bi films, I was able to replicate previous findings [1, 5], including the existence of QWS, surface states, and electron and hole pockets. However, I did not find any conclusive evidence for films as thin as 1BL. Nonetheless, I was able to detect clear indications of a 1ML (0.5BL) thickness and perform a comprehensive analysis of its electronic structure.

Furthermore, I discovered QWS at a thickness of 1.25BL and conducted a thorough analysis using the PAM.

By investigating the electronic properties of Bi (111) on InSb, I shed light on the higher conductivity observed in comparison to free-standing Bi (111). My research also resolves the long-standing debate regarding the transition from semi-metal to semiconductor in the bulk case [**6, 7**], as well as the transition from semi-metal to metal in ultrathin films. I reveal that higher conductivity, combined with SOC, plays a crucial role in the quantum spin hall effect, where SOC acts as an external magnetic field. These findings hold significant implications for the development of next-generation quantum computers.

Overall, the results of this study provide a deeper understanding of the electronic behavior arising from metal/semiconductor interactions and offer a solid foundation for future research endeavors aimed at exploring the behavior of thin films and their potential applications in advanced electronic devices.

5.5 Reference

1. H. S. Inbar et al. "| Inversion Symmetry Breaking in Epitaxial Ultrathin Bi (111) Films", arxiv (2023). https://arxiv.org/ftp/arxiv/papers/2302/2302.00803.pdf
2. T. Hirahara, G.Bihlmayer, Y.Sakamoto, M.Yamada, H.Miyazaki, S.Kimura, S.Blugel, and S.Hasegawa, "Interfacing 2D and 3D Topological Insulators: Bi (111) Bilayer on Bi_2Te_3", Physical Review Letters **107**, 166801(2011). http://www-surface.phys.s.u-tokyo.ac.jp/papers/2011/Hirahara-PRL2011Oct.pdf
3. Z. Liu, C. X. Liu, Y. S. Wu, F. Liu, J. Wu, "Stable nontrivial Z_2 topology in ultrathin Bi (111) films: a first-principles study", Physical Review Letters **107**, 136805 (2011). https://doi.org/10.1103/PhysRevLett.107.136805
4. Y. M. Koroteev, G. Bihlmayer, E. V. Chulkov, and S. Blügel, "First-principles investigation of structural and electronic properties of ultrathin Bi films", Physical Review B **77**, 045428 (2008). https://doi.org/10.1103/PhysRevB.77.045428
5. T. Hirahara, T. Nagao, I.Matsuda, G.Bihlmayer, E.V.Chulkov, Yu.M.Koroteev, P.M. Echenique. M.Saito, and S.Hasegawa, "Role of Spin-orbit coupling and Hybridization effects in the electronic structure of ultrathin Bi films", Physical Review Letters **97**, 146803(2006). https://doi.org/10.1103/PhysRevLett.97.146803

6. Yakovkin “Dependence of the band structure of Bi (111) bilayers on lattice constant and spin-orbit splitting induced by a H monolayer. Journal of Physics and Chemistry of Solids”, 129, 277-283(2019). https://doi.org/10.1016/j.jpcs.2019.01.027
7. Taniguchi, M., Fujimori, M., Fujisawa, M., Mori, T., Souma, I., & Oka, Y. (1987). “Mn 3d partial density-of-states and p-d hybridization in Cd1-xMnxY (Y = S, Se and Te)”. Solid State Commu., 62(6), 431-434. https://doi.org/10.1016/0038-1098(87)91049-0
8. Speranza, G., Calliari, L., Laidani, N., & Anderle, M. (2000), “Semi-quantitative description of C hybridization via s- and p-partial density of states probing: An electron spectroscopy study”, Diamond and Related Materials, 9(11), 1856-1861. https://doi.org/10.1016/S0925-9635(00)00338-1

Chapter 6

6.1 Summary &Conclusion
6.2 Papers in Preparation
6.3 Future Road Map

Chapter 6

6.1 Summary and Conclusion

This dissertation investigates the growth phenomena and photoemission effects on thin-film topological materials, specifically on the InSb (111) B, as well as ultrathin Bi (111) films. The analysis primarily focuses on thickness-dependent effects and phenomena, based on quantum well states, which arise due to the inherent quantum size effect in thin films.

The focus of this study is on the use of ARPES, which is a powerful technique for analyzing localized low-dimensional states confined within the film plane. The existence of the film's surface results in the appearance of new bands, such as Quantum Well States (QWS), which are confinement-induced states that play a significant role in the electronic behavior of thin film thickness, in such cases I implement a phase accumulation model (PAM).

To investigate the structural and electronic changes, I will employ density functional theory (DFT) simulations in the Quantum Espresso software package, which accurately models material properties and electronic structure. As previous studies have shown, the spin-orbit coupling (SOC) approximation is essential in accurately describing the electronic properties of the Bi/InSb interface, and I will also utilize this approach.

Before delving into the details of the structural and electronic changes, it is essential to understand the basics of Quantum Espresso, Linux, and Python as these are essential tools for reproducing the work and conducting further studies. Having a solid foundation, I will proceed to introduce the Bi (111) surface on the InSb(111) slab, which has been experimentally investigated. I will compare the experimental results with the predictions from my DFT calculations to gain insights into the accuracy and reliability of my computational methods.

Through analysis of the structural and electronic changes in InSb and the impact of SOC on these modifications, I aim to enhance my understanding of the materials science underlying this intriguing semiconductor compound. This understanding not only advances the fundamental comprehension of Bi/InSb but also holds significant implications for the development and refinement of devices based on this computational material science research.

In addition, my study reveals a new state and a new Fermi surface in the case of 2 atomic layer (1BL) thickness of bi films. This state is distinct from the bulk Fermi surface and is a result of the reduced dimensionality of the thin film, leading to significant changes in its electronic properties. These findings provide valuable insights into the growth and electronic properties of InSb (111) thin films, which can lead to the development of new electronic devices and contribute to the broader understanding of surface science and semiconductor physics.

6.2 Papers in preparation

1. **J. K Modak**, S. Kimura, "*Visualized QWS down to 2BL Bi (111) on InSb(111)B surface by theoretical and experimental evidence*".
2. **J. K Modak**, S. Kimura, "*Experimental and theoretically proven lattice match system rejected free-standing monocrystal growth in topological materials*".
3. **J. K Modak**, S. Kimura, "*Exploring the relationship between surface state and electron pocket in thin bismuth films grown on InSb: An investigation of the influence of substrate morphology on the thickness-dependent electronic properties*".

6.3 Future Road Map

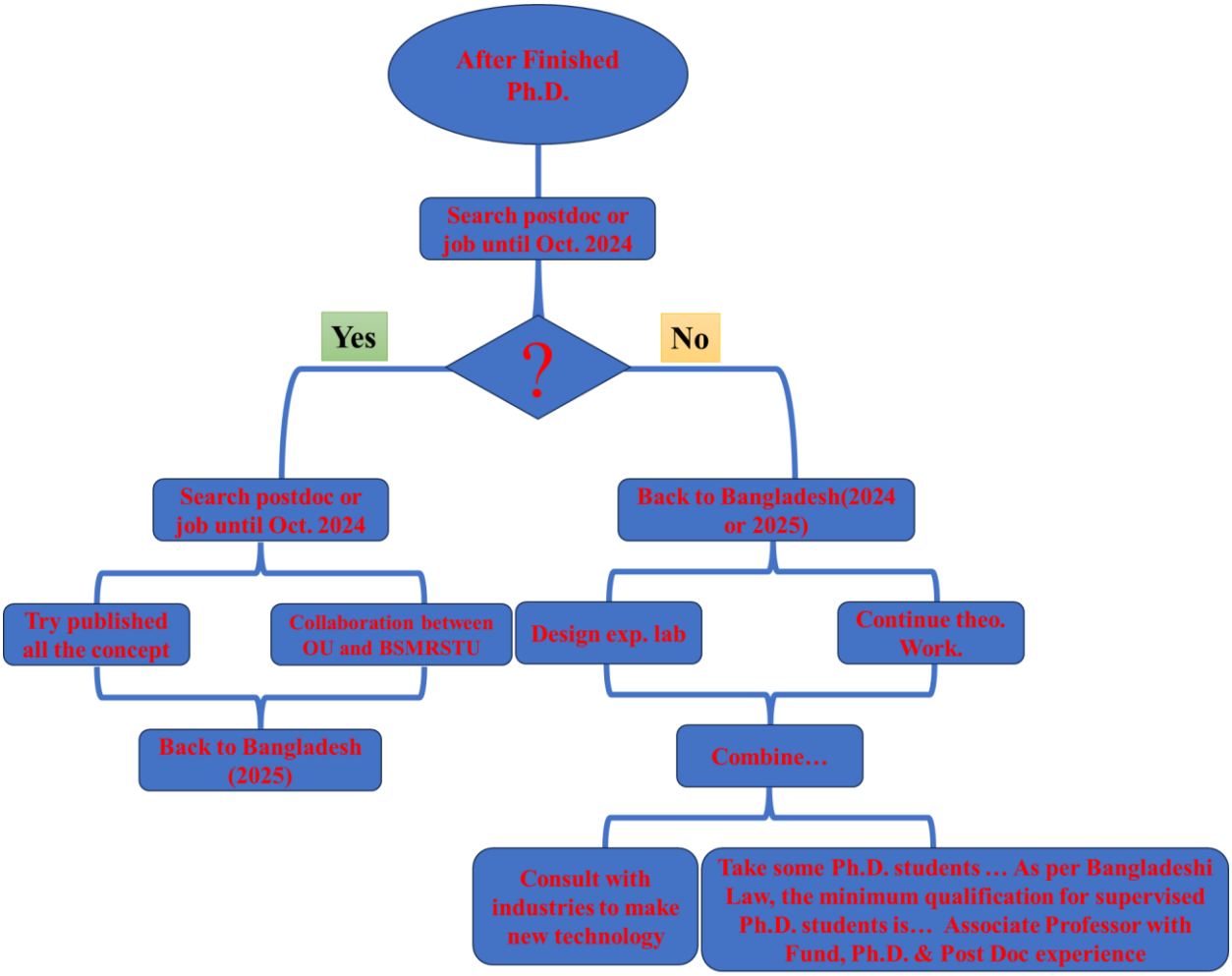

→→ Before coming to Japan, I designed a cluster computer-based theoretical lab at my university. Currently, my three groups are collaborating with twelve universities in Bangladesh. After returning to my country, I plan to acquire funding for developing an experimental lab in Bangladesh. I aim to establish a correlation between theoretical and experimental experiences. Additionally, I intend to establish a collaboration between Osaka University and Bangladeshi Universities. The main objective of the Bangabandhu Fellowship is not only to conduct research but also to increase collaboration and connect with world-class universities. I have already discussed this opportunity with the Osaka University President, Prof. Dr. S. Nishio, and my university Vice-Chancellor, Prof. Dr. A. Q. M. Mahbub. My aim is to collaborate as soon as possible, enabling Osaka University students and Bangladeshi students to exchange knowledge. This cross-cultural collaboration can inspire new ideas, broaden research horizons, and promote a global perspective in academic pursuits. It also presents an opportunity for students to gain

international exposure and develop valuable skills through international exchanges. I have already taken some initiative toward my future research work, and I plan to implement the below list after returning to Bangladesh.

List of Upcoming Projects

1. Jahan, I., **Modak, J. K.**, Hasan, W., Rahman, Jamila, N. A., Hossain, M., Choudhury, M.,Chowdhury, S., Rahaman, R., and Hasan, **Z. have nearly completed their theoretical investigation on the physical properties of cubic perovskite oxides SrXO3 (X = Sc, Ge, Si).**

2. **Modak, J. K**., Barman, P., Rahman, M. F., Islam, M. R., Hasan, M., Chowdhury, M., Hossain, M. K., Ezzine, S., & Amami, M, "***Unveiling the Potential of Ba3XI3(X= Sb, As): A Lead-Free Perovskite with Promising Optoelectronic and Mechanical Properties***" (~70% work finished).

3. **J. K. Modak**, M. Z. Hasan, M. A. Rayhan, M. A. Rahman, M. Rasheduzzaman, and K. M. Hossain, "***Decoding the Multifaceted Nature of Cr2CoGa: A DFT Journey through Structure, Mechanics, and Electronic Wonders***" (~50% work finished).

4. **J. K. Modak**, Md. K. Miah, K. M. Hossain, Md. A. Rahman, Md. Rasheduzzaman, S. K. Mitro, Md. Z. Hasan, "***Bridging the Gap Between Composition and Property Space: A Comprehensive Ab Initio Unveiling of the Physical Landscape in Tetragonal LaXGe3 (X= Rh, Ir, or Pd) Compounds***". (40% of work finished).